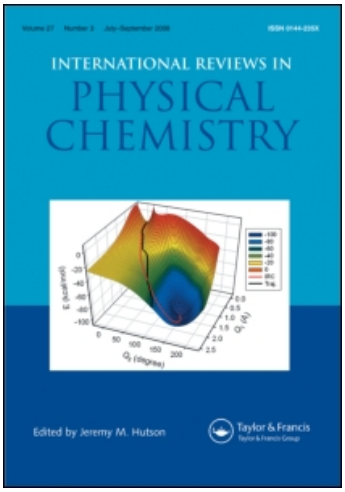

International Reviews in Physical Chemistry
Publication details, including instructions for authors and subscription information:
http://www.informaworld.com/smpp/title~content=t713724383

Applications of molecular Rydberg states in chemical dynamics and spectroscopy

T. P. Softley[a]
[a] Department of Chemistry, Chemistry Research Laboratory, University of Oxford, Oxford OX1 3TA, UK

To cite this Article Softley, T. P.(2004) 'Applications of molecular Rydberg states in chemical dynamics and spectroscopy', International Reviews in Physical Chemistry, 23: 1, 1 — 78
To link to this Article: DOI: 10.1080/01442350310001652940
URL: http://dx.doi.org/10.1080/01442350310001652940

INT. REVIEWS IN PHYSICAL CHEMISTRY, 2004
VOL. 23, NO. 1, 1–78

Taylor & Francis
Taylor & Francis Group

Applications of molecular Rydberg states in chemical dynamics and spectroscopy

T. P. SOFTLEY

Department of Chemistry, Chemistry Research Laboratory, University of Oxford, Mansfield Rd, Oxford OX1 3TA, UK

Molecules in high Rydberg states, in which one electron has been excited into a hydrogenic orbital of large mean radius, have many unusual properties compared to ground state molecules. These properties, which are reviewed in this article, make them suitable for a diverse and growing number of applications in chemical dynamics. The most recent methods for studying molecular Rydberg states using high-resolution spectroscopy and theory, including effects of electric fields, are described here. An important feature is the high susceptibility of Rydberg states to external field perturbation which not only has a profound effect on the observable energy levels, spectroscopic intensities and lifetimes, but is also useful for state-selective detection through field ionization. The large dipole moment that can be created in a field is also useful for controlling the motion of molecules in Rydberg states. The applications reviewed here include: ZEKE (zero kinetic energy), MATI (mass-analyzed threshold ionization) and PIRI (photo-induced Rydberg ionization) spectroscopy; pulsed-field recombination of ions and electrons; the state selection and reaction of molecular ions; collisions of Rydberg states with neutrals, ions and metallic surfaces; Rydberg tagging and imaging of products of photodissociation; and the control of translational motion and orientation via the use of inhomogeneous fields.

Contents

International Reviews in Physical Chemistry ISSN 0144–235X print/ISSN 1366–591X online © 2004 Taylor & Francis Ltd
http://www.tandf.co.uk/journals
DOI: 10.1080/01442350310001652940

1. Introduction: the exotic properties of molecular Rydberg states

This article reviews recent experiments that take advantage of the novel properties of high-principal-quantum-number Rydberg states of molecules. These properties include the almost macroscopic dimensions of the orbital radius, the high susceptibility of the Rydberg electron to external fields, the long timescale associated with the electronic motion, and the very high degeneracy of the quantum states. Figure 1 summarizes the scope of this review, in which it will be seen that the study and understanding of the properties of Rydberg states leads to applications

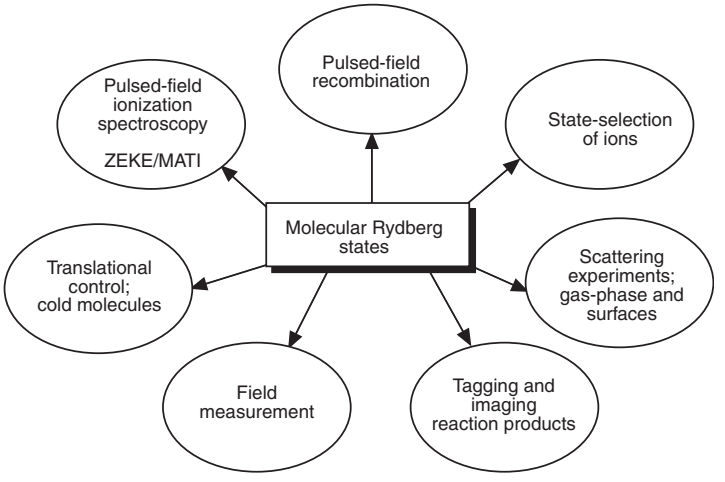

Figure 1. Applications of molecular Rydberg states.

ranging from high-resolution photoelectron spectroscopy, e.g., ZEKE (zero kinetic energy) spectroscopy, to state-selective reactive scattering of ions and Rydberg molecules, to probing of surfaces, to analysis of energy and angular distributions from photodissociation events, to manipulation of molecular motion. In sections 1–4 we review the properties of molecular Rydberg states and how they are studied spectroscopically and theoretically, and then present a review of the applications in sections 5–9.

1.1. *Molecular Rydberg quantum numbers and series*

In a high-n molecular Rydberg state, where n is larger than about 10, one electron has been excited into an orbital of sufficiently large mean radius that the electron can, to a first approximation, be considered to be moving independently of the ionic core of the molecule (see figure 2(*a*)). The electron primarily sees just the net single positive charge of the ionic core and therefore experiences the same potential as if it were in a hydrogen atom. Hydrogenic quantum numbers n, l and m_l are used to characterize the Rydberg electron motion. The ionic core is considered to vibrate and rotate independently of the Rydberg electron motion and therefore is characterized by vibration–rotation quantum numbers v^+, $N^+, \ldots$, which are equivalent to those of the bare cation.

As a consequence of the virtual separability of the motion of the Rydberg electron and the core, the energy can to a first approximation be described as the sum of two terms,

$$E(v^+, N^+, \ldots, n, l, m_l) = I(v^+, N^+, \ldots) + \frac{R}{(n - \delta_l)^2}$$
$$I(v^+, N^+, \ldots) = I_0 + E(v^+, N^+, \ldots) \quad (1)$$

where I_0 is the adiabatic ionization energy, and $E(v^+, N^+, \ldots)$ represents the ionic vibration–rotation energy; thus $I(v^+, N^+, \ldots)$ is the energy required to ionize the

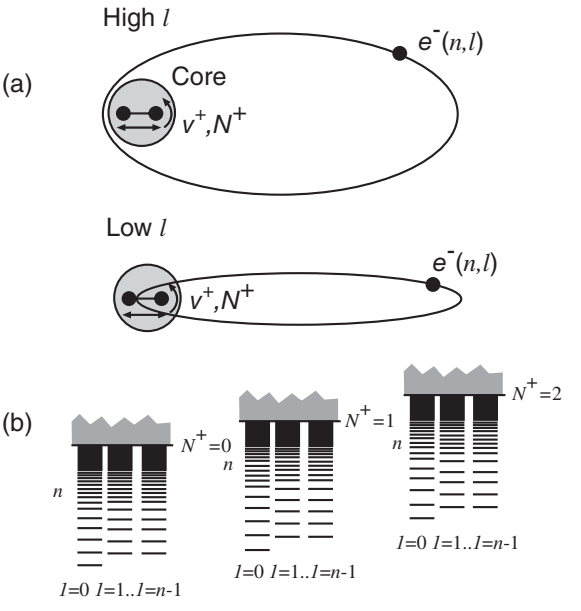

Figure 2. (*a*) Pictorial view of separation of nuclear and electronic motion in a molecular Rydberg state. (*b*) Energy levels (schematic) for a molecular Rydberg state. v^+ and N^+ are the vibrational and rotational quantum numbers for the ionic core.

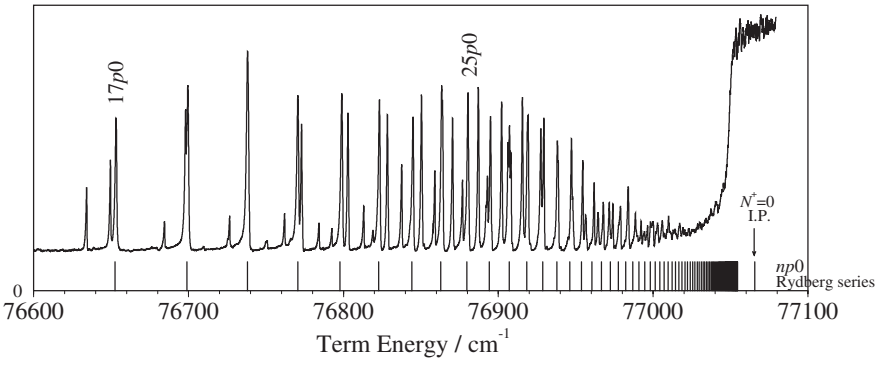

Figure 3. Rydberg series of nitric oxide observed in excitation from the $v = 1, J = \frac{1}{2}$ level of the $A^2\Sigma^+$ electronic state. The main series observed are $np(0)$, $np(2)$ and $nf(2)$, where the notation represents $nl(N^+)$. The positions of the $np(0)$ lines are shown (from ref. [1]).

neutral molecule from its lowest vibration–rotation state to produce a specific vibration–rotation state of the cation. The second term in equation (1) is the familiar Rydberg formula which includes the quantum defect δ_l, the measure of penetration of the Rydberg electron into the region of the electron distribution of the ionic core. Strictly speaking δ_l represents a phase shift of the radial component of the Rydberg electron wavefunction relative to its hydrogenic form. The phase shift arises from the core penetration and is typically larger for lower-l values because of the greater penetration. In a zero-order model, δ_l is independent of n and of the core quantum numbers. The two terms in equation (1) combine together to form the schematic

energy level pattern shown in figure 2(*b*). Figure 3 shows an example of Rydberg series observed in the spectrum of the nitric oxide molecule [1]. The excitation takes place out of a single optically excited rotational level so that there are mainly three allowed Rydberg series observed converging to two different rotational states of the cation.

1.2. *The classical model*

Some insight into the properties of a high-n molecular Rydberg state can be gained by using the classical Bohr model of the hydrogen atom to estimate the properties of the Rydberg electron. Although such a model might seem outdated, recent experiments, as reviewed in [2], have shown that short-pulse lasers can be used to create Rydberg wavepackets that orbit the nucleus in a manner very close to that predicted by the classical model. Table 1 lists some of these classical properties for principal quantum number $n = 100$. The classical orbit period (1.5×10^{-10} s), which scales with n^3, is seen to be longer than the characteristic vibrational period (10^{-14}–10^{-13} s) and even longer than the rotational period of small molecules (10^{-12}–10^{-10} s) and therefore the behaviour of the Rydberg electron is sometimes described as the 'inverse Born–Oppenheimer regime'. Effectively the separation of timescales implies that there can be no rapid readjustment of the electronic distribution to the nuclear motion, as occurs when the Born–Oppenheimer approximation is applicable. The significance of this orbital time in the context of Rydberg molecules is that the decay of a Rydberg molecule can generally only occur via a collision between the Rydberg electron and the ionic core. In that sense the orbital period represents a minimum lifetime.

The orbital radius scales with n^2 and is of the order of 1 μm for $n = 100$. At atmospheric pressure, $\sim 10^7$ molecules would be contained within the volume of a sphere of this radius and would be found between the ionic core and the Rydberg electron if it were possible to create an $n = 100$ Rydberg state under these conditions. Given the large orbital radius, a Rydberg electron is extremely susceptible to collisional effects and also to external electromagnetic fields. With a binding energy of only 11 cm^{-1} the electron is ionized by an electric field of just 2.8 V cm^{-1}, but strong quantum-state mixing effects will occur at fields much lower than this (see section 3). The electron distribution is highly polarizable, the polarizability scaling with n^7, and this gives rise to the possibility for manipulating and controlling properties such as the lifetime, orientation and translational motion of the Rydberg molecule as shown in sections 3.7, 4.3 and 9.

The final property in table 1 does not come directly from the Bohr model, but reflects the quantization of angular momentum – for each n value the orbital angular momentum l takes values from 0 to $n-1$ and its projection m_l takes values from l to $-l$ adding up to an n^2 electronic degeneracy (i.e., 10 000 for $n = 100$). The energy

Table 1. Classical properties of an $n = 100$ Rydberg electron.

Property	$n = 100$	scaling
Orbital period	150 ps	n^3
Orbital radius	0.5 μm	n^2
Binding energy	11 cm^{-1}	n^{-2}
Field ionization	2.8 V cm^{-1}	n^{-4}
Electronic degeneracy	10 000	n^2

spacing between $n = 100$ and $n = 101$ in the hydrogen atom is $0.22\,\mathrm{cm}^{-1}$ and therefore, without considering any degeneracy of the ion core in Rydberg molecules, there are $\sim 10^5$ quantum states per cm^{-1}. Thus this region above $n = 100$ is often referred to as a pseudo-continuum, although as we show later, it is still possible to resolve individual quantum states spectroscopically in this region.

1.3. *Molecular Rydberg energy levels*

Equation (1) describes the energy levels in the limiting case where there is essentially no interaction between the Rydberg electron and the ion core. This is sometimes referred to as the Hund's case d coupling case. In the absence of the field the total angular momentum quantum number J and its projection M_J must be well defined and therefore in a diatomic molecule the Hund's case d quantum states can be labelled with the quantum numbers $|v^+, N^+, l, J, M_J\rangle$ where J takes values determined by the vector sum of the ion core angular momentum N^+ and the Rydberg electron angular momentum l, such that $J = N^+ + l, N^+ + l - 1, \ldots, |N^+ - l|$. (In this discussion we are ignoring the spins of the Rydberg electron and of the ion core, which are assumed for the purposes of simplicity to couple together to give a zero resultant.) In reality there will be a weak coupling between the Rydberg electron and the core rotational angular momentum – an electrostatic interaction with the core charge distribution – leading to small splittings of the energy levels of the same N^+, l but different J. This interaction can be treated as a perturbation which produces matrix elements between states with different N^+ (and possibly l) but the same J and the same parity (see for example [3–5]). When perturbing levels belonging to different Rydberg series become accidentally close, strong perturbations from the simple formula (1) might occur.

At lower n the electrostatic interaction with the ionic core becomes stronger, and a gradual transformation to a Hund's case b coupling case takes place. In this limit the Rydberg orbital angular momentum becomes coupled electrostatically to the ion-core molecular axis and the quantum number representing the projection along this axis, λ, becomes well defined. The states of different N^+ are so strongly mixed that this quantum number is no longer 'good' and in the Hund's case b limit (again ignoring electron spin) the defined quantum numbers are $|v, l, \lambda, J, M_J\rangle$. To a first approximation the Rydberg energy levels are given by

$$E = I_0 - \frac{R}{(n - \delta_{l\lambda})^2} + E_v + B_{vl\lambda}[J(J+1) - \lambda^2]. \tag{2}$$

In this case a series of rotational energy levels is built on each vibronic level associated with values l, λ and v. Although the transformation between Hund's cases d and b varies with the molecule and with l, a rough guide for low-l states is that at n values around 3–5 Hund's case b is likely to be a good description, while above $n = 10$ Hund's case d is likely to be a more appropriate starting point. These ideas can be extended in principle to non-linear molecules or to systems where the spin or electronic angular momentum of the ion core must also be considered.

1.4. *Rydberg states in 'nature'*

In all the experiments described below, Rydberg states are created by laser excitation. However, Rydberg states can also be formed by impact of energetic electrons on neutral molecules and are likely to exist in extreme physical environments, particularly plasmas and flames. Furthermore, in ionized media such as the

upper parts of the Earth's atmosphere (ionosphere) or in interstellar gas clouds, the major mechanism for removal of electrons is dissociative recombination [6], in which a molecular cation recombines with an electron to form a neutral highly excited intermediate that subsequently predissociates to form fast neutral atoms or molecules. Recent calculations have shown [7, 8] that for the crucially important astrophysical process

$$H_3^+ + e^- \rightarrow H_3^* \rightarrow H + H_2 \tag{3}$$

the cross-section is strongly enhanced at collision energies corresponding to Rydberg states of the H_3 intermediate. Similar behaviour has been predicted for the dissociative recombination of other molecules such as HD^+ [9] and NO^+ [10], illustrating that it is the Rydberg states that play a key role as intermediates in this process.

Rydberg atoms have also been observed in thermal emission from insulating surfaces. For example the desorption of K Rydberg atoms from samples of an industrial potassium-promoted iron oxide catalyst has been studied [11], while $n = 5$ and 6 Rydberg atoms have been detected directly on such a surface by Stokes stimulated Raman spectroscopy [12]. Such observations have been linked to the formation of clusters of excited potassium atoms on the surface and the existence of an unusual long-lived phase referred to as 'Rydberg matter' involving bonding between circular Rydberg atoms within the two- and three-dimensional clusters [13].

2. High-resolution laser spectroscopy of molecular Rydberg states

The experimental study of Rydberg states is not a new subject; the Rydberg formula, essentially equation (1), was proposed in 1889 to describe the Rydberg spectra of alkali metals, and the Rydberg states of molecules have been studied at low resolution throughout much of the twentieth century. However, the high resolution and sensitivity provided by recent advances in laser equipment and experimental technique (including molecular beam cooling) have led to new levels of detail in Rydberg spectroscopy, renewing considerable interest in this field. In particular very high resolution is required to cleanly resolve the full rotational structure of Rydberg spectra even in very small molecules.

2.1. *Vacuum ultraviolet and multiphoton excitation*

In general the high Rydberg states of molecules are located at energies more than 7 eV above the ground state (with the exception of low-IP alkali-metal compounds) and therefore their study is experimentally more challenging than the study of valence excited states in the visible or near-ultraviolet (UV) region. Three approaches are possible (see figure 4), although the third has been rarely employed: (a) single-photon excitation in the VUV; (b) multiphoton excitation (using longer-wavelength radiation); (c) excitation from a metastable electronically excited intermediate formed by, e.g., electron impact in a discharge. In many cases (b) has been employed recently, using two-laser double-resonant excitation via a suitable electronically excited intermediate state. The most important advantage of this kind of approach is that a single vibration–rotation level can often be selected as the intermediate state using the first laser, such that the number of Rydberg series that can be subsequently excited from that level using the second laser are restricted by the selection rules. This is potentially a very important advantage when dealing with polyatomic molecules with many degrees of freedom.

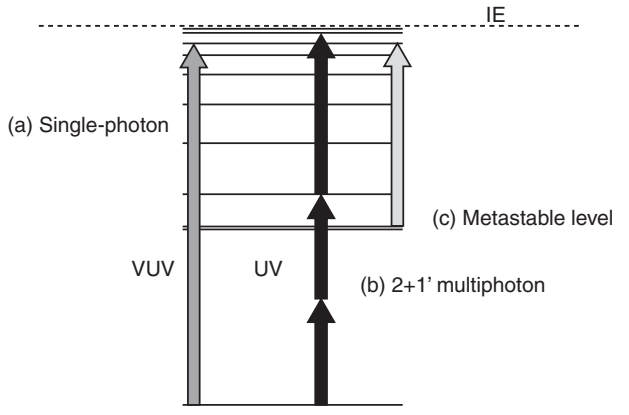

Figure 4. Excitation methods for spectroscopic study of Rydberg states: (*a*) single-photon VUV; (*b*) resonance-enhanced multiphoton using UV/visible lasers; (*c*) excitation in UV/visible from a metastable state prepared by non-optical means.

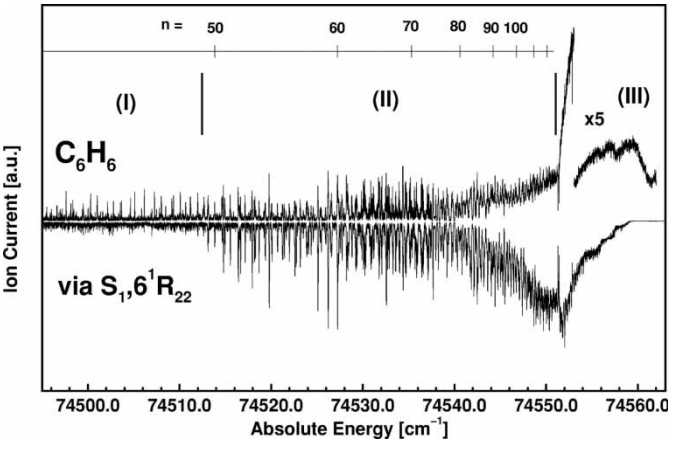

Figure 5. Very high-resolution Rydberg excitation spectrum of benzene, detected via $(1+1)$ two-photon excitation via a selected vibration–rotation level of the S_1 state (from ref. [14]).

For example, Neusser and coworkers have performed high-resolution studies on Rydberg states of benzene using pulsed lasers of near-Fourier-transform-limited bandwidth ($\sim$70 MHz), and as shown in figure 5 observed relatively simple series up to around $n = 100$ [14]. In this case the intermediate level is the S_1 valence state. In other cases a low-lying Rydberg state has been employed as the intermediate (e.g., NH_3 [15], H_2O [16], CO [17], NO [18], HCO [19]); this has the advantage that the molecular geometry in the intermediate state is very similar to that of the high Rydberg states and therefore the Franck–Condon factors for processes with $\Delta v = 0$ are very large compared to transitions off-diagonal in v, again simplifying the spectrum.

However, there are some disadvantages to the multiphoton excitation approach. Perhaps the most significant, when the highest resolution is required, is that the rate of decay of the intermediate state may be such as to compete with the rate of excitation to the high Rydberg states, and such as to cause significant

broadening of the transitions to the final states. This is particularly true for states with the potential for predissociation, which includes most of the low-n Rydberg states discussed above. Thus there is a need to use relatively high laser intensity in the second step of the double-resonant process so that the excitation rate exceeds the decay rate. This effectively reduces the intermediate state lifetime even more and leads to an additional 'power broadening' of the spectrum. The need for focused laser power may also lead to unwanted secondary processes producing background ions, which themselves perturb the highest Rydberg states and cause space-charge problems. The other main disadvantage of the multiphoton approach is the need to find a suitable intermediate state to act as a resonant state (although in a few cases non-resonant multiphoton ionization has been employed, such as in the two-photon spectrum of NH_3 [20]). While this may present no difficulty in the case of molecules that have been intensively studied in the past, such as NO, benzene, NH_3 or H_2O, it presents a much greater difficulty for the case of free-radicals, e.g., CH_2, where spectroscopic studies may be few and far between, or with some stable molecules such as CO_2 that have no known suitable intermediate states in the near-UV region. Finally the strong Franck–Condon propensity in favour of diagonal vibrational transitions, i.e., those with no change of v, when using a low-n Rydberg state as the intermediate could be seen as a disadvantage in that it may lead to some difficulty in accessing certain vibronic levels.

The use of single-photon excitation in the vacuum ultraviolet, figure 4(*a*), provides a useful alternative in that it bypasses the intermediate states to excite directly to the Rydberg states of interest. Although synchrotron radiation sources, and even classical grating spectrometers, have provided much useful information on Rydberg spectroscopy, e.g., [21, 22], neither of these can compete with the highest resolution achievable using laser-based sources. Methods for generating coherent vacuum ultraviolet radiation have been reviewed many times (e.g., [23–25]); these techniques are based on the non-linear optical frequency conversion of UV/visible lasers. Most useful is the sum- and difference-frequency mixing of two laser beams in a gaseous non-linear medium (quite often one of the rare gases) to generate the frequencies $2\nu_1 \pm \nu_2$, where in general the frequency ν_1 is tuned to be resonant with a two-photon excitation in the non-linear medium. For example, in krypton there are strong two-photon resonances at 94 093 and 98 856 cm^{-1} which are accessible using wavelengths of 212.56 or 202.31 nm from laser 1. Thus with laser 1 fixed at 212.56 nm, tuning laser 2 in the range 14 000–24 000 cm^{-1} generates a difference frequency in the range $2\nu_1 - \nu_2 \sim 70\,000$–$80\,000\ cm^{-1}$ and a sum frequency in the range $2\nu_1 + \nu_2 \sim 108\,000$–$118\,000\ cm^{-1}$. It is worth noting, however, that if laser 2 is a dye laser, scanning over such a range requires the use of more than 20 different dyes. A useful alternative approach to obtaining broad tunability is to use an optical parametric oscillator (OPO) source for laser 2 that allows rapid tuning over such a range.

The optimum resolution achievable from such a VUV source is illustrated by the setup in the laboratory of F. Merkt at Zurich [26] (see also the earlier setup of Kung and coworkers described in ref. [27]). In that case, the fundamental frequencies ν_1 and ν_2 are provided by a pair of pulse-amplified single-mode ring dye laser systems (see figure 6) each providing near-Fourier-transform-limited bandwidth pulses. Sum- or difference-frequency mixing of the outputs of these systems generates VUV radiation with a bandwidth of $< 0.01\ cm^{-1}$ in the range 80 000–120 000 cm^{-1}, a resolving power of 1 part in 10^7. Figure 7 shows a part of the very high-resolution

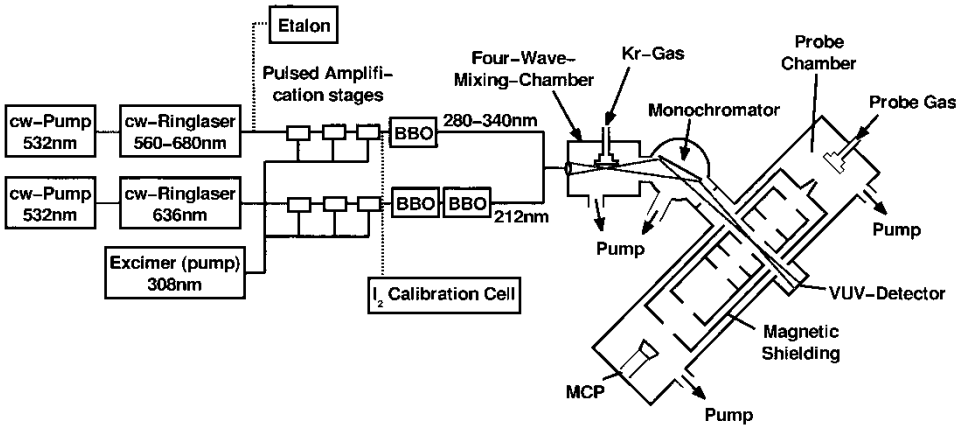

Figure 6. VUV laser system for very high-resolution photoionization studies (from ref. [26]). Two pulse-amplified single-mode ring dye lasers are sum-frequency mixed in a rare-gas non-linear medium to generate the VUV radiation.

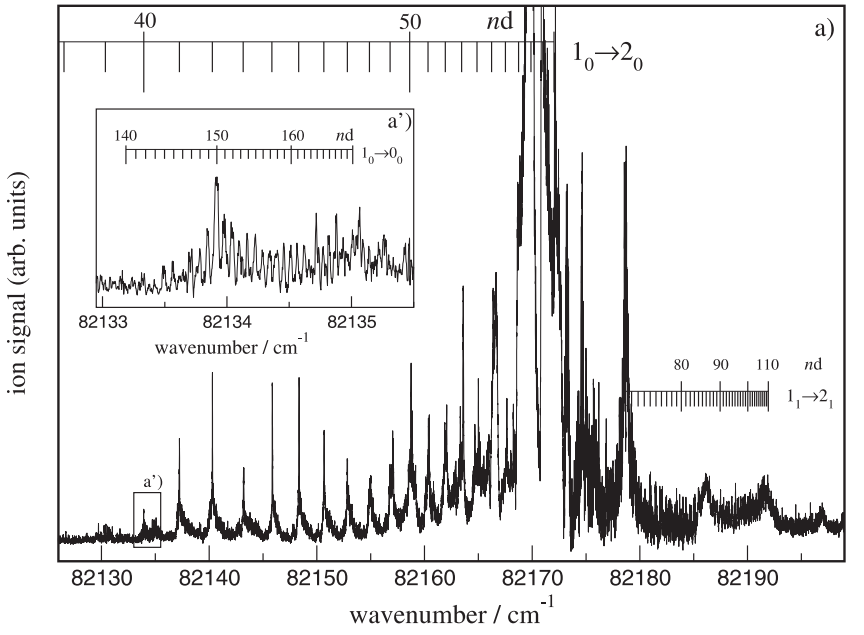

Figure 7. Very high-resolution one-photon photoionization spectrum of ammonia, obtained using the laser system in figure 6. The assigned series are labelled with the notation $(J''_{K''} \rightarrow N^+_{K^+})$ where N^+, K^+ represent the rotational quantum numbers of the threshold to which the series converge, and J'', K'' are the ground state quantum numbers (from ref. [28]).

photoionization spectrum of NH_3 recorded using this source and (see inset) showing clearly resolved Rydberg series up to $n = 170$ where the spacing between levels is just $0.04\,\mathrm{cm}^{-1}$ [28]. It is not only the resolution of closely spaced levels that is important here, but also the detailed measurement of linewidths and line shapes that reveal information about the dynamics of Rydberg state decay (see section 4). This spectrum also illustrates one of the disadvantages of the single-photon

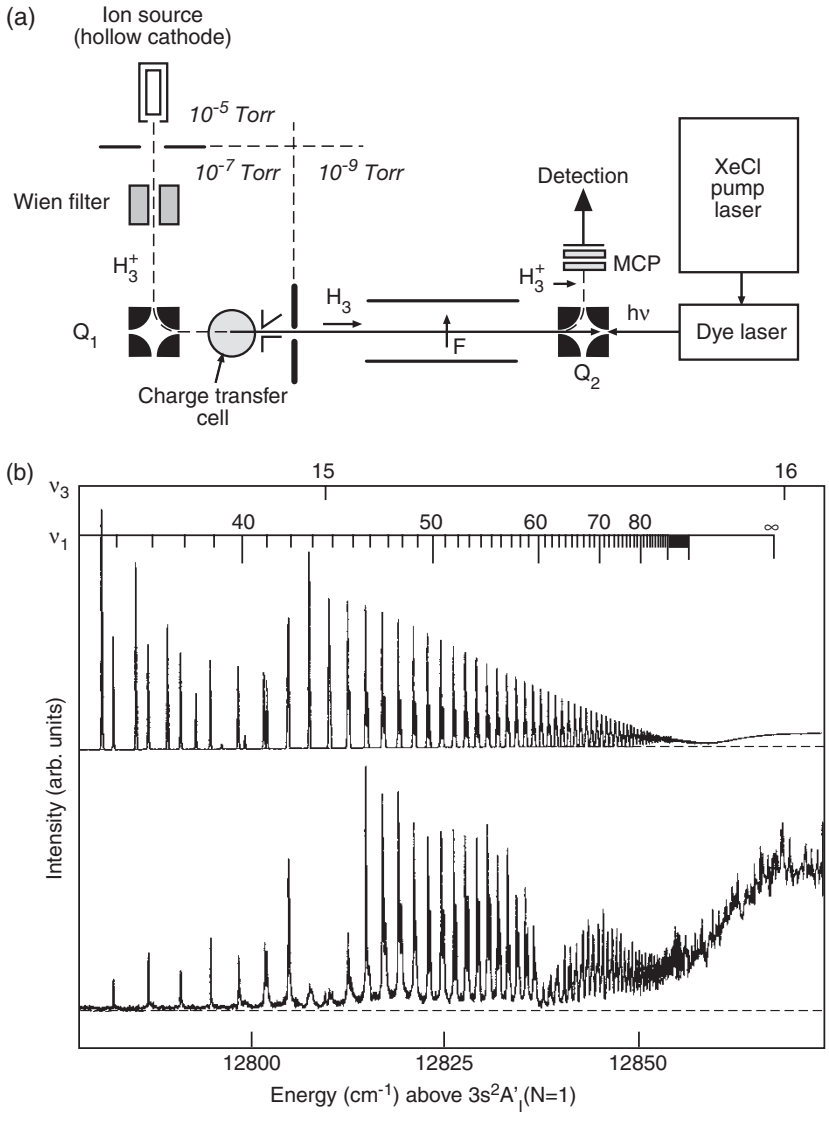

Figure 8. (*a*) Experimental setup for obtaining Rydberg spectra of H_3. A fast H_3^+ ion beam is neutralized in a charge-exchange cell after which the metastable H_3 molecules are excited by one or more collinear laser beams. Transitions are detected by field ionization in quadrupole Q_2 (from ref. [30]). (*b*) Experimental spectrum (bottom) and MQDT simulation of the *np* series of H_3 converging to the $N^+ = 1$ ionization threshold (Reprinted with permission from ref. [29], copyright (1991) by the American Physical Society).

excitation approach in that there are several superimposed Rydberg series observed, corresponding to excitation out of the different ground-state rotational levels that are populated in the molecular beam source.

A good example of the third approach to Rydberg spectroscopy mentioned above, i.e., formation of metastable excited molecules by non-optical means, is seen in the spectroscopy of H_3 performed by Helm and coworkers [29, 30]. In this case

H_3 molecules are formed in the metastable lowest rotational level of the $2p\ ^2A_2''$ Rydberg state by neutralization of a fast beam of H_3^+ ions in a cesium vapour cell, using the experimental setup shown in figure 8(*a*). Spectra of the *np* Rydberg series (figure 8(*b*)) are obtained by two-laser excitation via the intermediate 3*s* Rydberg states, while the *ns* and *nd* states are accessible by one-photon excitation in the near-UV. H_3 is an unusual case, not only in having a metastable state with such a long lifetime ($\sim$640 ns), but also in the fact that its ground state is unstable with respect to dissociation.

In general the most sensitive methods for laser spectroscopy of Rydberg states involve the *indirect* detection of absorption, usually by detecting ions or electrons that are produced either by photoionization, autoionization or field ionization of the excited states. Direct measurement of absorption is also possible using laser excitation as demonstrated recently by Sommavilla *et al*. who found that 1 part in 10^3 absorption in Ar and N_2, could be observed in a dual-beam VUV spectrometer [31]. After frequency up-conversion of UV laser radiation to the VUV, the VUV + remnant UV light was passed through a grazing-incidence monochromator, in which the first-order of the grating was passed through the sample while the -1th order was sent directly to a detector to normalize the VUV signal transmitted through the sample on a shot-to-shot basis.

2.2. *Millimeter-wave and infrared studies*

Ultimately the resolution achievable in the optical excitation of Rydberg states is likely to be limited by the Doppler effect, even when using excitation perpendicular to a supersonic beam. The highest resolution achieved to date in molecular Rydberg spectroscopy has been obtained using either microwave or millimetre-wave excitation between Rydberg energy levels as reviewed in ref. [32]. In this region of the spectrum, the Doppler contribution to the linewidth is many orders of magnitude smaller than in the VUV. In the experiments of Merkt and coworkers [33], H_2 molecules were excited to Rydberg levels around $n = 50$ by a double-resonant VUV-UV excitation through the $B^1\Sigma_u^+, v = 3$ intermediate state, and then the Rydberg molecules were exposed to the output of a millimetre-wave backward-oscillator source tunable in the range 120–180 GHz. The frequency of the millimetre waves is such as to drive transitions between nearby Rydberg levels, for example the $n = 51, 52$ to $n = 55, 56$ processes depicted in figure 9. It was found that the inter-Rydberg transitions were very easily saturated, having a strong transition probability, and the power broadening could only be eliminated by reducing the millimetre-wave intensity to a few nW cm^{-2}. Transitions were detected using selective field ionization, i.e., adopting a field-ionization pulse that would only result in ionization being detected through population of the upper states of the transitions (see section 3.5). With sub-MHz resolution, hyperfine structure was observed associated with the coupling of the nuclear spin angular momentum in the ion core to the rotation of the ion core. In effect the ionic rotational energy levels are split by the hyperfine interaction and thus to a first approximation different Rydberg series converge to different hyperfine levels giving rise to hyperfine splittings in the Rydberg spectrum. The hyperfine interaction was also observed to cause singlet–triplet mixing, and splittings due to the electron-spin—rotation coupling were resolved. Multichannel quantum defect theory (see below) has been adapted to treat this problem [34]. The ultimate limitation on resolution is due to the residence time of the molecules in the apparatus ($\sim$ tens of microseconds), and linewidths

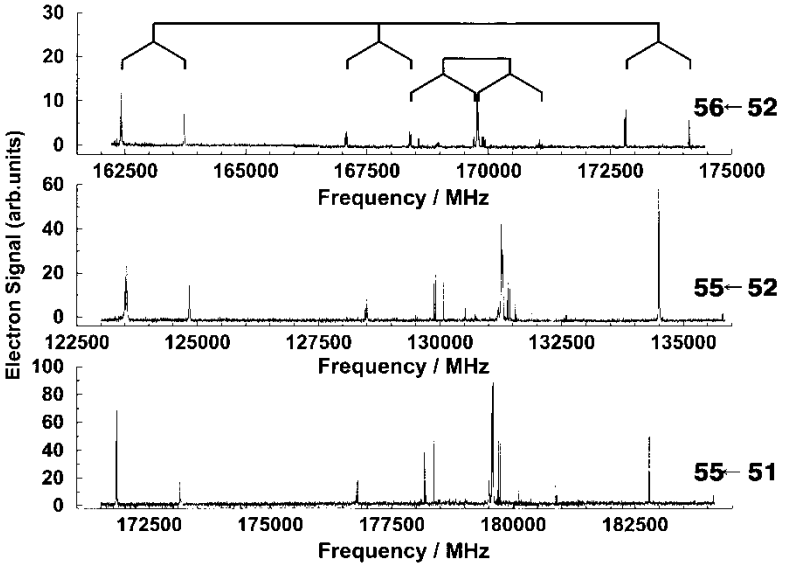

Figure 9. Millimetre-wave excitation spectrum of H_2 Rydberg states from the $N^+ = 1$, $51d, 52d$ levels populated by UV + VUV double resonant excitation (reprinted with permission from ref. [32], copyright (2002) by the American Physical Society).

as small as 60 kHz have been observed for Kr Rydberg states in a supersonic expansion. Section 9 describes current efforts to decelerate and trap molecules in Rydberg states which could allow the possibility of even higher spectroscopic resolution.

Infrared studies of the H_2 molecule Rydberg states have also been carried out using Fourier transform infrared (FTIR) by Herzberg and Jungen [35], and using diode lasers by Davies *et al.* [36]. H_2 molecules were formed in high-l states (e.g., the $5g, 6h$ or $8i$ states) in an AC electrical discharge and then could be excited to higher Rydberg states in the infrared region using a diode laser, or alternatively infrared emission could be observed from such levels. Doppler-limited resolution was obtainable (~ 0.01 cm^{-1}) to resolve detailed fine structure in these transitions. Qian *et al.* have recently demonstrated the possibility of using a combination of the advanced light source (ALS) synchrotron source for VUV excitation to the Rydberg states, combined with an infrared OPO laser to observe inter-Rydberg transitions [37]. This method was used to observe the np' and nf' autoionizing states of argon up to $n = 57$.

2.3. *The theoretical description of Rydberg spectra: multichannel quantum defect theory*

In section 1.3 we referred to the deviations from the simple equation (1) for the energy levels which arise because there is a finite probability of the Rydberg electron penetrating near, or inside, the region of the ion core electrons, and thus interacting with the core. In the core region the wavefunction cannot be described by the simple hydrogenic picture and therefore the ion core and Rydberg electron quantum numbers are not exact. The Hund's case b description is a more appropriate description of the angular momentum coupling in this region. This interaction with

the core gives rise to a perturbation and mixing between the various Rydberg series particularly at energies where members of two different series are almost degenerate. A useful physical view is that the Rydberg electron takes a classical trajectory into the core region where it exchanges energy and angular momentum with the core, and emerges with different quantum numbers on an altered trajectory, while the core quantum numbers are also changed. This inelastic scattering is equivalent to the mixing of Rydberg series.

The multichannel quantum defect theory (MQDT), first put forward by Seaton [38] and developed for molecular systems particularly by Fano [39], Jungen [40] and Greene [41], develops this scattering picture into a quantum mechanical framework for describing the Rydberg wavefunctions and energies. A good introduction to the theory can be found in the 'primer' article written by Ross [42]. A key feature of the energy region near the ionization threshold that must be incorporated is the existence of the ionization and dissociation continua that will be degenerate with the Rydberg series, and will play a controlling influence on the decay dynamics of the Rydberg states. The major advantage of MQDT is that it is able to treat the ionization continua and bound Rydberg states within a single formalism, while progress is also being made to include dissociation continua [43–46]. Each Rydberg series and the associated ionization continuum forms a single 'channel' which is labelled by the angular momentum quantum numbers of the Rydberg electron and the quantum numbers of the ion core. A channel describes one of the possible initial or final states of the inelastic scattering process. In the theory, the radial coordinate of the Rydberg electron is divided into two (or more) regions (see figure 10). In the outer region (II) the potential experienced by the electron is hydrogenic and the wavefunction can be described as a linear combination of Coulomb functions, the solutions of the hydrogenic Schrödinger equation. In the inner region (I) the potential is no longer hydrogenic and the electron interacts with the charge distribution of the ion core. For electrons that are relatively non-penetrating, e.g., those with $l \geq 3$, the interaction can be considered primarily as an external interaction with the ion core dipole or quadrupole. However, for more penetrating electrons (s, p, d) the Rydberg electron cannot be separated from the other electrons, and electron correlation and angular momentum coupling become important. The core region is sometimes referred to as the Born–Oppenheimer region because the

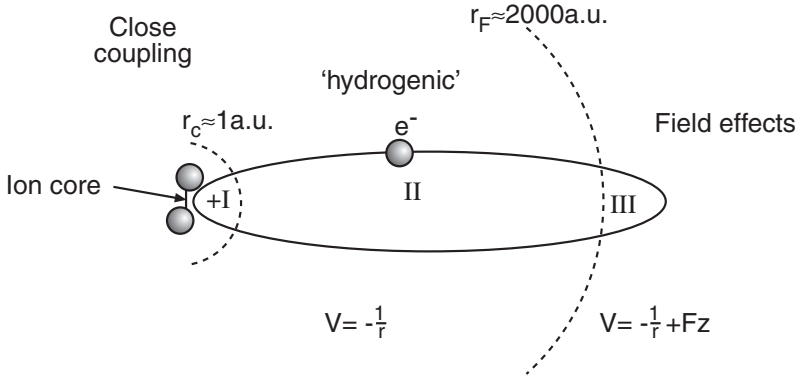

Figure 10. Multichannel quantum defect theory picture of a Rydberg molecule. I is the short-range 'Born–Oppenheimer' region, II is the Coulombic long-range region, and III is the region where external fields dominate.

timescale associated with the electron residence in this region is so short that the nuclei can be considered to be fixed, and the total electronic wavefunction has the character associated with excited valence states.

In MQDT a notional boundary is defined between the inner and outer regions. At that boundary the long-range description is valid and the wavefunction emerging from the core region must map on to a linear combination of regular and irregular Coulomb functions which may have components in many of the long-range channels. The wavefunction is written in terms of a scattering matrix K

$$\Psi = \sum_j Y^{(j)} \sum_i |i\rangle \big[f_i(r)\delta_{ij} - g_i(r)K_{ij} \big], \tag{4}$$

in which i, j represent particular channels, f_i and g_i are the regular and irregular Coulomb functions, and $Y^{(j)}$ is the wavefunction of the ion core multiplied by the angular parts of the Rydberg electron wavefunction. The off-diagonal matrix elements of the scattering matrix K effectively represent the strength of the interaction between the various channels. This K matrix is taken to be largely independent of energy (and hence principal quantum number) and it is considered to be valid both below and above any ionization threshold. In the theory the behaviour of the wavefunction in the core region is independent of energy, aside from a normalization factor and it is only in the long-range region where boundary conditions are applied. The approximate invariance of the K matrix with respect to total energy occurs because the potential and kinetic energies of the Rydberg electron are very large in the core region (and are of opposite sign), such that the magnitude of the total energy is much smaller than either. Thus the behaviour in the core region is barely affected by a small change in total energy.

Fano pointed out [39] that diagonalization of the K matrix is in some respects analogous to diagonalization of the Hamiltonian matrix and the eigenvectors $Q_{i\alpha}$ form a matrix which represents a frame transformation between the short-range and long-range regions:

$$K_{ij} = \sum_\alpha Q_{i\alpha} \tan(\pi\mu_\alpha) Q^t_{j\alpha}; \tag{5}$$

for example, for a diatomic molecule this represents a transformation between a Hund's case b coupling scheme and a Hund's case d basis. The diagonalized eigenvalues of the matrix are written as $\tan(\pi\mu_\alpha)$ where the μ_α are known as the eigenchannel quantum defects and represent the phase shifts of the wavefunctions at the boundary of the core region, relative to those in the hydrogen atom. These eigenchannel quantum defects can be considered to be the fundamental input parameters into the multichannel quantum defect theory. Strictly speaking these parameters are dependent on the internuclear distance(s) and bond angles; the instantaneous interaction of the Rydberg electron with the ion core occurs at fixed geometry. The averaging over vibrational wavefunctions is incorporated into the frame transformation matrix; for example for a diatomic molecule this would be in the form

$$K_{ij} = \sum_\alpha Q_{i\alpha} \langle \chi_i(R) | \tan(\pi\mu_\alpha(R)) | \chi_j(R) \rangle Q^t_{j\alpha}, \tag{6}$$

where $\chi_{i,j}(R)$ are the vibrational wavefunctions of the ionic core (but see ref. [47] for a discussion of alternative formalisms).

In order to calculate an absorption spectrum or a partial photoionization cross-section using MQDT, one needs to have knowledge of the K matrix and also an associated dipole vector **d**, which itself may be expressed in terms of a dipole matrix in the eigenchannel basis

$$d_i = \sum_\alpha Q_{i\alpha} d_\alpha. \tag{7}$$

In effect the transition dipole moments d_α represent the physical reality that the excitation takes place primarily in the core region where the overlap with the ground state wavefunction is greatest. Explicit expressions for the transition probability in terms of K are given for example in refs [43, 48].

Multichannel quantum defect theory has been applied to the interpretation of the Rydberg spectra of a number of small molecules: H_2 [48], NO [49], H_2O [50], N_2 [51], Li_2 [52], H_3 [53], Na_2 [54], HCO [55], HBr [56], CaF [57]. In our own work we have shown that it can be adapted for calculating rotational line intensities in ZEKE spectroscopy (see section 5.3) of H_2 [48] and NH_3 [58, 59]. In some of these cases the K matrix elements (or the associated quantum defects and transition dipoles) have been regarded as a set of input parameters to be determined by iterative adjustment to match the observed spectra. A first guess for some of the eigenchannel quantum defects is obtainable by using the experimentally determined quantum defects for the low-n states (those behaving as Hund's case b). In other cases the K matrix has been calculated by *ab initio* methods. For the *ab initio* approach, Jungen and Ross [60] have used the *ab initio* potential energy curves calculated for the bare H_2^+ ion and those calculated for the low-lying Rydberg states to derive an R-dependent quantum defect matrix. Child and Hiyama have pointed out the advantage of using an R-matrix *ab initio* approach to calculate the K matrix directly [61], bypassing the calculation of potential energy curves. Fielding and coworkers [2] and subsequently Jungen and coworkers [62] have developed a time-dependent formulation of MQDT so that wavepacket motion in Rydberg states can be simulated. The real-time competition between autoionization and predissociation has been modelled in this way [62].

3. Molecular Rydberg states in external fields: theory and experiment

Many, if not all, of the applications of molecular Rydberg states described below in sections 5–9 take advantage of the sensitivity of the Rydberg electron to an external electric field. Even at low electric field strengths the energy levels may be strongly perturbed and the very high degeneracy associated with the n^2 possible combinations of l and m_l is lifted. At high field strengths the phenomenon of field ionization occurs. In both these field-strength regions there is a close analogy between the behaviour of molecular Rydberg states and that of the hydrogen atom. We therefore proceed with a brief review of the properties of the H atom in a field before highlighting the subtle differences for molecular Rydberg states.

3.1. *The Stark effect in the hydrogen atom*

Figure 11 shows how the potential energy of an electron in the H atom changes in the presence of an electric field along a line that passes through the nucleus and is parallel to the field direction. The Coulombic potential is changed by the addition of a term Fz for a field along the z-direction and this raises the electronic potential

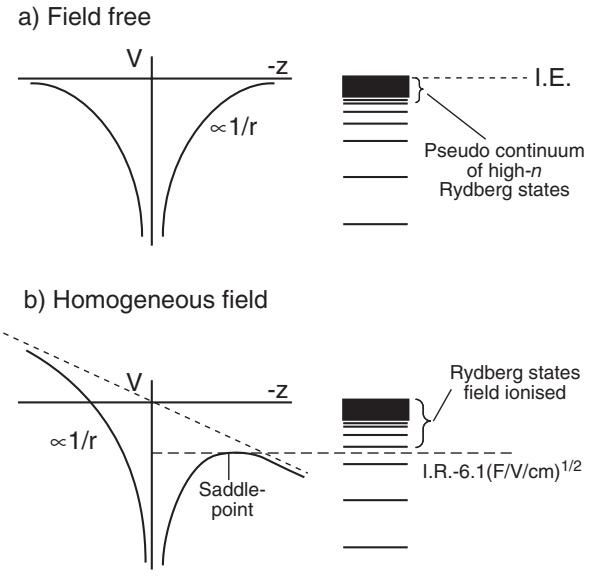

Figure 11. Potential of an electron in a hydrogen atom along the z-axis (*a*) in absence of a field (Coulombic potential), and (*b*) in the presence of a field directed along the z-axis.

for $z > 0$ and lowers it for $z < 0$. $V(z)$ tends to $-\infty$ as $z \to -\infty$, and a maximum in $V(z)$, which is actually a saddle point in the full three-dimensional space, occurs at $z = -F^{-1/2}$ for which $V(z) = -2F^{-1/2}$ (in atomic units). Classically the maximum in the potential barrier corresponds to the field-modified ionization threshold and this is equal to $I_0 - 6.12\sqrt{F}$ in wavenumber units (cm^{-1}) with F in V cm^{-1}. In quantum mechanics the possibility of the electron tunnelling through the barrier means that all the energy levels supported by the potential (even the ground state) are only metastable with respect to ionization, although in reality the lifetimes with respect to decay by tunnelling are extremely long except for all but the levels very close to the saddle point.

The above arguments suggest that if a given electronic state is initially populated in the absence of an electric field and then a field is subsequently switched on which lowers the ionization threshold below the energy of that state, then the electron changes from being bound to unbound and the atom is field-ionized (see figure 11). In reality this picture is an oversimplification even for the H atom because it does not take into account the behaviour of individual energy levels as the field rises.

Quantum mechanically the effect of the field is to add an additional term Fz to the Hamiltonian. The Schrödinger equation for the H atom is separable in the presence of an electric field provided a change to parabolic coordinates is carried out [63, 64]:

$$\xi = r + z, \quad \eta = r - z, \quad \phi = \arctan(y/x). \tag{8}$$

The wavefunctions may thus be written

$$\Psi(\xi, \eta, \phi) = (2\pi\xi\eta)^{-1/2} f_{n_1 m}(\xi) g_{n_2 m}(\eta)\, \mathrm{e}^{\mathrm{i}m\phi} \tag{9}$$

and are now defined by the quantum numbers n, m, n_1 and n_2, where n_1 and n_2 represent the number of nodes in the separated parts of the wavefunction. As these two quantum numbers are always linked by the relationship $n_1 + n_2 + |m| + 1 = n$,

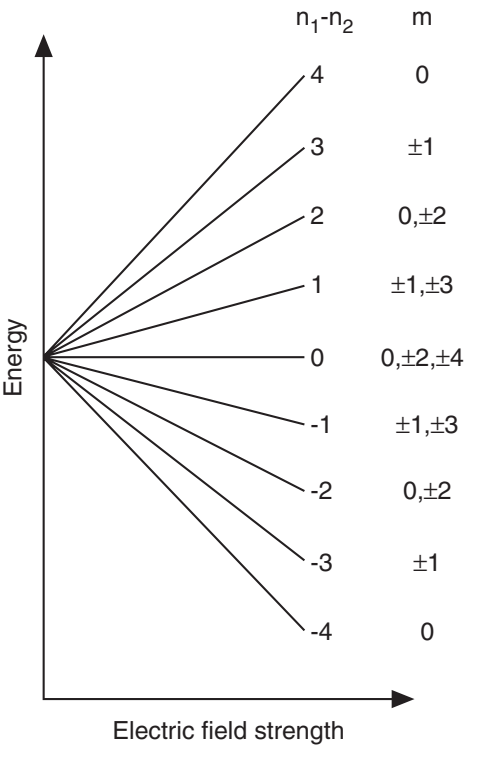

Figure 12. Energy levels of the H atom in an electric field for $n = 5$. The levels are labelled with the parabolic quantum number $k = n_1 - n_2$ and the degenerate m states are listed for each k.

it is convenient to define a new quantum number $k = n_1 - n_2$ such that for given n and $|m|$, the quantum number k takes the values $n - |m| - 1$, $n - |m| - 3$, ..., $-(n - |m| - 1)$. l is no longer a good quantum number and each of the Stark eigenstates is a mixture of all possible l values. Figure 12 illustrates the energy levels that are obtained, which are given approximately by the series expansion [64, 65] (in atomic units)

$$E = -\frac{1}{2n^2} + \frac{3}{2}F(n_1 - n_2)n - \frac{1}{16}n^4[17n^2 - 3(n_1 - n_2)^2 - 9m^2 + 19]F^2 + \cdots \qquad (10)$$

An exact solution is not obtainable in analytical form. At modest electric fields the linear term dominates the expansion.

The predominantly linear variation of energy with field implies that a dipole moment is created in the atom in a given eigenstate which does not vary significantly with the applied field. This is really akin to a *permanent* dipole moment rather than an induced dipole moment and the magnitude is *not* directly related to the polarizability. Figure 13 shows the wavefunctions that correspond to the Stark states $k = -7$ to $k = +7$ for $n = 8$ of the hydrogen atom and the existence of the dipole displays itself in the lopsided distribution of electric charge, in contrast to the symmetrical distributions for states of well-defined l at zero field [66]. For the states that increase in energy in the field ('blue-shifted Stark states', k negative) the electron density is located in the positive z-region where the potential energy is high, whereas

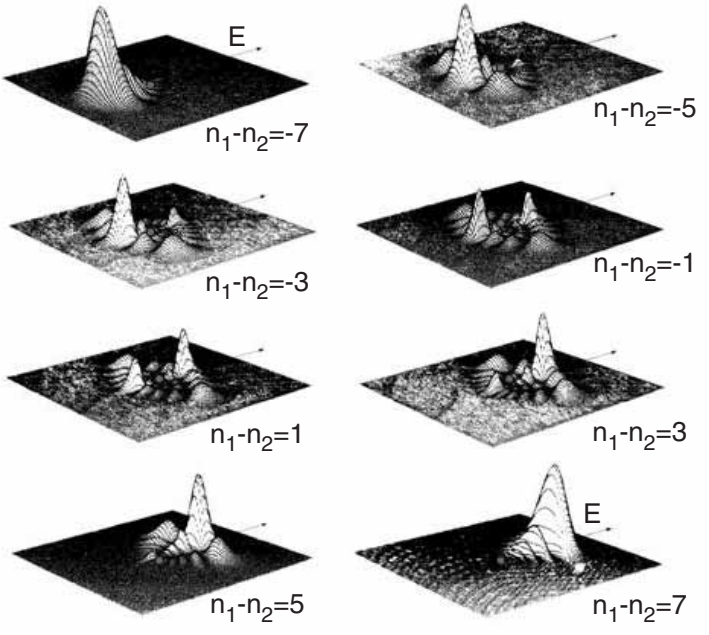

Figure 13. Electron density plots of the H atom wavefunctions in the zx-plane for the $n = 8$ Stark states ($m = 0$) labelled with the parabolic quantum number k (from ref. [67]).

Table 2. Calculated field-ionization characteristics and Inglis–Teller field of Rydberg states with different principal quantum numbers: the adiabatic field ionization limit obeys the relationship $E_n = 6.12\sqrt{F_{\text{adiabatic}}}$ and the diabatic field ionization limit, $E_n = 4.6\sqrt{F_{\text{diabatic}}}$.

n	$E_n(F=0)$ (cm^{-1})	$F_{\text{adiabatic}}$ (V cm^{-1})	F_{diabatic} (V cm^{-1})	Inglis–Teller field (V cm^{-1})
5	–4390	514 000	911 000	575 000
10	–1100	32 200	56 900	18 000
15	–488	6350	11 200	2370
25	–175	823	1460	184
50	–43.9	51.4	91.1	5.75
100	–11.0	3.22	5.69	0.180
150	–4.88	0.635	1.12	0.0237
200	–2.74	0.201	0.355	0.005 62

for the red-shifted states (k negative) it is located in the negative z-region where the potential is low.

The most blue-shifted energy level associated with a given principal quantum number n crosses the most red-shifted level associated with quantum number $n+1$ at a field known as the *Inglis–Teller field*; if only the linear term in the expansion of equation (10) is considered this crossing occurs at a field of

$$F_{\text{IT}}/\text{V cm}^{-1} = 1.798 \times 10^9 n^{-5}. \tag{11}$$

The values of F_{IT} for a range of n values are listed in table 2. Uniquely in the H atom, the symmetry is such that this is a *real* crossing of energy levels not an avoided

crossing (the z-component of the Lenz–Runge–Pauli vector is uniquely a constant of the motion for the H atom [67, 68]).

If the second- and higher-order terms of equation (10) are ignored then the degeneracy of the Stark states associated with different m values increases on moving from the outside to the centre of the manifold, i.e., those levels for which $|k|$ is smallest have the highest degeneracy. As will be pointed out later (section 3.8), the effect of an inhomogeneous field could be to mix these m_l states, an effect which may be greatest for those levels with small $|k|$.

3.2. *Diabatic field ionization*

A correct description of field ionization takes into account the behaviour of individual energy levels as described above. For the H atom, as the crossings of the energy levels are real as opposed to avoided, the system will pass through these crossings *diabatically* as the field rises. For the blue-shifted Stark state, the energy rises and will reach the energy of the classical ionization threshold at a relatively low field. However, the wavefunction is highly localized away from the region of the saddle point and such a state is metastable with respect to ionization. Damburg and Kolosov give an analytical expression for the lifetimes of H-atom Stark states [65] (see also [69]). As the field rises more, the saddle point moves further to the left in figure 11(*a*) increasing the probability density of the blue-shifted state near the saddle-point region. Calculation using Damburg and Kolosov's formula shows [70] that the field $F/\mathrm{V\,cm^{-1}}$ needs to rise to $\sim\sqrt{F} = E_0/3.1$, where $E_0/\mathrm{cm^{-1}}$ is the zero-field energy of the level, in order for the rate of ionization of a blue-shifted level to increase to a measurable value ($> 10^9\ \mathrm{s^{-1}}$). (According to Hollenstein *et al.* [71] the more appropriate value to use is $\sqrt{F} = E_0/2.4$ for n values greater than 100, based on variational calculations of Herrick [72].) For a red-shifted Stark state the energy moves down with increasing field, tending to stabilize the state energetically, but the lowering of the ionization threshold occurs at a greater rate with respect to the increasing field. For the most extreme red-shifted state the field has to be raised to $\sim\sqrt{F} = E_0/4.6$, in order for the energy of the Stark-shifted state to be above the barrier. The wavefunction is highly localized near the barrier and therefore the ionization rate becomes very fast as soon as ionization becomes energetically possible (and indeed some tunnelling may be possible just below this barrier).

If all the Stark states of given n are populated with equal probability, then all of these would be ionized for $\sqrt{F} > E_0/3.1$, while a decreasing fraction would be ionized for fields in the range $\sqrt{F} = E_0/3.1$ to $E_0/4.6$. Below $\sqrt{F} = E_0/4.6$ none of the states are ionized at a measurable rate. The ionization probability of the entire Stark-state population for given n varies with field as shown in figure 14(*a*). Alternatively we can also plot how the ionization probability for the full set of Stark states varies with E_0 (and hence with n) at fixed field, and the result obtained is shown in figure 14(*b*). This figure shows how the pulsed-field ionization signal for the H atom would, in a given field, vary as the excitation frequency was scanned towards the ionization threshold, assuming the pseudo-continuum of Rydberg states is unresolved.

3.3. *The Stark effect in non-hydrogenic systems*

Figure 15 shows a 'Stark map' for the krypton atom [73], illustrating how the energy levels vary with field. There are several new complications introduced compared to the hydrogen atom.

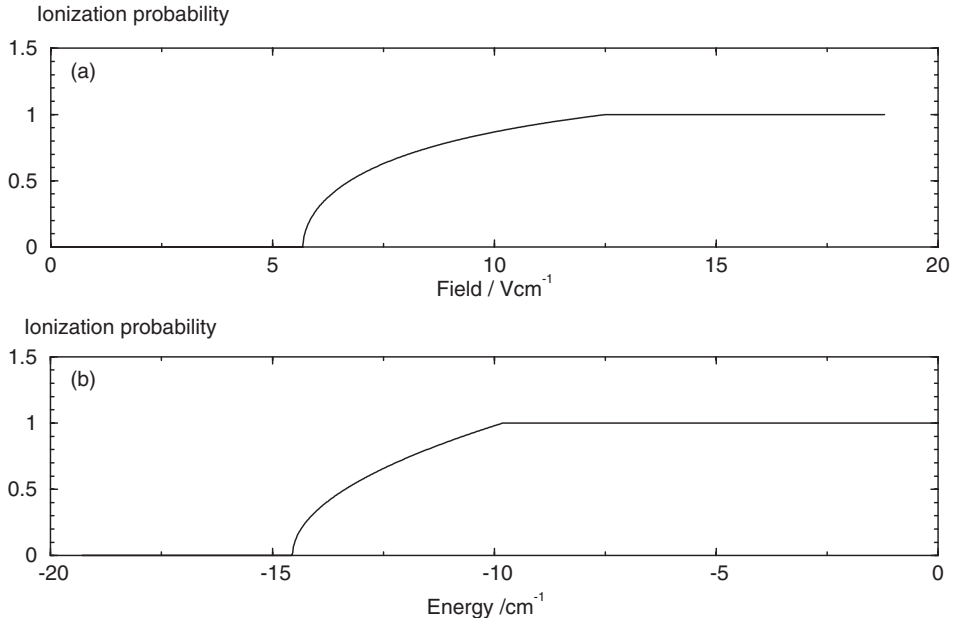

Figure 14. Total field ionization probability for the H atom (*a*) as a function of applied field for the full set of Stark states of $n = 100$, and (*b*) at fixed field ($10\,\mathrm{V\,cm^{-1}}$) as a function of the zero-field energy of the set of Stark states. It is assumed that a field ionization rate slower than $10^9\,\mathrm{s^{-1}}$ means that a level is not field-ionized on the experimental timescale.

1. The Runge–Lenz symmetry of the problem is broken in such a way that crossings between energy levels with the same values of M_J now become *avoided* crossings rather than real crossings, although the energy gaps at the avoided crossings are generally too small to be observed on the scale of figure 15. In effect, all states of given M_J become interacting and the eigenfunctions in the field are linear combinations of all possible zero-field wavefunctions.
2. The low-l Rydberg states are not degenerate at zero field with the high-l states because of the non-zero quantum defects. The Stark shifts of the low-l states can be treated using second-order non-degenerate perturbation theory at low field giving a Stark shift that is quadratic with the field:

$$\Delta E(F) = \sum_{nl'} \frac{\langle nl|Fz|nl'\rangle\langle nl'|Fz|nl\rangle}{E_{nl} - E_{nl'}}. \tag{12}$$

The high-l states on the other hand are almost degenerate with each other, as in the H atom, and therefore these show a hydrogenic behaviour even at very low fields, i.e., the energy shift is proportional to the field. At higher fields the magnitude of the Stark perturbations becomes comparable with the zero-field energy-level splittings between the high-l and low-l states, and the low-l states become merged into the behaviour of the high-l manifold, showing linear Stark shifts. However, at intermediate fields the behaviour can be complex if the quadratically shifted low-l states cut through the linear-shifted Stark manifold. This can lead to quite sharp changes in the eigen-

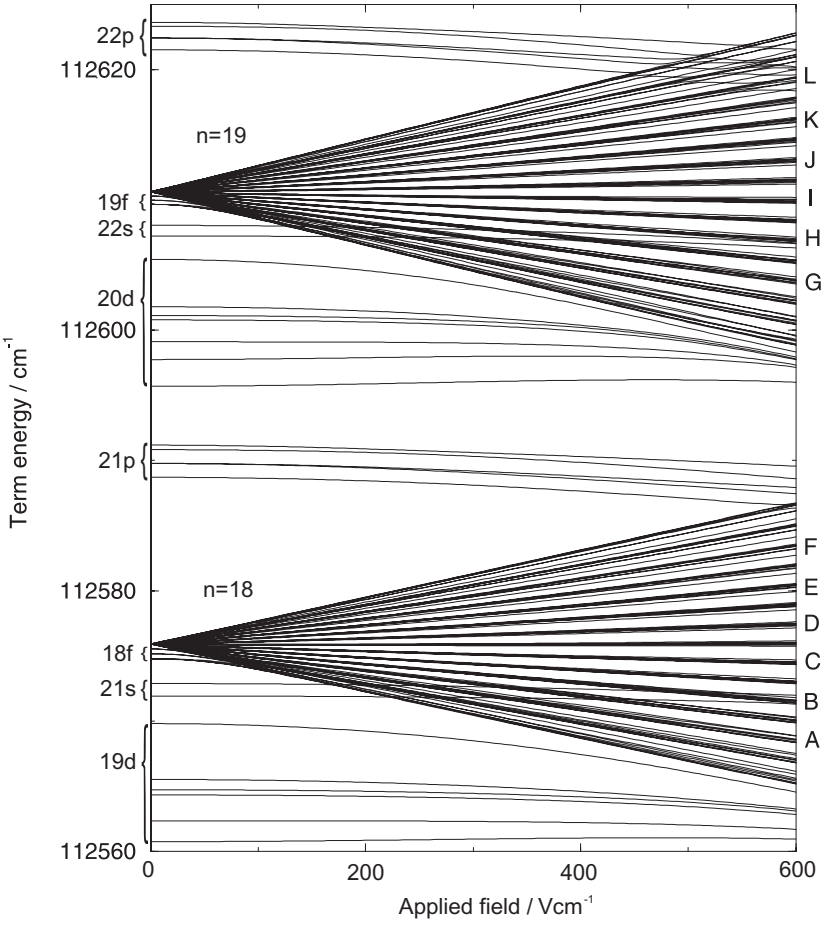

Figure 15. Calculated Stark map for the $n = 18, 19$ levels of krypton (from ref. [73]).

functions near the avoided crossings, with significant effects on the dynamics in a rising field.

3. In a *homogeneous* field, only the M_J quantum number, representing the projection of the total angular momentum, is conserved; this does not necessarily imply conservation of m_l because of the possible contribution from the core angular momentum. A state with given M_J can be written as a sum over decoupled states:

$$|j_{\text{core}}, l, s, J, M_J\rangle = \sum_{m_j, m_l, m_s} c_{m_j, m_l, m_s} |j_{\text{core}}, m_j, l, m_l, s, m_s\rangle. \tag{13}$$

The contribution of each m_j, m_l, m_s combination to an eigenstate will change as the field rises, due to mixing between states of the same M_J and eventually the eigenstates will correspond predominantly to one m_j, m_l, m_s combination; the effect of a strong field is to *decouple* the angular momenta that were originally coupled internally at zero field.

4. The Stark manifolds show additional fine structure. The nature of the splittings evolves as the field changes, because of the change from the coupled to decoupled regime as described in (3) above. For example, at

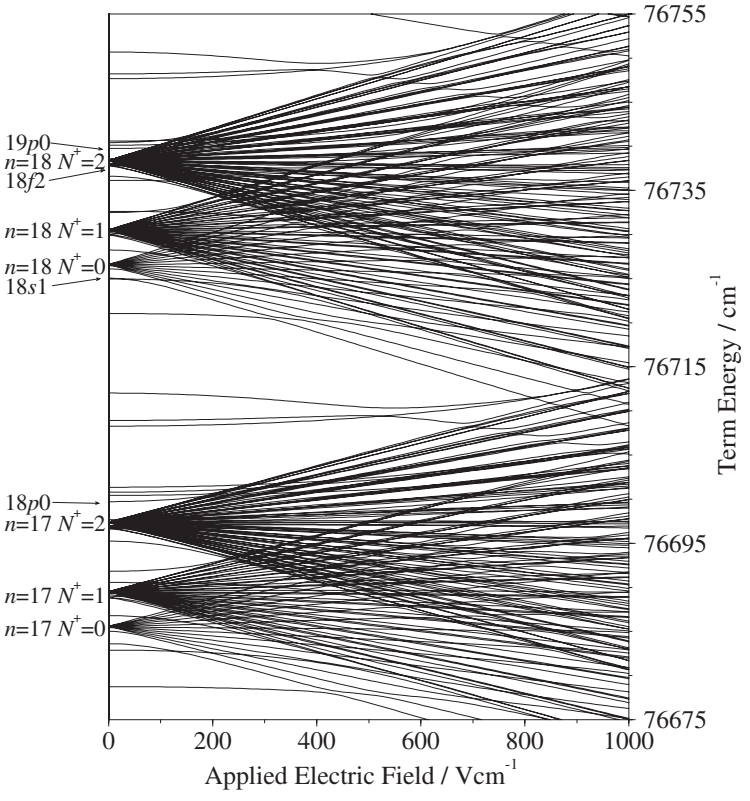

Figure 16. Calculated Stark map for nitric oxide $M_J = 0$ showing $n = 17, 18$ levels for $N^+ = 0 - 2$ only (from ref. [1]).

zero-field in the heavier rare gases the coupling of $j = 3/2$ to the l of the Rydberg electron leads (in the *jl* coupling scheme) to states with resultant quantum number K having values $l + 3/2, \ldots, l - 3/2$. The spin of the Rydberg electron then couples to give states of well-defined J having values $K \pm 1/2$. The states with the same l but different K, J have slightly different energies and this splitting is largest for the low-l states (see the low-field region of figure 15). These internal couplings therefore cause splittings at low field of states with significant low-l character. At high field, the effect of the applied field is to decouple these angular momenta so that the quantum numbers m_j, m_s and m_l are well defined, such that for given M_J $(= m_j + m_s + m_l)$ the energy levels split primarily according to the possible values of m_l. For example in the argon atom, if $M_J = 0$ then for $j = 3/2$, the sum $m_j + m_s$ takes values from $+2$ to -2 and therefore the m_l values can range also from -2 to $+2$. The energy levels are seen to split into several sets according to the possible m_l, m_j, m_s combinations. The different energies arise at high field because, for example, the *ns* and *np* wavefunctions cannot contribute to the $m_l = 2$ states, and the *ns* cannot contribute to the $m_l = 1$ states. At intermediate fields there must be a gradual transition from the zero-field coupling to the high-field coupling, but in any case some splittings of the levels will occur.

Figure 16 illustrates the Stark map for the NO molecule [1], showing a further complication that is introduced: each rotational state of the ion core has its own associated Stark manifolds and the many manifolds cross and show weak avoided crossings. Nevertheless the Stark shifts remain predominantly linear as in the H atom. The external field itself cannot directly mix states with different core rotational quantum numbers. However, the core quantum numbers may not be entirely 'good' quantum numbers at zero field – for example, the *np* states which are nominally $N^+ = 2$, $J = 1$ in NO have a small degree of *np*, $N^+ = 0$, $J = 1$ character, and therefore when the $N^+ = 0$ and 2 Stark manifolds cross, there can be a non-zero interaction and an avoided crossing.

3.4. *Experimental measurements of the Stark effect*

The Stark effect has been measured in the Rydberg states of a number of atoms, mainly rare-gas atoms [74, 75, 76, 77], alkaline earth metals [78, 79] and alkali metals [80, 67] and for a few selected molecular Rydberg systems: H_2 [81, 82], Li_2 [83], NO [1, 84] and H_3 [30]. In molecular systems it is generally preferable experimentally to populate the Rydberg states in two-colour excitation via an intermediate resonant level. The selection of a specific vibration–rotational intermediate level restricts the number of core rotational states (and hence the number of Stark manifolds) that will be accessed, simplifying the potentially complex

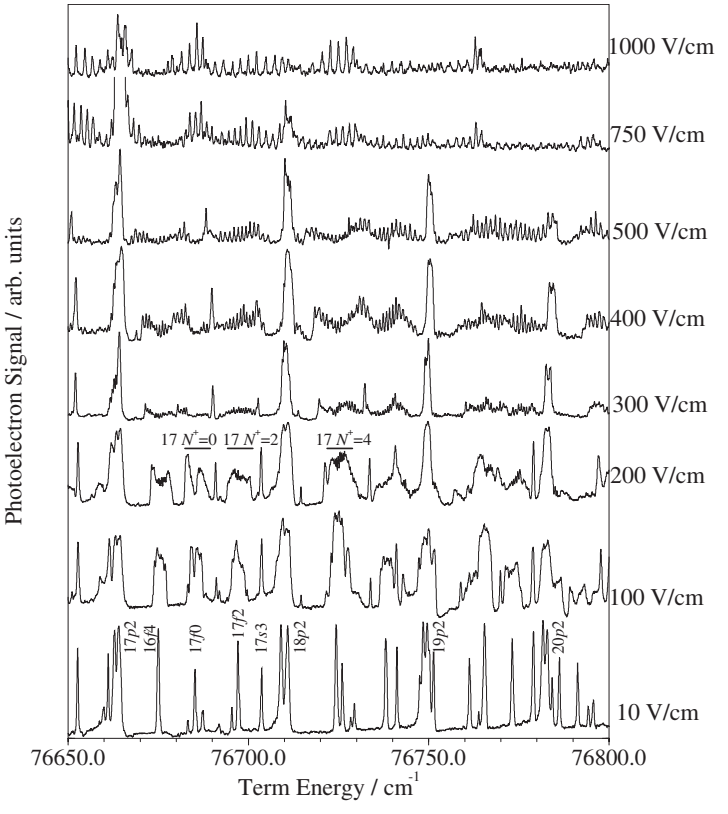

Figure 17. Experimental Stark spectra for nitric oxide excited from the $v = 1, J = \frac{5}{2}$ level of the $A^2\Sigma^+$ electronic state (from ref. [1]).

spectra. The Stark spectra for NO [1] recorded through excitation via the $A^2\Sigma^+, v = 1, N = 2,\ J = 5/2$ level are shown in figure 17. At zero field the predominant transition probability from this intermediate is to the *np* ($N^+ = 2$) and *nf* ($N^+ = 4$) states. As the field increases the $ns/nd, N^+ = 2$ levels start to appear in the spectrum through intensity borrowing from the *np* states, while at relatively low fields the *nf* states are readily mixed with the high-*l* Stark manifolds, through which the manifolds gain sufficient intensity to appear in the spectrum. It will be noticed that the low-*l* states associated with the $N^+ = 2$ core do not readily mix with the $N^+ = 4$ high-*l* states even when they are almost degenerate; for example the $17p2$ state is still clearly visible at $500\,\mathrm{V\,cm^{-1}}$ even though it is overlapped by the $n = 16$, $N^+ = 4$ high-*l* manifold. This mixing can only occur when the manifold acquires sufficient $N^+ = 4$ low-*l* character to mix with these low-*l* states of different N^+.

For the case of autoionizing Rydberg states, it is generally observed that broad lines (usually of low-*l* character) become sharper as the field is increased, while the high-*l* states apparently broaden. The mixing of states of different *l* in the field changes the coupling to the continuum as discussed in more detail below (section 4).

3.5. *Field ionization in non-hydrogenic systems*

The occurrence of *avoided* crossings in non-hydrogenic systems has a significant effect on the mechanism for field ionization. As the field rises and a given energy level approaches an avoided crossing the system has a choice of either jumping the energy gap diabatically, or following the avoided crossing adiabatically. If the diabatic behaviour dominates we would expect the field ionization characteristics to be very similar to the H atom. The field ionization behaviour of the entire Stark manifold would recreate the trend shown in figure 14. In the adiabatic extreme, however, if the system follows every crossing adiabatically, then it will take a zigzag, but almost horizontal, path across the Stark map as it moves through a sequence of avoided crossings, alternating between red-shifted and blue-shifted states (as illustrated for example in ref. [69], fig. 5). As a consequence the energy remains roughly constant at the zero-field value, E_0. Once the saddle point in the potential is lowered to this energy at a field given by $\sqrt{F} = E_0/6.1$, the system will rapidly field-ionize as soon as it makes a switch into a red-shifted Stark state (the blue-shifted Stark states are metastable; see above). This behaviour is generally referred to as 'adiabatic field ionization' as distinct from the hydrogenic 'diabatic field ionization'. Which of these two mechanisms is observed can be determined by consideration of the Landau–Zener theory [70, 85], which shows that the probability of crossing diabatically increases as the slew rate of the field increases and as the energy gap decreases. The energy gap generally becomes smaller for increasing *n* and increasing M_J. For the case of experiments involving pulsed-field ionization of high-Rydberg states, $n > 100$, as in ZEKE spectroscopy (see section 5.1), the mechanism is generally diabatic, as first pointed out by Chupka [70]. This is because of the combination of high-*n* values and fast-rising pulsed fields that are used, together with the likelihood that M_J mixing has occurred to produce a population with predominantly high M_J character (see section 4). For the field ionization of lower-*n* Rydberg states, say $n \sim 50$, one might expect partially adiabatic/diabatic character, as shown for example by field ionization experiments on argon [86].

Finally, a practical point to note is that the fields required for ionization increase strongly with decreasing n as shown in table 2, and while field ionization may be a good method to detect excitation to Rydberg states below the adiabatic ionization threshold, it becomes progressively more challenging experimentally below $n = 10$. However, the strong variation with n (and k) of the threshold field for ionization allows 'selective field ionization' experiments in which a slowly rising pulse is used, and the time of ionization (and hence detection) varies with the quantum state that is populated.

3.6. *Theoretical approaches to the Stark effect in molecular Rydberg states*

The two main approaches that have been adopted are the diagonalization of an effective Hamiltonian in an appropriate zero-order basis set, and multichannel quantum defect theory (MQDT). In the former approach, first used for alkali-metal atomic systems by Zimmerman *et al.* [80] and subsequently applied to rare-gas atoms and small molecules [75, 82, 87–89], a basis set of wavefunctions is constructed which is considered to be a good representation of the zero-field wavefunctions, e.g., a Hund's case d set $|v^+, N^+, n, l, J, M_J\rangle$ and then the Hamiltonian matrix, using $H = H_0 + Fz$, is diagonalized. The matrix elements of Fz in the Hund's case d basis set have been given in references [30, 81, 82, 87, 88] and the radial parts of these matrix elements can be evaluated in the Coulomb approximation as shown in [75]. Zero-field couplings between states of different N^+ can be incorporated as for example in refs [1, 87] by relating the off-diagonal matrix elements of H_0 to the eigenchannel quantum defects. Transition intensities are related to the zero-field transition moments via the relationship

$$I_i(F) = \left| \sum_j c_{ij}(F) R_{j0} \right|^2 \tag{14}$$

where R_{j0} is the transition moment to the zero-field state j from initial state 0, and c_{ij} is the eigenvector for state i, i.e., $\Psi_i(F) = \sum_j c_{ij}(F)\Psi_j^0$. This equation represents the way that the initial transition intensity, which may be localized in just a few states, is spread out amongst many different eigenstates in the field.

In the case of autoionizing or dissociating states, the field causes not only a redistribution of the transition intensity but also of the coupling to the continuum (see section 4). This has the effect of redistributing the homogeneous linewidths. The linewidths of states in the field, $\Gamma_i(F)$, can be estimated as outlined in [75] using a similar means to the transition intensities

$$\frac{\Gamma_i(F)}{2\pi} = \left| \sum_j c_{ij} V_j \right|^2 \tag{15}$$

where V_j represents the strength of coupling to the dissociation/ionization continuum and is related to the zero-field linewidth of state j by the equation $\Gamma_j^0 = 2\pi|V_j|^2$. Strictly speaking this equation is only valid if each zero-field bound state is coupled to a different continuum channel. The alternative (and more rigorous) approach is to add an additional term to the Hamiltonian

$$H = H_0 + Fz - \mathrm{i}\Gamma/2 \tag{16}$$

as shown by Bixon and Jortner [88], in which the imaginary part represents the strength of coupling to the continuum. The diagonal elements of the rate matrix Γ_{jj} are the zero-field linewidths of the states j while the off-diagonal matrix elements of $i\Gamma$ represent higher-order interactions between two bound states and a common continuum. In the limit of these off-diagonal elements of Γ being set to zero, this approach becomes identical to the calculation given in equation (15). It should be noted that the sum of all linewidths must be conserved when the field is applied, as specified by the diagonal sum rule [90, 91].

$$\sum_j \Gamma_j^0 = \sum_i \Gamma_i(F). \tag{17}$$

The matrix diagonalization approach is moderately successful in the description of Stark spectra, particularly for bound states. The interpretation of the results in terms of the eigenfunctions being linear combinations of a Hund's case d basis set is straightforward, and this leads to an easy physical picture of the effects of the field. These can be discussed in terms of which states are mixed and how much high-l/low-l character a given state possesses, or how much admixture of different core states occurs. However, there are three main deficiencies. Firstly, in the treatment of interactions with the continuum, the imaginary off-diagonal matrix elements of the rate matrix Γ are rather difficult to determine or estimate. Secondly, there may be a requirement to use very large (and possibly complex) matrices to achieve convergence in the high-n region. Thirdly there is a difficulty in describing complicated spectroscopic lineshapes arising from interference between different excitation pathways to a continuum channel (as discussed by Fano and others) [75, 92–94] because the direct transition probability to the continuum is not explicitly included.

The MQDT approach [1, 95–97] to the Stark effect is well designed for describing interactions with the ionization continuum and generally requires the manipulation of smaller matrices, as a whole sequence of n values can be described as a single channel; effectively the principal quantum number is replaced in the theory by the energy as a continuous variable. Thus in regions where the Stark manifolds due to many n values overlap, the interactions between these manifolds are automatically included without extending the size of the matrices. The effect of the electric field is incorporated into MQDT by defining an external region (III in figure 10) where the potential experienced by the Rydberg electron is of the form (using atomic units)

$$V = -\frac{1}{r} + Fz \tag{18}$$

and therefore the wavefunction is a linear combination of hydrogenic Stark functions in parabolic coordinates (equation 9). An additional frame transformation is incorporated between this region and the pure-Coulombic region of field-free MQDT as described in [97]. The method has been applied to H_2 and N_2 [97] and NO [1] through developing the formalism described by Sakimoto and Harmin and has been compared with experimental spectra, and directly with the matrix diagonalization approach [1]. An additional advantage of the MQDT approach is that the quantum defects that form the basic input parameters not only characterize the bound state energies but also the bound–continuum interactions including those higher-order interactions that were described by the off-diagonal matrix elements of the rate matrix. Thus the number of input parameters required to calculate a spectrum is in principle smaller. The disadvantage of the MQDT method for the

Stark effect is that moderately large complex matrices still have to be inverted and manipulated at every energy point on a fine energy grid. Thus although these matrices may be smaller in dimension than for the matrix diagonalization approach the matrix operations have to be carried out many more times. Nevertheless this approach is certainly the most rigorous and potentially the most capable of providing a means to analyse the finest details of Stark spectra [1].

3.7. *Orientation of the ionic core in the presence of an electric field*

As illustrated in figure 13 the Stark states of the H atom have a strongly polarized electron distribution, and assuming that the Rydberg states of molecules show similar behaviour, it is interesting to ask whether this polarization has any effect on the rotational motion of the ion core. Consider an electron fixed at a distance from the ionic core corresponding to the radius of an $n=8$ Rydberg orbital as illustrated in figure 18. The field at the position of nucleus A is slightly different from the field at the position of nucleus B. If the charge distribution of the core is such that the net charge on A is slightly more negative than the net charge on B then the orientation shown will be energetically more favourable than the reverse orientation. If the charge distribution is characterized by a dipole of 1 au as in CO^+ [98] the energy difference would be $\sim 100\,\mathrm{cm}^{-1}$, which classically would lead to a probability distribution of the ion-core orientation that favoured the orientation shown in the figure.

Quantum mechanically the orientation arises from the admixture, in the presence of the field, of basis functions having odd and even rotational quantum states of the ion core, but with the same orbital angular momentum quantum numbers l, m_l. This effect is analogous to, for example, *sp* hybridization of electronic wavefunctions. This admixture can only occur by a second-order interaction, in which the core dipole induces a mixing of states with different N^+ and different l and then the external field mixes states of the same N^+ and different l, e.g.,

$$\left|N^+, M_{N^+}, l, m_l\right\rangle \overset{H_{\mathrm{dipole}}}{\leftrightarrow} \left|N^+ \pm 1, M_{N^+}, l \pm 1, m_l\right\rangle \overset{H_{\mathrm{Stark}}}{\leftrightarrow} \left|N^+ \pm 1, M_{N^+}, l, m_l\right\rangle. \qquad (19)$$

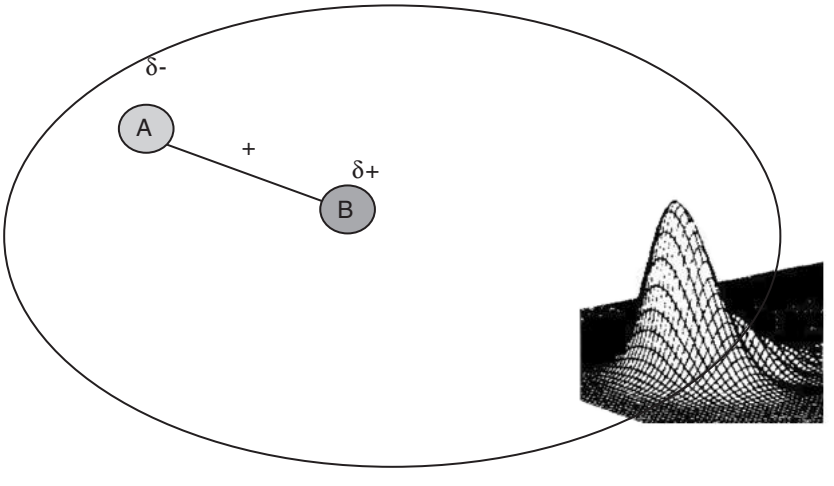

Figure 18. Classical picture of Rydberg core orientation for a molecule with a dipolar core.

In effect, states analogous to the pendular states produced in the 'brute-force' method [100] are created in the ion-core rotational wavefunction. The magnitude of the effect depends critically on the principal quantum number, the size of the internal dipole and the strength of the applied field. For CO we have calculated, using a matrix diagonalization approach, that an orientation characterized by $\langle \cos\theta \rangle = 0.4$–$0.5$ would be obtained for certain Stark states [99] for applied fields less than $10\,\mathrm{kV\,cm^{-1}}$, where $\cos\theta$ is the angle made by the core internuclear axis with the applied field.

Although this effect remains to be demonstrated experimentally, the interest is that this potentially provides a route for creating oriented molecular ions within the Rydberg orbit using relatively modest electric field strengths. 'Brute-force methods' applied for orienting neutral molecules [100] are not applicable to ionic species because of the large fields involved.

3.8. *Inhomogeneous field effects*

In a *homogeneous* field only the M_J quantum number, representing the projection of the total angular momentum, is conserved. If the field is *inhomogeneous* (i.e., varying in space), and the cylindrical symmetry of the field is lost, M_J is no longer a good quantum number. Merkt and Zare formulated the potential energy of interaction between the field due to a point charge $z_i e^2$ and a Rydberg state [101] in terms of a contribution to the Hamiltonian of the form

$$\begin{aligned} V_i &= -\frac{z_i e^2}{4\pi\epsilon_0 r_{ie}} \\ &= \sum_{k=1}^{\infty} \sum_{q=-k}^{+k} f_{kq}(R_i, \Phi_i, \Theta_i) \times r_e^k Y_{kq}(\theta_e)(\phi_e). \end{aligned} \tag{20}$$

In this equation r_{ie} is the distance from the charge to the Rydberg electron, R_i, Φ_i and Θ_i are the polar coordinates of the charge with respect to the centre of mass of the molecule and r_e, θ_e, ϕ_e are the electronic coordinates. The geometric factors f_{kq} are given by

$$f_{kq}(R_i, \Phi_i, \Theta_i) = \frac{(-1)^{q+1}}{\epsilon_0} \frac{z_i e^2}{R_i^{k+1}} \frac{1}{2k+1} Y_{k-q}(\Theta_i, \Phi_i). \tag{21}$$

The matrix elements of the parts depending on the electronic coordinates in equation (20) are given in a hydrogenic approximation in ref. [101], and the state-mixing effects can be calculated in a matrix diagonalization approach as described above for homogeneous fields but with inclusion of basis functions for all M_J values. This formalism was extended by Rednall and Softley [102] to incorporate the effects of *many* point charges, so that the effect of *any* field which can be represented by a set of point charges can be calculated in principle. A single point charge does not cause M_J mixing in itself because the field due to this charge remains cylindrically symmetric along the axis between the charge and the molecule. However, a combination of, for example, a point charge due to a nearby ion or electron and an applied homogeneous field in a different direction, or the combined effect of two nearby charged particles, does result in M_J mixing. As shown in reference [102] the field must vary significantly on the scale of the Rydberg-orbital dimensions for non-negligible M_J mixing to

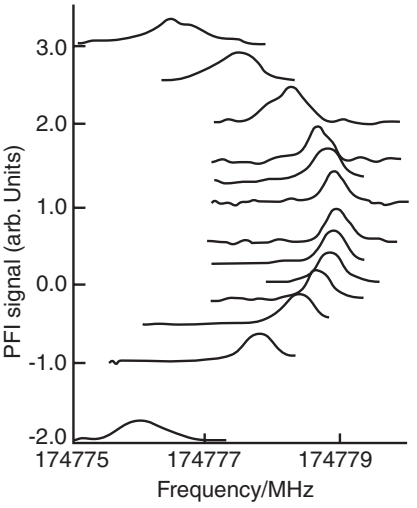

Figure 19. Millimetre-wave spectrum of the krypton $77d[3/2]_1$–$91f[5/2]_2$ transition for the range of applied fields -1.0 to $3.0\,\mathrm{mV\ cm^{-1}}$. The quadratic Stark shift shows a turning point at 1 $\mathrm{mV\ cm^{-1}}$ indicating there is a stray field of this magnitude (reprinted with permission from ref. [103], copyright (1999) by the American Physical Society).

occur. Such microscopic inhomogeneity can arise if charged particles come within ~ 50 Rydberg radii ($50n^2a_0$) of the Rydberg molecule.

As shown in figure 12 the levels of different k parabolic quantum number for the H atom have an m_l degeneracy in a homogeneous field which increases towards the centre of the Stark manifold. A similar effect is found for non-hydrogenic systems [102] and therefore the predominant M_J mixing occurs in an inhomogeneous field between the near-degenerate levels that underlie each Stark k-component. As shown in section 4, M_J mixing is believed to have a significant effect on Rydberg state lifetimes.

3.9. *Electric field determination*

Using the millimetre-wave excitation method described earlier, Merkt and coworkers have shown that high-resolution measurements of the Stark effect provide a means to characterize and compensate very small stray electric fields [103]. Figure 19 shows how the energy of the $77d[3/2]_1$–$91f\,[5/2]_2$ transition of the krypton atom varies quadratically with electric field strength over the range -1 to $3\,\mathrm{mV\,cm^{-1}}$. By adjusting the strength of compensating fields to move this resonance to the zero-field position these workers could reduce stray fields to below $20\,\mu\mathrm{V\,cm^{-1}}$.

4. Lifetimes of molecular Rydberg states

4.1. *Decay processes*

A key factor in determining whether Rydberg states can be of use beyond spectroscopic experiments is the survival time of these Rydberg states with respect to decay processes. For *atomic* Rydberg states below the ionization energy, the only mechanisms for decay are spontaneous emission, black-body radiation-induced stimulated emission or absorption, or collisional processes. The collision-free lifetimes of the $17p$ and $18p$ Rydberg states of Na have been measured to be 11.4 μs and

13.9 μs, respectively [67]. These should scale approximately as n^3 (see below) so that they are in the millisecond range for $n = 100$. Above the lowest ionization threshold, for Rydberg states built upon an electronically excited core, autoionization can also occur. For example, in the rare gases, the Rydberg series converging to the $^2P_{1/2}$ ionic level (the second threshold energetically) are degenerate above the adiabatic ionization energy with the free-electron continuum associated with the lowest-lying $^2P_{3/2}$ threshold. A coupling between the bound states and the continuum leads to autoionization:

$$A + h\nu \rightarrow A^*(^2P_{1/2}; nl) \rightarrow A^+(^2P_{3/2}) + e^-. \tag{22}$$

This process can be regarded as arising from an inelastic collision between the Rydberg electron and the ion core resulting in the electronically excited core giving up its energy to the Rydberg electron which is then ejected.

All the above processes are also possible in *molecular* Rydberg states. Autoionization may take on more guises, as the core can have several different types of energy which can be exchanged with the Rydberg electron. For example, for the energy levels illustrated in figure 2(*b*) the highest Rydberg states converging to the $N^+ = 2$ level are degenerate with the $N^+ = 1$ and 0 continua, such that a collision between the Rydberg electron and the ion core could lead to *rotational* autoionization. Vibrational autoionization can also occur for levels converging to vibrationally excited thresholds. In general rotational autoionization is likely to be the dominant process if energetics and symmetry allow it, and vibrational autoionization may in turn dominate over electronic autoionization.

In addition to these processes, in which the Rydberg electron effectively *receives* energy from the ion core, molecules may also undergo a transfer of energy from the Rydberg electron into the nuclear degrees of freedom of the molecule. In such a process, the Rydberg electron may revert to valence-like character and the end result is predissociation of the neutral molecule into electronically excited or ground-state *neutral* fragments

$$AB \rightarrow AB^* \rightarrow A + B^{(*)}. \tag{23}$$

In larger molecules the energy may be distributed amongst the various vibrational modes via intramolecular vibrational redistribution (IVR) processes and the lifetime with respect to dissociation could be very long [104]. Even so, the Rydberg character is lost once the Rydberg-electron–ion-core energy transfer takes place, and the Rydberg decay has therefore already occurred. Predissociation in simple molecules may be regarded as arising from the crossing of the Rydberg potential energy curve by a repulsive highly excited valence state (for example arising from two-electron excitation) as illustrated in figure 20.

In general, with the exception of some collisional processes (see section 6), the probability of these isolated molecule decay processes depends on the degree of penetration of the Rydberg electron into the ion-core region. The amplitude of the Rydberg electron wavefunction in the core region decreases with $n^{-3/2}$ and therefore lifetimes with respect to all decay processes, in the absence of perturbations between different Rydberg series, tend to increase with increasing n in proportion to n^3. This behaviour was shown for example for the predissociation lifetimes of the NO Rydberg series in the range $n = 40$–65 [105] (see figure 21) or for the Rydberg series in the range 10–45 for diazacyclooctane (DABCO) [106]. The lifetimes

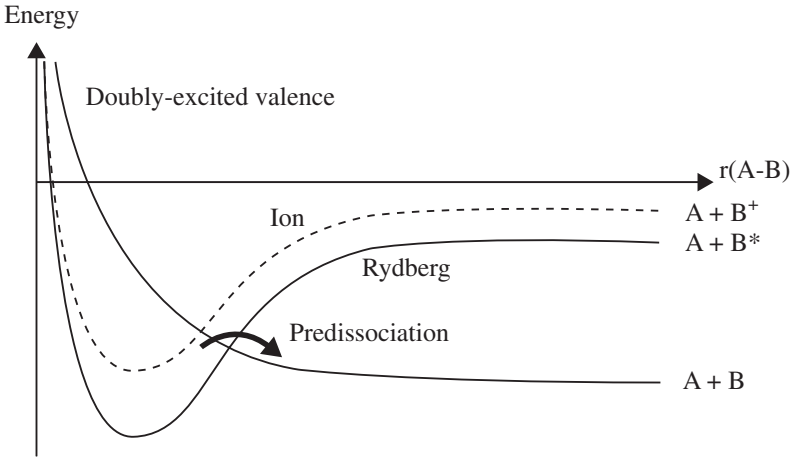

Figure 20. Schematic potential energy curves for Rydberg state predissociation.

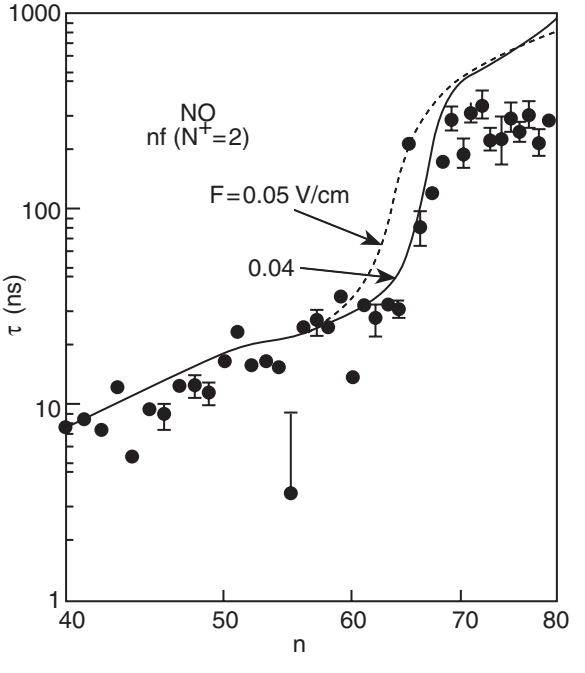

Figure 21. Experimentally determined lifetimes of NO Rydberg states ($N^+ = 2, l = 3$) plotted on a log–log scale (from ref. [105]).

generally increase with increasing l because of the progressively smaller quantum defects (and hence degree of penetration).

There are two main methods available for measuring Rydberg lifetimes. In the first method, the linewidths are measured and related to the lifetimes via the 'time–energy uncertainty' relationship $\Delta t \Delta E \sim \hbar/2$, more conveniently expressed as

$$\tau/\mathrm{s} = \frac{5.014 \times 10^{-12}}{\Gamma/\mathrm{cm}^{-1}},$$

as has been reported for HD [107]. Alternatively the Rydberg states are detected by pulsed-field ionization at a variable time delay between excitation and ionization. The number of Rydberg states surviving the time delay before ionization is monitored as a function of time delay to obtain a decay curve. For example Vrakking and Lee used this method for obtaining the data shown in figure 21 [105]. In a variation of this approach Mackenzie *et al.* observed autoionization lifetimes of high-n Rydberg states of N_2 by measuring the time of flight of the ions produced by decay. Ions autoionizing at different times in the presence of a small discrimination field received a different acceleration and therefore arrived at the detector at a different time [108].

Noordam *et al.* extracted information about the predissociation rate and the autoionization rate of Rydberg series in ammonia, by observing the competition between these processes and field ionization [109]. The observed ionization yield as a function of applied field was fitted to a rate model to determine $\Gamma \sim 1 \times 10^{15}/n^3$ for predissociation under field-free excitation conditions (a lifetime of 27 ps for $n = 30$). The autoionization rate was found to be approximately equal to the predissociation rate within experimental error.

4.2. *Electric field effects on lifetimes*

In the field of ZEKE spectroscopy (see section 5.1) there has been considerable interest in the understanding of Rydberg decay properties since it was recognized that the lifetimes of high-n Rydberg states detected by delayed field ionization in widely varying experimental setups were significantly longer than expected on the basis of n^3 scaling. For example, as shown in figure 21 for NO, there is an apparent jump in the measured lifetimes of the $N^+ = 2, nf$ states at around $n = 65$. In some cases a biexponential decay of the excited Rydberg population was observed, with a very long-lived component, superimposed on a short-lived component. For example, for N_2 excited to levels around $n = 165$ the fast-decaying component comprised 38% of the signal with a lifetime of $\sim 2\,\mu s$, while the slow-decaying component (62%) had a lifetime greater than $30\,\mu s$, as shown in figure 22.

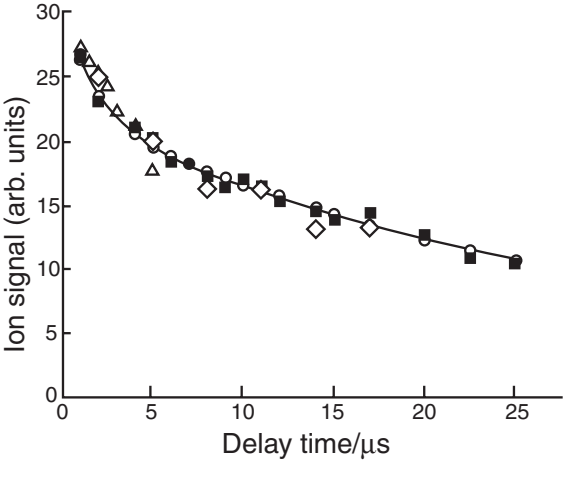

Figure 22. Decay of predissociating N_2 Rydberg states excited around $n = 165$ showing biexponential decay of the populated states (from ref. [108]).

Earlier measurements on atomic Rydberg states, e.g., in xenon [75], illustrated that electric fields would have a significant effect on lifetimes. The short-lived $nd[3/2]_1$ states in xenon become mixed with the long-lived high-l states and the nd lines become sharper as the field increases, while the high-l lines broaden. In simplistic terms the field-induced mixing of l character results in a democratic sharing of the strength of the coupling to the degenerate continuum, as can be explained by equation (15) and the sum rule (equation 17). Chupka pointed out [70] that the stray fields present in most experimental apparatuses were sufficient to cause such l-mixing for the high-n Rydberg states used in ZEKE spectroscopy; for $n = 160$ the Inglis–Teller field, which is usually taken as a measure of the field at which the l mixing is substantial, is just $17\,\mathrm{mV\,cm^{-1}}$. The democratic sharing of coupling to the continuum would lead to an apparent n^4 scaling of the lifetimes of the optically populated states (or an n^{-4} scaling of the homogeneous linewidths). If the sum of the zero-field linewidths of all states of given n and m_l scales with n^{-3},

$$\Gamma_{\mathrm{tot}} = \sum_l \frac{\Gamma_l^0}{n^3}, \tag{24}$$

where Γ_l^0 is a constant, then the average lifetime per quantum state in the field is

$$\Gamma_{\mathrm{ave}} = \frac{\Gamma_{\mathrm{tot}}}{n} = \frac{\sum_l \Gamma_l^0}{n^4}. \tag{25}$$

The above arguments assume that states with l greater than a certain value, e.g., $l \geq 5$, make a negligible contribution to the total linewidth.

Many calculations have been performed, using both matrix diagonalization, e.g., [88, 89] and MQDT [97] approaches, to investigate this effect and in general the population of the full set of Stark states of given n is expected to have a *distribution* of lifetimes. Bixon and Jortner predicted a *bifurcation* of the distribution [110] due to incomplete mixing in certain intermediate ranges of field, while Levine, Remacle and coworkers have attributed the biexponential behaviour of the decay [89, 111] to the coupling 'bottlenecks' introduced by the mixing of different rotational channels, in the situation where the density of bound states exceeds the density of continuum channels.

However, the observed lifetimes, and in particular the proportion of molecules with long lifetimes, are in general found to be even greater than could be predicted by l mixing only. A further factor of importance identified by Chupka [70] is the likely role of ions, which are created in the excitation volume, in causing additional electric-field effects. These ions create a local *inhomogeneous* field which can cause m_l mixing as well as l mixing (see section 3.8). In the limit of complete l and m_l mixing the arguments cited above can be extended to predict that the average lifetimes should scale with n^{-5} as there would be n^2 different l, m_l combinations for a given n amongst which to distribute the total linewidth:

$$\Gamma_{\mathrm{ave}} = \frac{\Gamma_{\mathrm{tot}}}{n^2} = \frac{\sum_{lm} \Gamma_{lm}^0}{n^5}. \tag{26}$$

Experimental measurements by Vrakking *et al.* [112] and Palm *et al.* [113] demonstrated the effect of varying the ion concentration explicitly. Calculations performed by Softley and Rednall [102] (also summarized in ref. [114]) suggested that complete m_l mixing could be achieved by the combined presence of a single ion at a distance of $\sim 5n^2 a_0$ (5 Rydberg radii) and an external field of order of the Inglis–

Teller field. However, when simulating the effect of a random distribution of many ions, it was found that the maximum stabilization – calculated to be an extra factor of $0.15n$ in the lifetime due to the effect of the ions – was likely to be achieved when the average separation of the ions from the Rydberg state was of order $20n^2a_0$. For higher densities it was likely that one ion would be sufficiently close to cause field ionization or electron exchange (see section 6.2). Although a small homogeneous component of the field was also necessary, it should not be so great as to dominate the inhomogeneous component; a homogeneous field significantly larger than the Inglis–Teller field weakened the amount of m_l mixing.

Overall the conclusions arising from these investigations were that if, as in many ZEKE spectroscopy experiments, one just needs to populate high-n Rydberg states of some approximate principal quantum number that can be subsequently field ionized in a well-defined manner without any need to control the exact quantum states populated, then ions and stray fields are of some assistance in providing the necessary stabilization. The success of ZEKE spectroscopy in a wide range of laboratories and for a wide range of molecules suggests that the requirements for these fields are not too specific. On the other hand, if one wants to carry out spectroscopic studies on Rydberg states for $n > 100$, or to obtain the optimum resolution from ZEKE spectroscopy using 'slicing techniques' (see below), or to investigate Rydberg state lifetimes under well-defined conditions, one would have to be very careful to control, and in some cases minimize, stray fields and ion densities.

4.3. *Time-dependent fields*

Although much of the literature has been concerned with lifetimes of states with $n > 100$, some recent experiments at lower n in our laboratory [115] have revealed some novel behaviour at rather lower values of n. As described in more detail in section 9, Rydberg states of H_2 around $n = 17$ were populated in selected Stark states and exposed to the inhomogeneous field of a dipole (constructed from a pair of cylindrical rods) for 2 μs. The field was then switched off and the Rydberg-state molecules were allowed to fly along a time-of-flight tube to the detector where they were field ionized. In this way the Rydberg states were apparently found to survive for more than 100 μs, well in excess of the expected radiative lifetimes.

This observation is linked to reports by Schlag and coworkers [116–118] that time-dependent fields could be used to 'lock' a population of high-n Rydberg states into long-lived high-m, high-l states. When a Rydberg population is excited in the presence of a field, the states have mixed low-l, high-l character. However, if the field is then ramped down to zero, the Stark states are expected to follow the Stark map adiabatically and ultimately most of these states will correlate with states of pure high-l character. Thus the effect of the downward field ramp is to trap the Rydberg electron in a high-l circular orbit in which the decay lifetime is long. Calculations by Procter *et al*. were performed [114] to investigate the detailed evolution of optically excited Rydberg wavepackets under the influence of time-dependent fields. The locking process is likely to be enhanced if the population evolves into high-m states before the field is switched off; this could be achieved by either rapidly rotating the field direction [116] or through the presence of inhomogeneous fields due to ions [114]. The high-m_l Stark manifolds have no low-l character (because $l \geq |m_l|$) and once the applied field becomes zero, the low-l states become separated energetically from the high-l states and there is no possibility of mixing the low-l character back into the wavepacket. Too high an ion density would have an adverse effect on

stabilization, however, because it would prevent the resultant field experienced by the Rydberg states from reaching zero. The motion of ions was also found to be important [114] in that movement away from the Rydberg state allowed the field to approach zero and removed the possibility of m_l mixing that would restore low-l character to the wavepacket.

In the case of the H_2 $n = 17$ Rydberg states, although the switching off of the field is likely to stabilize the populated states, this cannot be the whole story because the combined spontaneous emission and black-body radiation-induced decay lifetime is still expected to be shorter than 100 μs even for the high-l states. We return to this point in section 9.

Gallagher and coworkers have studied an alternative approach [119] to stabilization which involves applying microwave fields to drive transitions between levels of adjacent Stark manifolds (i.e., mixing of n with $n \pm 1$). After multiple transitions, both up and down in energy, the net effect is to disperse the population amongst the entire manifold including long-lived dark states. Stolow and Ivanov proposed the sequential use of pulsed electric and magnetic fields to coherently drive a Rydberg wavepacket into first high-l, and then high-m_l states and trap the population there [120]; this scheme has not been demonstrated experimentally, however. Park *et al.* reported that l and m mixing in Rydberg states in the range $n = 100$–200 could be induced using the AC electric jitter inherent in high-voltage switching [121].

5. Pulsed-field ionization spectroscopy

The pulsed-field ionization of Rydberg states lies at the heart of a number of the applications discussed in this article, including ZEKE and MATI spectroscopy, the state selection of ions, and the state-selective Rydberg tagging of chemical reaction products. ZEKE spectroscopy is the most well-established of these techniques [122, 123], and to some extent other developments have evolved from this.

5.1. *ZEKE spectroscopy*

The principal aim of ZEKE spectroscopy is to obtain high-resolution spectroscopic data for molecular cations by studying the pulsed-field ionization of the corresponding neutral molecule. The information obtained is akin to that obtained from photoelectron spectroscopy, and indeed the technique has its origins in threshold photoelectron spectroscopy [124], but the energy resolution achievable is considerably better. As shown in figure 2 and discussed earlier (section 1.3), the Rydberg energy levels of a molecule form series that converge at high-n to the various vibration–rotation levels of the cationic core. If an absorption spectrum were recorded, many overlapping series would most likely be observed. However, in ZEKE spectroscopy, pulsed-field ionization is used as the detection method, and for a small applied field only a narrow band of Rydberg states lying below each threshold would be observed. For example, for an applied field of $1.12\,\mathrm{V\,cm^{-1}}$, only Rydberg states with $n > 150$ would be detected (assuming the diabatic ionization mechanism, section 3.2) and all these would lie within $5\,\mathrm{cm^{-1}}$ of a given threshold. For a typical pulsed laser resolution of $0.1\,\mathrm{cm^{-1}}$, these high-Rydberg states in the range $n = 150 \rightarrow \infty$ would not be resolved and this region could be regarded as a *pseudo-continuum*. Thus if the laser wavelength is scanned through the Rydberg series converging to the various thresholds, while detecting electrons produced by pulsed-field ionization, a peak (comprising the band of unresolved field-ionized

Rydberg states) will be observed just below each threshold. In a sense this is equivalent to a threshold photoelectron spectrum [124], except that in the latter case a peak is observed just *above* each threshold, rather than just below it, through the detection of near-zero-kinetic-energy electrons. Experimentally in ZEKE spectroscopy the ionizing field is delayed with respect to the excitation laser pulse by hundreds of nanoseconds or even microseconds, so that only long-lived Rydberg states will be detected, and the time delay allows background electrons formed by direct ionization or fast autoionization to disperse so that only the PFI electrons are accelerated to the detector.

In principle, by making the pulsed field smaller, a narrower band of Rydberg states is detected and hence a narrower peak is observed below each threshold (and the centre of that peak is closer to the threshold). However, this approach is limited in practice because stray fields and collisional ionization tend to remove the population of the very highest Rydberg states (e.g., $n > 250$). Moreover, the diabatic ionization mechanism has an effect on the resolution because of the different pulsed-field ionization (PFI) behaviour of the red-shifted or blue-shifted Stark states. As illustrated in figure 14, the field-ionization probability for the total Stark state population increases gradually rather than abruptly on the low-frequency side of a given threshold in the approximate range $I - 3.1\sqrt{F}$ to $I - 4.6\sqrt{F}$, giving a broad tail to any PFI peak.

The best resolution in ZEKE spectroscopy $\sim 0.06\,\mathrm{cm}^{-1}$ has been achieved by Merkt and coworkers [71] using a variation of the 'slicing method' first proposed by Müller-Dethlefs and coworkers [125, 126]. In the original slicing method, which demonstrated a resolution of around $0.15\,\mathrm{cm}^{-1}$, a two-pulse sequence was used as shown in figure 23(*a*). The first pulse, magnitude F_1, removes all the population down to $\sim 3.1\sqrt{F_1}\,\mathrm{cm}^{-1}$ below threshold and removes primarily the red-shifted Stark states in the range $\sim 3.1\sqrt{F_1}$ to $4.6\sqrt{F_1}$ leaving a remnant population of blue-shifted Stark states in this range. When the field is reversed by the second pulse the blue-shifted Stark states become converted into red-shifted states that are less resistant with respect to ionization by the second field. By making this field F_2 slightly smaller than F_1, the 'slice' of Rydberg states detected can be made narrow and is roughly in the range $3.1\sqrt{F_1}$ to $4.6\sqrt{F_2}$. This range can be made arbitrarily narrow, but at the expense of signal to noise. Merkt and coworkers improved the resolution using the pulse sequence shown in figure 23(*b*), with the ZEKE signal detected arising from one of the small negative steps shown. The key features of the pulse sequence were deemed to be [71]: (a) the polarity of the field must be rapidly switched with no time delay between the positive- and negative-going pulses; (b) the absolute value of the field in the negative steps should be in the range 40–70% of the positive pulse; (c) the magnitude of the steps should be kept as small as is compatible with a measurable signal.

This resolution is several orders of magnitude better than that obtainable using conventional photoelectron techniques ($\sim 100\,\mathrm{cm}^{-1}$) or time-of-flight techniques [127] ($\sim 10\,\mathrm{cm}^{-1}$), and, as demonstrated for the first time by Müller-Dethlefs *et al.* in 1984 [122, 123], leads to the possibility of rotationally resolved photoelectron spectra at least for small molecules. In the last 20 years the technique has been applied to well over 100 molecules and several reviews are available [128–132]. Examples of molecules for which rotational resolution is obtained range from stable diatomics such as N_2 [133], H_2 [134], O_2 [135], HBr [136], to small polyatomics, e.g., NH_3 [137], CH_2CO [138] or C_6H_6 [139, 140]. Vibrationally resolved spectra of larger

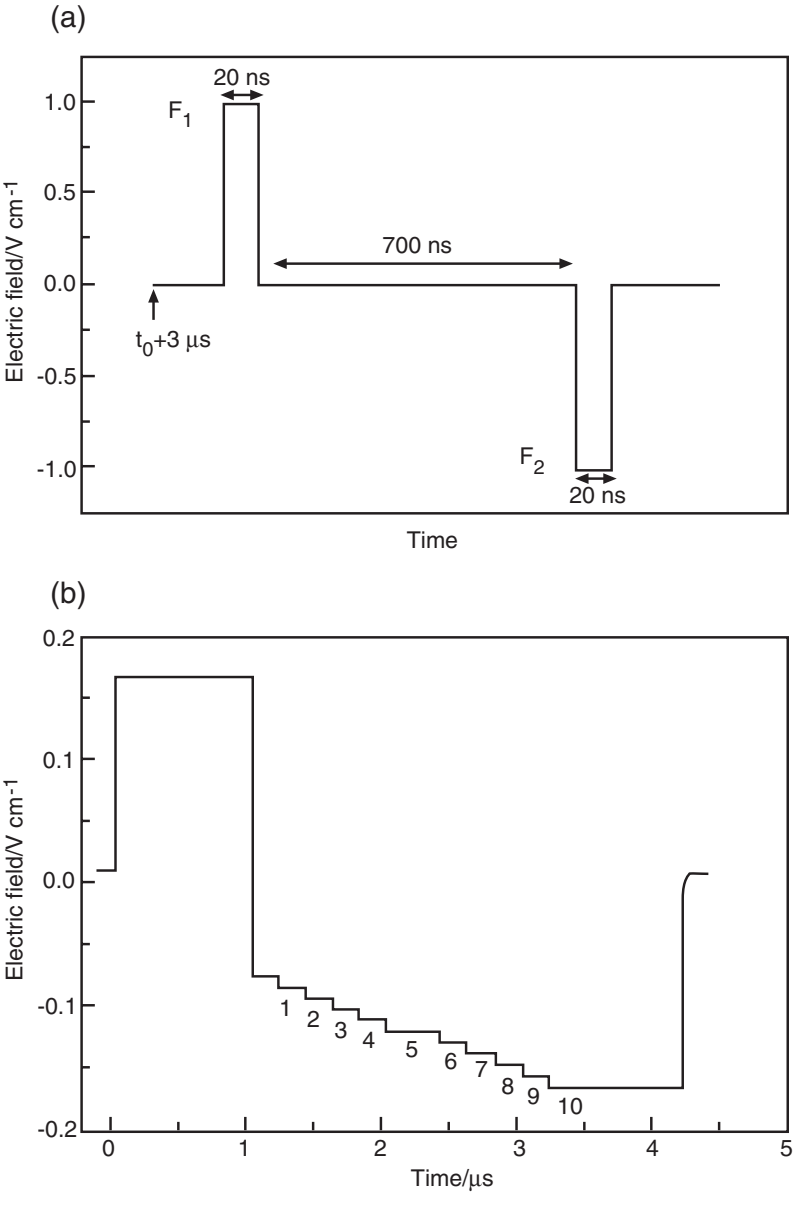

Figure 23. Pulsed field sequences used for optimum resolution via the 'slicing' technique in ZEKE spectroscopy: (*a*) sequence used by Müller-Dethlefs and coworkers [125, 126], and (*b*) by Merkt and coworkers [71].

organic molecules and clusters have been obtained [131], a recent example being H_2O-acetanilide [141]. These results have been used to gain insight into the changes in weak intermolecular bonds on changing from the neutral to the cation, in conjunction with *ab initio* calculations of vibrational frequencies [128]. ZEKE spectra of metallic atom clusters or metal-containing species such as V_3 or $YO(CH_3)_2$ have also been obtained [142], and two groups have used ZEKE spectroscopy for negative ion studies [143, 144] to obtain information on the

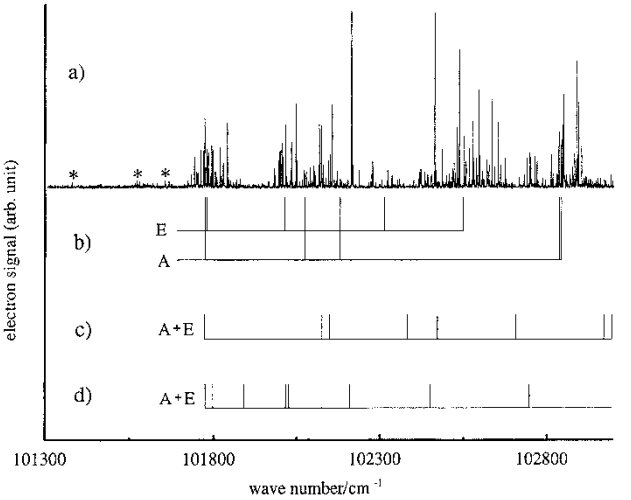

Figure 24. (*a*) Rotationally resolved ZEKE spetrum of CH_4; (*b*)–(*d*) simulated vibrational transitions using different one-dimensional models for the pseudo-rotation in the cation (from ref. [149]).

corresponding neutral radical species. Neumark and coworkers have also used anion ZEKE as a means for transition-state spectroscopy in IHI^- [145], but it should be noted that negative ions do not have Rydberg states and therefore ZEKE spectroscopy of negative ions is a true threshold photolectron technique. Recently effective methods have been developed for multiphoton-ZEKE [146] and VUV-ZEKE spectroscopy [147] of free radicals such as CH_2 and NH_2, formed by photolysis or pyrolysis in a supersonic expansion.

A classic example where ZEKE spectroscopy has brought completely new spectroscopic information is the case of CH_4 [148, 149]. Direct spectroscopy on the CH_4^+ cation has not been possible in the past and conventional photoelectron spectra of CH_4 did not have sufficient resolution to gain structural information. Merkt and coworkers have obtained the rotationally resolved ZEKE spectrum of several isotopomers of CH_4 (see figure 24). The CH_4^+ molecular ion is the 'simplest' example of a molecule showing the Jahn–Teller effect in it ground state. In all the isomers except for $CH_2D_2^+$ the molecule undergoes large-amplitude pseudo-rotational tunnelling motion between numerous equivalent minima (six in CH_4/CD_4 and three in CH_3D) on a picosecond timescale. The tunnelling splitting is of the same order as the rotational constants and therefore highly complex (and only partly assigned) spectra have been obtained. For $C_2D_2^+$ the molecule behaves as a rigid rotor and the static Jahn–Teller distortion can be determined. The study of the $C_6H_6^+$ cation by Müller-Dethlefs *et al.* is another example where important information about dynamic Jahn–Teller distortions has been obtained [139] from ZEKE spectroscopy.

ZEKE spectroscopy can be performed using either single-photon VUV/XUV excitation from the ground state, as in the case of CH_4 above, or using resonance-enhanced multiphoton excitation. In the former case, the spectra will be composed of transitions from several populated ground state levels, and if rotational resolution is achieved then rotational branch structure will be observed akin to conventional electronic spectroscopy (e.g., [133]). Although most experimental setups have used

laser-based sources for single-photon studies, Merkt and Guyon made one of the first demonstrations of combining the synchrotron source with the ZEKE technique [150] and this has been developed by Weitzel [151] and by Ng *et al.* [132]. These latter authors, using the third-generation advanced light source (ALS), have achieved a resolution of near $1\,cm^{-1}$, comparable with many laser studies and having the advantage of very broad tunability. The ZEKE spectra of approximately 20 small molecules have now been studied in the energy range 9–26 eV at the ALS as reviewed by Ng [132]. An example is their study of O_2 for which the vibrational levels of O_2^+ were rotationally resolved for the states $X^2\Pi_g, v = 0-38; a^4\Pi, v^+ = 0-18; b^4\Sigma_g^-$, $v^+ = 0-9; B^2\Sigma_g^-, v^+ = 0-7$ and $c^4\Sigma_u^-, v^+ = 0-1$. This example demonstrates the tunability advantage of synchrotron sources, although complete ZEKE studies of all the vibrational levels of certain rare-gas dimers have also been carried out using a laser VUV source at higher resolution albeit with lesser ease of tuning [152].

For multiphoton excitation, most studies have made use of the $1 + 1'$ excitation especially for molecules with an aromatic chromophore (e.g., benzene via the S_1 state [139]). Some $2 + 1'$ (e.g., NH_3 [137])) and even $3 + 1'$ studies (e.g., H_2 via the B state [153]) have been performed but the difficulties in obtaining a good balance of laser powers should not be underestimated in these cases, and the use of focused lasers means that the excitation conditions may not be 'clean'. In the resonance-enhanced multiphoton process, a single rotational level of the intermediate may be selected, in which case the rotational branch structure is eliminated and the ZEKE spectra become relatively simple.

ZEKE spectroscopy has also been used as a time-dependent probe of intramolecular dynamics [154], a recent example being the study of vibrational redistribution in the S_1 state of 9-ethylfluorene [155]. Using picosecond lasers Knee and coworkers found that by varying the time delay between the pump laser excitation of a molecule into the S_1 intermediate state and the probe laser exciting to the high-n Rydberg states, the ZEKE spectrum also changes. These changes are caused by evolution of the electronic or vibrational character of the intermediate which favours different transitions to the cationic states. A lifetime of 120 ps was found in the case of 9-ethylfluorene for the decay of the intermediate at an energy $990\,cm^{-1}$ above the band origin.

Very high-precision ionization potentials should be obtainable from ZEKE spectroscopy because of the high resolution and clarification of rotational structure. However, there is often a question about how best to extrapolate the observed peak positions to determine the actual threshold; these positions are always red-shifted with respect to a given threshold, and various empirical approaches have been adopted, plotting peak positions as a function of ionizing field [156]. The diabatic field-ionization model is based on calculated ionization rates for the hydrogen atom, and whereas the range $3.1\sqrt{F}$ to $4.6\sqrt{F}$ is a useful guide to the tail-off of the diabatic ionization it is not necessarily applicable with precision to molecular Rydberg states.

In fact the optimum precision in determining an ionization potential is obtained if the very high Rydberg states within the ZEKE peaks are actually resolved using a high-resolution laser, as demonstrated by Seiler *et al.* [157]. By observing Rydberg states up to $n = 200$ within the pulsed-field ionization range, the series can be extrapolated to give the threshold (e.g., for N_2) using the standard Rydberg formula to a precision of $0.015\,cm^{-1}$. In the case of NH_3 the interference between two series converging on the spin–rotation components of the $v_2^+ = 1, 1_0(A_2)$ level was used to

determine the spin–rotation spacing of that level of the ion, which is just $0.059\,cm^{-1}$ [28]. Neusser *et al*. obtained a similar precision in extrapolating high-Rydberg series of benzene in the range 48–110; 64 series of C_6D_6 and 20 series of C_6H_6 were analysed, each converging to a different vibration–rotation level of the cation [14] (see also reference [158] for a study of lifetime issues affecting these measurements). Watkins and Cockett made a direct comparison between Rydberg extrapolation and ZEKE spectroscopy in DABCO and concluded that the values of the ionization potential from the Rydberg spectroscopy had a greater precision [156]. In cases where only partial rotational resolution in a ZEKE spectrum is obtained it may still be possible to fit the rotational contours of the vibrational band profiles to determine accurate ionization thresholds and rotational constants as shown by Müller-Dethlefs *et al*. [159].

5.2. *MATI and PIRI spectroscopy*

In 1994 Zhu and Johnson [160] demonstrated that an equivalent spectrum to a ZEKE spectrum could be obtained by detecting the *ions* formed by pulsed-field ionization rather than the electrons. The advantage of this approach was that the time of flight of the ions could be measured and related to their mass, and therefore a species-selective spectrum could be obtained – hence the name 'mass-analysed threshold ionization' (MATI). Thus, the method is potentially useful in any situation where many species may be present, such as mixtures of isotopomers, clusters of variable size, or radical species formed in a discharge expansion. The disadvantage of this approach is that whereas background electrons are very rapidly dispersed in the ZEKE experiment by very small stray fields or by applied discrimination fields or under their own velocity, the ions move more slowly and remain in the excitation region for much longer. Typically a small discrimination field is therefore applied after excitation to push background ions out of the ionization volume and then, after a delay of order several microseconds, a second field is applied to field-ionize the surviving Rydberg states. MATI spectra have generally been of lower resolution than ZEKE spectra, although it was demonstrated [126] that a variation of the double-pulse slicing technique could be used to obtain comparable resolution to ZEKE spectra. Johnson and coworkers have recently combined MATI spectroscopy with a VUV excitation source and carried out studies of cationic vibrational structure in molecules such as 1,4-dioxane [161]. Examples of molecules studied using MATI (and multiphoton excitation) in our laboratory (see also [162]) include H_2O [163] and NH_3 [58, 59], the radical CD_3 [164], formed by photodissociation of CD_3I, and ArNO [165]. In this last case, it was possible to identify certain previously unassigned vibrational bands in the A–X (1+1) resonance-enhanced multiphoton ionization (REMPI) spectrum on the basis of the MATI spectrum out of the A state intermediate levels. These spectra confirmed that the bands originated from vibrationally excited levels of the ground state, and thus the MATI spectra provided a novel means for gaining information about the vib–rotational structure of the ground state of the neutral complex. Neusser and coworkers have shown [166] that the threshold for dissociation of the cation can be determined using MATI spectroscopy through the appearance of a daughter ion, e.g., the appearance of benzene cations in the MATI spectroscopy of benzene-Ar_n. The onset of dissociation provides a means to determine the dissociation energy of the ionic cluster. The experiments described below involving state-selection of ions (see section 7) are an extension of the MATI experimental technique.

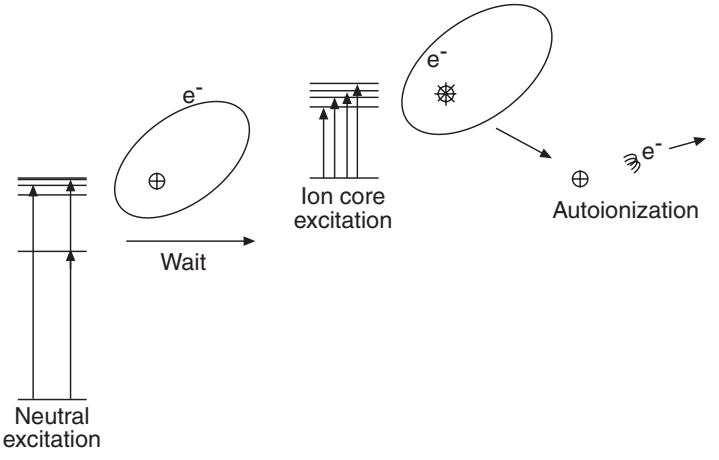

Figure 25. Excitation scheme for the PIRI technique.

Subsequently Johnson and coworkers demonstrated a further new technique, know as photoinduced Rydberg ionization (PIRI) [167] in which benzene was excited using two lasers to Rydberg states converging on the lowest ionization limit and then a third laser was introduced electronically to excite the ion core, as illustrated in figure 25. It was found that the core excitation led to autoionization of these states and the detection of an ion signal. This provided a method for observing electronic transitions of the ion core, and it has been subsequently applied to the B–X transitions in the phenol [168] and fluorobenzene [169] cations. An infrared version of this technique was subsequently developed by Fujii and coworkers [170, 171] in which vibrational excitation of the core was induced using an infrared laser leading to vibrational autoionization, and they observed systematic measurements of the OH and CH vibrations in various phenol-derivative cations. Some unconventional hydrogen bonds were discovered between hydroxyl and alkyl groups through measurement of the vibrational frequencies. A variation of this technique was developed by Kleinermanns and coworkers in which the infrared pumping of the ion-core vibrational levels was detected as a depletion in the normal MATI signal to obtain frequencies of OH-stretching vibrations in aromatic cations [172].

There remain some questions about the mechanism by which the PIRI technique works, particularly why the excitation of the ion core causes significant changes in the lifetimes of the stabilized high-n Rydberg states. It must be assumed that these states are strongly l and m_l mixed in order to survive the typical 3 μs delay before core excitation, and therefore it is not well established why this stabilization is affected by the core excitation. Johnson reported [173] that the technique worked best when populating states in the range $n = 50$–70 for benzene, suggesting that a compromise between stabilization of the initial Rydberg state and the capability for subsequent autoionization was required. Nevertheless the technique is particularly useful in providing a means for studying the spectroscopy of state-selected cations. It offers a sensitivity that techniques for direct spectroscopy on cations cannot offer because of the effective means of detection against a zero background.

5.3. *Intensities in ZEKE and MATI spectroscopy*

The intensities of transitions in ZEKE and MATI spectra have been the subject of considerable interest. To a first approximation, the excitation to the pseudo-continuum of Rydberg states can be regarded as equivalent to excitation to the true continuum above threshold and therefore the intensities would be expected to be governed by photoionization selection rules and propensity rules. Thus Franck–Condon factors should be a good guide to relative intensities of vibrational bands. The rotational selection rules must take into account the angular momentum that is carried away by the photoelectron, which implies that the conservation of angular momentum is described by

$$\mathbf{J}_0 + \boldsymbol{\gamma} = \mathbf{J}^+ + \mathbf{j}_{\mathrm{Ryd}} \tag{27}$$

where the vectors given are the initial angular momentum $\mathbf{J}_0$, the photon angular momentum $\boldsymbol{\gamma}$, the ionic angular momentum $\mathbf{J}^+$, and the free-electron (or Rydberg electron) angular momentum, $\mathbf{j}_{\mathrm{Ryd}}$. The angular momentum theory for rotational selection rules in diatomic molecules was first derived by Buckingham *et al.* [174] and reformulated by Xie and Zare [175] who also discussed the selection rules for diatomic molecules in detail [176]. The propensities for given rotational changes depend principally on the angular momentum characteristics of the orbital from which the electron is removed; using the rotation spectator model [177] and assuming that the total electron spin is conserved in the transition it can be shown that rotational changes are restricted by the requirement that

$$\mathbf{N}^+ = \mathbf{N}' + \mathbf{l}' \tag{28}$$

where $\mathbf{l}'$ is the orbital angular momentum of the electron that is removed and $\mathbf{N}'$, $\mathbf{N}^+$ are the initial and final rotational angular momenta excluding spin [59]. However, as discussed in detail in the review of Merkt and Softley [177], the interpretation of these rotational intensities, in almost every case where rotational structure is observed, is complicated by the existence of 'channel interactions'. As illustrated in figure 26, the pseudo-continuum of Rydberg states converging to one rotational threshold may be perturbed by the existence of degenerate interloper states belonging to series converging on higher limits. There may also be degenerate continua which are weakly coupled to the pseudo-continuum. The couplings between these different series manifest themselves as intensity perturbations in ZEKE spectroscopy. Individual rotational transitions may either borrow intensity from transitions to the interloper states, or there may be a depletion of intensity known as a window resonance [178] if the interlopers have no intrinsic transition probability. These effects may not only perturb rotational line intensities but also affect the intensity of different vibrational bands, an extreme example of which is given by the observation of vibrational bands in the ZEKE spectrum of Ag_2 [179] which show very different relative intensities compared to the predictions based on Franck–Condon factors. In several cases these interloper states have been partly resolved within the pseudo-continuum belonging to a particular ZEKE peak (e.g., [28, 59, 133, 134]). This effect is illustrated for the MATI spectrum of ammonia in figure 26. Seiler *et al.* have used a very high-resolution laser to scan across ZEKE peaks in Ar, N_2 and NH_3 and in some cases have clearly resolved not only the interloper states but also the interacting levels of the pseudo-continuum [28, 157].

McKoy and coworkers have developed an *ab initio* approach to calculating the ZEKE spectra of diatomics and small polyatomic hydrides [180, 181, 182]. Generally

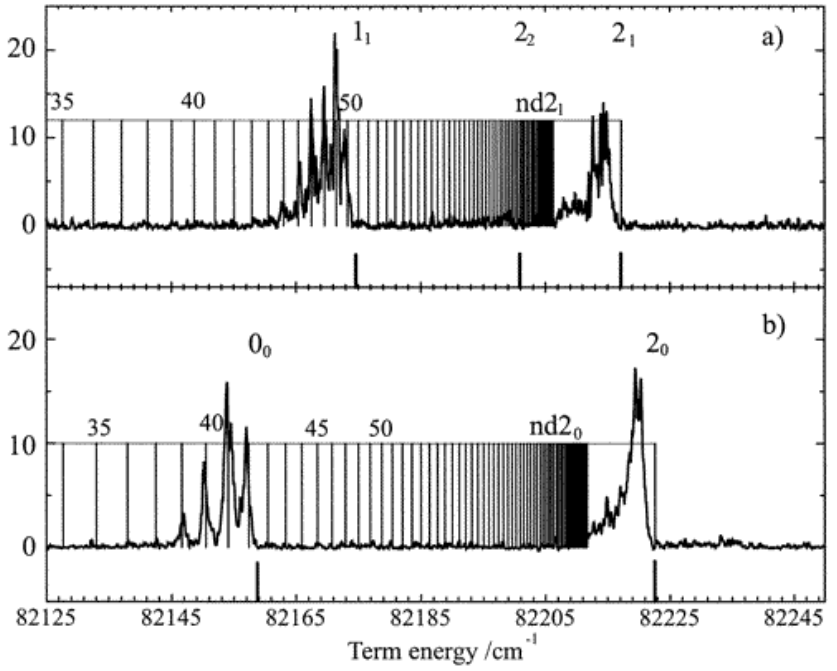

Figure 26. MATI spectrum of NH_3 (reprinted with permission from ref. [59], copyright (2001) American Chemical Society) showing how interloper Rydberg states converging to the 2_1 limit (*a*) or the 2_0 limit (*b*) appear as peaks in the MATI features at the lower-lying 1_1 and 0_0 thresholds (using the notation $N^+_{K^+}$).

applicable propensity rules for the photoionization process in symmetric tops and asymmetric tops can be extracted from their model. No assumptions are made about the angular momentum character of the orbital from which the electron is removed as this is determined in the *ab initio* calculations. Although a good match to experimental results has been obtained in many cases, small but significant deviations remain because these calculations do not include the interactions referred to above between the bound Rydberg series and the field-ionized pseudo-continuum. Continuum–continuum couplings *are* included, however, and these are closely related to the bound-state interactions. A related model using symmetry arguments to predict allowed transitions and intensities has been proposed by Müller-Dethlefs and applied to the ZEKE spectrum of ammonia [183]. The model incorporates some aspects of the MQDT frame transformations but again does not include the effects of bound-state channel interactions.

Signorell and Merkt [184] derived a general set of symmetry selection rules applicable to the photoionization and Rydberg excitation of polyatomic molecules using the molecular symmetry group. These rules are based solely on group theoretical considerations and assume conservation of the total angular momentum only, and the formalism provides a means to correctly determine a complete listing of all ionic vibration–rotational states accessible from a given initial level. Thus, these rules provide an extremely useful all-embracing general framework, although they do not make any distinction between photoionization channels that are accessed through direct transition intensity as opposed to indirect access via channel

couplings, and so do not necessarily provide detailed insight into the intensity mechanisms at work in a ZEKE or MATI spectrum.

In our work we have developed the first applications of MQDT to the simulation of ZEKE line intensities, including interactions between the pseudo-continuum and interloper bound states, for the molecules H_2 [48] and NH_3 [58, 59]. The MQDT approach incorporates all channel interactions but requires only quantum defects and dipole transition moments as input parameters. The advantage of this approach is that bound states and continua are treated in a single formalism, allowing the possibility of developing a 'complete' theory of ZEKE/MATI intensities. To simulate a MATI or ZEKE spectrum the excitation probability to the long-lived Rydberg states that are subsequently field-ionized must be calculated. The quantity required is a *partial* cross-section in the sense that there are normally degenerate continua associated with lower-lying ionization thresholds that can also be excited either directly or indirectly at the same time. These continua give rise to prompt electrons/ions upon excitation, which are not detected in the ZEKE/MATI experiments. Although the pseudo-continua of high-n Rydberg states are *closed* channels with respect to ionization, in practice it is only possible to calculate the partial photoionization cross-section into an *open* channel. The procedure adopted is therefore to artificially lower the threshold of interest by an amount equal to the lowering by the pulsed ionization field, and to treat the pseudo-continuum as a true continuum for the purposes of calculating the intensity. This approach proved to be extremely successful in predicting the relative intensities of lines in the ZEKE spectrum of H_2 [48] including some very strong perturbations due to channel interactions with bound states. In the case of ammonia [59] the quantum defect parameters were less well-determined, and were adjusted to give a good fit between experiment and theory. The adjustable parameters included a mixing angle which characterized the p-d mixing occurring in the core region as a result of configuration interaction. The molecular symmetry rules derived by Signorell and Merkt were used in the construction of the quantum defect matrix. Figure 27 shows the level of agreement achieved between these calculations and the MATI spectra recorded by $(2+1')$-photon excitation via several different vibration–rotational levels of the $\tilde{B}$ intermediate state.

5.4. *Pulsed field recombination*

The reverse of pulsed-field ionization, known as 'pulsed field recombination', has been demonstrated by Noordam and coworkers [185] and potentially provides a novel means for producing exotic species. The principle is illustrated in figure 28. If an electron and an ion collide in the presence of an electric field then the potential energy of interaction is identical to that shown previously in figure 11(*b*). In a low-energy electron–ion collision, where the collision energy is less than the difference between the saddle point and the field-free ionization limit, the electron will take a small, but non-negligible, time to travel from the saddle point to the nucleus and back; in the experiments carried out this time was of order 1 ns. If, during that time, the field is switched off then the electron will remain bound in a highly excited Rydberg state, and may subsequently decay to lower lying states. The technique may thus provide a means to convert cations into the corresponding neutrals with high efficiency.

The implementation of this rather simple idea requires very precise control of the collision energy and of the timing of the switched field. In the first experiments, a

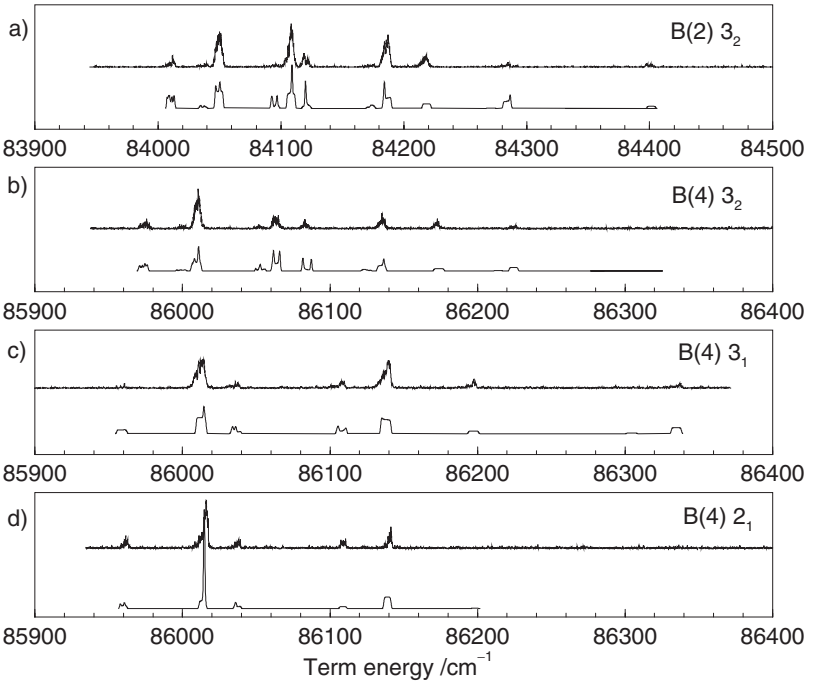

Figure 27. Comparison of the MQDT simulations (lower traces) with experimental MATI spectra (upper traces) originating from four different vibration–rotation levels of the B intermediate state of ammonia (reprinted with permission from ref. [59], copyright (2001) American Chemical Society). Identical quantum defect parameters are used to simulate each spectrum. The intermediate levels for each spectrum are labelled with the quantum numbers $B(\nu_2')J'_{K'}$.

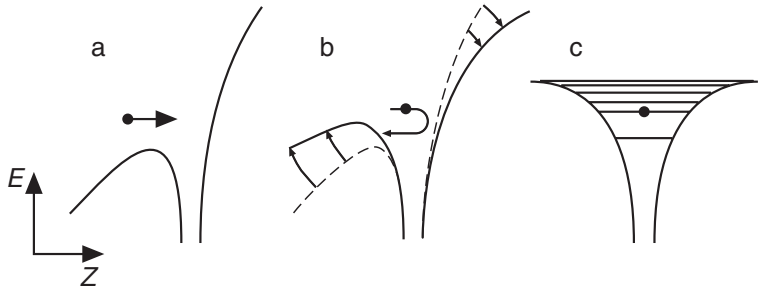

Figure 28. Principles of pulsed-field recombination. The electron collides with the ion at low energy in (*a*) and then the field is switched off (*b*) at the point of collision, trapping the electron in a Rydberg energy level (*c*).

10 ns pulse of $\sim 10^4$ electrons was created by photoionization of lithium and these were directed towards a cloud of ions, which were also formed by photoionization. The electrons were decelerated as they approached the ions such that the turning point of their motion coincided with the position of the ion cloud. A fast pulse generator was used to switch off the field (1.5 V cm^{-1}) in $\sim$1 ns. A second experimental setup employed a Penning trap to store electrons, and then emptied it to produce 4 ns electron pulses. The pulsed-field recombination technique has been

successfully demonstrated for carbon cluster ions, C_{60}^+, C_{50}^+ [186], which were reported to recombine with electrons with an efficiency as high as 6×10^{-2} to produce neutral Rydberg states around $n = 200$. A particularly interesting application has been proposed by Noordam *et al.* [187] involving the recombination of positrons with antiprotons to form neutral antihydrogen atoms. This proposal is under active investigation at CERN.

6. Molecular Rydberg collisions

The macroscopic size of Rydberg molecules makes them highly susceptible to collisional processes. In some experiments these collisional effects cause unwanted complications but in this section we also explore how the study of such collisions offers new possibilities in chemical physics.

6.1. *Collisions with neutral atoms and molecules*

The collision between a Rydberg atom or molecule and a neutral perturber may be regarded as a sum of two parts; the interaction between the perturber and the Rydberg electron, and the interaction between the perturber and the ionic core. Which interaction dominates will depend on the relative cross-sections describing these two types of process. At thermal energies and moderate values of n (e.g., 20) the velocity of the Rydberg electron is much faster than the velocity of the perturber and therefore the interaction between these is physically similar to the scattering of free electrons with the perturber.

As discussed in the literature on atomic Rydberg states [66, 67] the range of the interaction depends critically on the nature of the perturber. For rare-gas atomic perturbers the collision range is quite short as the potential energy of interaction varies as $1/\rho^4$ (where ρ is the electron–perturber separation), and so this charge-induced dipole interaction only occurs once the perturber is well inside the Rydberg orbital. In principle the collision with the Rydberg electron could be inelastic, resulting in transfer of the electronic energy of the Rydberg electron to (or from) the degrees of freedom of the collision partner. For a rare-gas atomic partner, the only degree of freedom available is translational and therefore the transfer of energy is inefficient. Gallagher estimates that for collisions between an $n = 20$ Rydberg orbital and He atoms at 300 K, the mean energy transfer per collision would be expected to be of order $3\,\mathrm{cm}^{-1}$ and generally of order $kT/100\,\mathrm{cm}^{-1}$ [67]. Thus, state-changing processes involve predominantly transfer from the initially excited low-l state into the nearby high-l Stark manifold with little or no change in n. The probability of collisional ionization is very small. At higher n the probability of state changing drops off; the electron density is becoming more and more spread out reducing the probability of an electron–perturber collision.

The situation changes dramatically for collision with molecular partners for two reasons. Firstly, if the molecule is polar then its interaction (charge-dipole) with the Rydberg electron becomes longer range, proportional to $1/\rho^2$; and secondly the molecule has more degrees of freedom from which to transfer energy. As a result much larger exchanges of energy to and from the rotational degrees of freedom of the perturber are possible, especially if the rotational constant of the molecule is large. Hotop and coworkers [188] found that rare-gas Rydberg atoms could be ionized in collisions with polar molecules such as H_2O and NH_3 with cross-sections of $\sim 100\ \mathrm{nm}^2$, but not with non-polar molecules such as H_2 or N_2. For some

molecules such as SF_6 the collisional ionization results in electron attachment to the collision partner to produce, for example, an SF_6^- anion.

However, various experiments have shown that under certain conditions of collision energy and high principal quantum number, the collision partner may pass through the Rydberg orbital leaving the electron untouched and collide instead with the ion core. For example, Pratt *et al.* [189] observed the process

$$H_2^*(n = 30 - 70) + H_2 \rightarrow H_3^* + H \rightarrow H_3^+ + e^-. \tag{29}$$

The reaction cross-section appeared to be independent of the principal quantum number, and the interpretation of this reaction was in terms of an ion–molecule reaction ($H_2^+ + H_2 \rightarrow H_3^+ + H$) taking place within the Rydberg orbit to produce a vibrationally excited H_3^+ ionic core, while the Rydberg electron remained in the same high-n state. This intermediate then undergoes vibrational autoionization to produce the free-product ion. Dehmer and Chupka [190] studied the same process over the range $n = 3$–17 and found that the ion-yield slowly increased as n increased, reaching the value for the equivalent ion–molecule reaction at $n = 14$. The lower rate at low-n was attributed to competition with radiative processes, and also shielding of the ion core by the penetrating Rydberg electron. Davis *et al.* recently studied the collisions between H Rydberg atoms, $n = 30$–50 with O_2 and N_2 molecules at a collision energy of 1.84 eV in a crossed beam apparatus [191]. A major process observed was energy transfer from the Rydberg atom to the vibrational energy levels of the collision partner. This transfer was detected as a change in the momentum of the Rydberg atom, and therefore the results were interpreted in terms of a collision between the H^+ ion core and the collision partner in which the Rydberg electron acts as a spectator. They were able to deduce that more than 25% of these inelastic collisions left the Rydberg electron in a high-n orbital ($n > 20$) so that it could be field-ionized and detected.

The significance of these results is that the study of Rydberg atom/molecule collisions with neutral partners can be used as a means to study ion–molecule reactions. Yang and coworkers have reported such a study on $H^* + D_2$ [192] in which the product rotational state distribution of the HD^+ could be determined from the kinetic energy of the products. In cases where molecular Rydberg states are produced by laser excitation the core quantum states can often be selected and therefore the opportunity is presented for studies of state-to-state ion–molecule dynamics.

6.2. *Collisions with ions*

The perturbing effects of ions on Rydberg states have already been discussed earlier in terms of the inhomogeneous field produced by the ions (see section 3.8). The limit of this process would be the field ionization of the Rydberg state. The outcome could be the capture of the free electron by a perturbing ion (or the direct transfer to it) resulting in Rydberg electron exchange. Schlag and coworkers [193] have produced direct experimental evidence that this can occur in ZEKE-type experiments. They found that when C_6D_6 ions are produced in the neighbourhood of $C_6H_6^*$ ($n > 100$) Rydberg molecules, excited at the frequency of a C_6H_6 ZEKE peak, electron transfer took place with a probability of a few per cent. $n \geq 150$ Rydberg states were removed by a $1\,V\,cm^{-1}$ spoiling field, and after a $\sim 12\,\mu s$ time delay C_6D_6 ions produced by pulsed-field ionization of Rydberg states (after electron transfer) were detected. Calculations to model this effect have been carried out by

Smith and Chupka. They predicted that some extreme states of the Stark manifold could transfer an electron at a rate of 10^8 s^{-1} once an ion had approached within $5n^2a_0$ of the Rydberg molecule [194].

However, under conditions of high ion density, it is possible that this behaviour is a more collective effect in which ionization of many Rydberg electrons causes the formation of a mini-plasma in which a few electrons are trapped by an excess of positive ions. Ions or electrons are released from the plasma if a pulsed field of sufficient magnitude is later applied [195]. A related area of research in atomic physics is the study of 'frozen Rydberg gases' in which a laser-cooled bunch of atoms is excited to Rydberg states and after ejection of a few electrons form stabilized plasmas of the type described above [196].

6.3. *Collisions with surfaces*

The predominant process occurring when a Rydberg atom collides with a metallic surface is known to be tunnelling ionization of the Rydberg electron into the conduction band of the metal [197, 198]. The approach of the Rydberg atom causes the creation of image charges of the ion core and the electron in the metal and the net attractive force lowers and narrows the barrier to ionization of the Rydberg electron, as illustrated in figure 29. At a critical distance from the surface, tunnelling ionization of the Rydberg electron can occur. The position of ionization with respect to the surface has been determined experimentally by Dunning and coworkers [199, 200] using Xe Rydberg atoms incident on an atomically flat Au(111) surface at a grazing incidence angle. A field is applied such as to pull the ions that are formed away from the surface. The closer the ionization occurs with respect to the surface, the greater the field required to extract the ions, as there is an image charge attraction pulling the ion towards the metal. It is found that the position

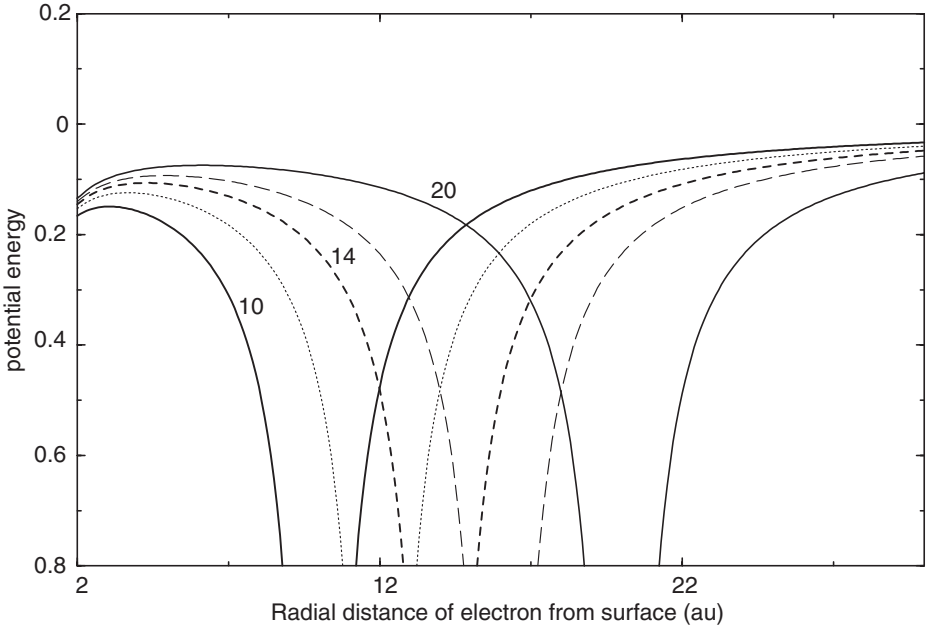

Figure 29. Potential energy of an electron in a Rydberg atom for different distances of the atom from the metal surface (in the range 10–20 n^2a_0).

of ionization varies strongly with n as expected, but if states are populated in the presence of a field, the position of ionization appears to vary little with the Stark state (k quantum number) populated. A red-shifted Stark state is observed to ionize at the same position as a blue-shifted Stark state even though in one case the electron distribution is initially polarized so as to be in between the surface and the ion core, whereas in the other case it is trailing behind the ion core. As explained by Zhou *et al.* [201], the Stark-shifted levels undergo a series of crossings as the surface is approached and the system may pass through these crossings adiabatically such that many switches between red-shifted and blue-shifted character occur.

Calculations have been carried out by Nordlander and coworkers to model these effects [202, 203]. They used a complex scaling method in the solution of the Schrödinger equation for this problem, and a surface potential was determined from density functional theory. The complex scaling method allows lifetimes with respect to electron tunnelling to be calculated for the Rydberg states as a function of distance from the surface; the rate of tunnelling appears as the imaginary part of the complex eigenvalues. Initial calculations were carried out for H-atom Rydberg states [202], but the methodology was subsequently extended to Xe atoms using an effective potential for interaction of the Rydberg electron with the ion core that gave the correct quantum defects [204, 200].

There have been no experiments or theory on the interaction of Rydberg *molecules* with surfaces, but it is of interest to ask whether there are likely to be any differences to the behaviour of Rydberg atoms. The main difference is the possibility that the electric field produced by the image charges could cause a change to the internal couplings between bound states and dissociation/ionization continua, such as to induce competitive processes such as predissociation or autoionization. In experiments we have performed with H_2 Rydberg molecules ($n = 17$) moving towards the high-field region of an electric dipole, such field-induced predissociation is observed to occur, but the probability depends strongly on which Stark state is initially populated [115]. The levels towards the outsides of the Stark manifolds decay much more readily than those at the centre of the manifold. There is also evidence that when the core is rotationally excited, forced autoionization can occur as a field rises by enhancing the coupling to the continuum associated with channels of lower core excitation. The probable occurrence of such processes when a Rydberg molecule approaches a metallic surface may mean that the decay of the Rydberg state occurs over a much narrower range of distances from the surface and therefore the use of Rydberg molecules may prove to be a more sensitive probe of the long-range surface potential.

7. State selection and reactivity of molecular ions

7.1. *State selection by pulsed field ionization*

The development of MATI spectroscopy (section 5.2) led to the idea that the ions that were detected at a given excitation wavelength in the MATI spectrum would be prepared in a well-defined vibration–rotation quantum state [59, 162, 163, 178, 205]. The method should therefore provide a unique approach for studying reactivity, spectroscopy and photodissociation of ions in selected vibration–rotation states. The high-n Rydberg states that are ionized just below a given ion-core threshold would have well-defined core quantum numbers, and when the Rydberg electron is removed, the core quantum numbers remain unchanged. This statement requires

some justification because there have not actually been any experiments which have directly measured the ionic quantum states following pulsed field ionization. For many of the peaks in the MATI spectrum, the field-ionized pseudo-continuum is degenerate with other continua (e.g., for NO the $v^+ = 0$, $N^+ = 2$ high-n Rydberg states are degenerate with the continua of $v^+ = 0$, $N^+ = 1$ and 0). Although it might be assumed that the field ionization of these states would only produce $v^+ = 0$, $N^+ = 2$ ions, it is possible that the field would induce extra couplings to the degenerate continua leading to ions with different rotational quantum numbers, a *forced* autoionization.

Two arguments offer strong evidence that such processes do not occur, at least for the $n > 100$ Rydberg states [162] used in MATI/ZEKE spectroscopy. First there is no reason why forced rotational ionization, if it does occur, should be confined to occur within the field ionization range of a given MATI peak; in general it could also occur below this range and would give rise to long tails on the red side of every ZEKE and MATI peak. The general observance of well-defined field-ionization behaviour in ZEKE and MATI spectroscopy points to the non-occurrence of forced autoionization in the high-n range. Secondly, in order to survive the several-microsecond delay before field ionization, the Rydberg electron must certainly have found its way into a long-lived state with high-l, high-m_l character in which the electron is non-interacting with the core. In this state, forced autoionization, which requires core penetration by the Rydberg electron, cannot occur because the pulsed electric field will preserve the high-m_l value of the Rydberg electron and hence its non-penetrating character.

The pulsed-field ionization technique offers much greater selectivity in the production of state-selected ions than, for example, REMPI methods and in principle it is possible to produce bunches of ions (typically 10^2–10^4 per laser pulse) in any quantum state for which there is a well-resolved peak in the MATI spectrum. Thus, for example, the levels of given J, K_a, K_c for H_2O^+ can be individually selected in this way [163]. In comparison, in the use of REMPI methods, the degree of state selection obtained is dependent on how diagonal are the Franck–Condon factors via the intermediate and how little the rotation changes on ionization. The experimenter has little control over these changes, although favourable cases may be found. In fact the channel interactions that perturb intensities of MATI/ZEKE transitions (see section 5.3) are generally advantageous in that they allow selection of a much wider range of quantum states via a given intermediate than is possible with REMPI.

7.2. *Studies of ion–molecule reactions*

In 1994 Mackenzie *et al*. showed that it was possible to study reactive scattering of ions selected by pulsed-field ionization [206]. The experimental apparatus is shown in figure 30. H_2^+ ions were formed in selected v^+, N^+ by PFI and accelerated to collide with unexcited neutral H_2 molecules within the same molecular beam. H_3^+ ions formed in the reaction $H_2^+ + H_2 \rightarrow H_3^+ + H$ were detected in a quadrupole mass spectrometer and the collision energy could be varied by changing the duration of the accelerating (and ionizing) pulsed field. The results showed no measurable variation in the cross-section with ionic rotational state [206]. A similar lack of variation with rotational state was found for the reaction of H_2^+ with Ar [153]. Subsequently, Anderson and coworkers developed an ion-guide apparatus to determine *absolute* cross-sections for state-selected ion–molecule reactions using pulsed-field ionization for ion preparation. Their study of the hydride-extraction

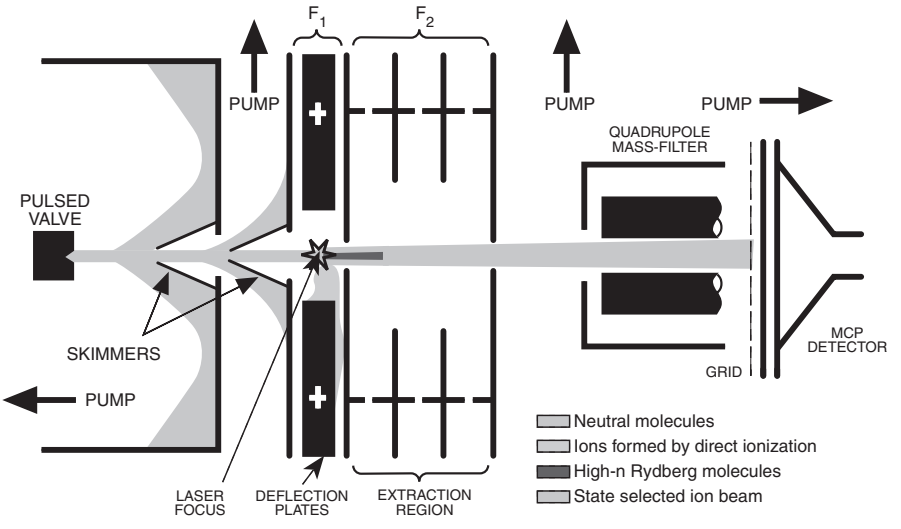

Figure 30. Experimental setup for studying state-selected ion–molecule reactions (from ref. [206]). Rydberg states with well-defined core quantum states are formed by laser excitation between the deflection plates and then are field-ionized and accelerated in the extraction region. Product ions formed further downstream are analysed in a quadrupole mass filter.

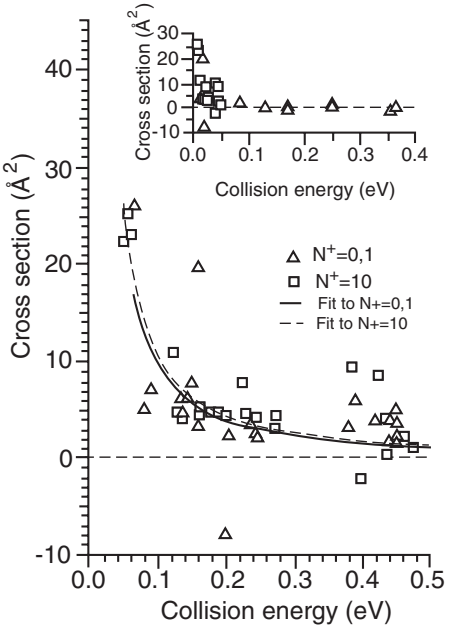

Figure 31. Reaction cross-sections for the $NO^+ + EtOH$ reaction as a function of collision energy for two different selected rotational states of NO^+ (from ref. [207]).

reaction $NO^+ + C_2H_5OH \rightarrow HNO^+ + C_2H_4OH$ [207] also revealed no variation in cross-section over the range of NO^+ rotational quantum numbers $N^+ = 0$ to 10, although a comparable change in translational energy did inhibit the reaction (see figure 31). A precursor complex mechanism has been invoked. Ng and coworkers

have recently developed a similar apparatus at the Chemical Dynamics Beamline at ALS, in which product ions are detected in coincidence with ZEKE electrons [208]. The reaction $H_2^+(v^+ = 0 - 17, N^+ = 1) + Ar$ has been studied and *absolute* cross-sections have again been obtained. An increase in the cross-section from $v^+ = 0$ to 5 was observed, followed by the cross-section leveling off up to $v^+ = 14$. The rate dropped off at higher v^+, an observation that was attributed to dissociation of the product ArH^+.

Given that the few reactions studied so far reveal no significant dependence of the cross-section with ionic *rotational* state it is of interest to ask under what circumstances one might expect some dependence. Such an effect would require a strong anisotropy in the potential energy surface with respect to the orientation of the ionic species relative to the direction of the collision, and thus a preferred orientation for reaction. Increased rotation would then hinder the reaction. Using a long-range force model, the interaction between an ion having a dipolar charge distribution (dipole moment μ_D) and a non-polar neutral molecule of polarizability α (e.g., $CO^+ + H_2 \rightarrow HCO^+ + H$) can be written

$$V(R,\theta) = -\frac{\alpha}{2(4\pi\epsilon_0)^2}\left[\frac{Q^2}{R^4} + \frac{4Q\mu_D\cos\theta}{R^5} + \frac{\mu_D^2}{R^6}(3\cos^2\theta + 1) + \cdots\right] \qquad (30)$$

where Q is the charge on the ion, R is the separation of the two species and θ is the angle between the dipole and the line of centres of the two atoms. The first term is the ion–induced-dipole interaction, while the second represents the interaction between the charge-induced dipole on the neutral and the permanent dipole on the ion. The anisotropy arising from this term should be sufficiently large in some cases for a rotational effect to be observed. Using a statistical adiabatic channel model (SACM) calculation with the capture approximation [209] we have estimated that the rate of reaction of CO^+ with H_2 decreases by approximately 10% when changing the rotational state of CO^+ from 0 to 3 at a collision energy of 10 meV [210]. The model adopted is simplistic but the calculations suggest that at low temperatures this effect may be significant and measureable.

More generally, however, the PFI state-selection method may bring important insight into effects of *vibrational* excitation on ion–molecule reactions, as there are many cases where the superior resolution and the wide range of states that can be accessed will make this technique a method of choice for state-selected studies. For example, Kim *et al.* have used this method to study vibrational mode effects on proton transfer in phenol cation methylamine reactions [211]. Also, following recent experiments involving the imaging of products from photodissociation of a REMPI state-selected molecular ion (Br_2^+) [212], the possibility of using PFI for this purpose also becomes worth considering.

8. Rydberg tagging of chemical reaction products

8.1. *Velocity distributions in chemical reaction dynamics*

An important field in the development of chemical reaction dynamics has been the measurement of nascent velocity distributions of the products of simple reactions. In using the term 'velocity' we refer not only to the speed (or kinetic energy) distribution of these products but also the angular distribution. For the case of photodissociation studies, in which the reaction is unimolecular, the measurement of the kinetic energy distributions of one or both of the products will in general

reveal information about the disposal of the total excess energy into the various internal degrees of freedom of the products, and this disposal can be compared with statistical and dynamical models. Measurement of the angular distribution of products may give details, for example, of the electronic character of the excitation process, and of the rate at which the parent excited state is decaying to products. Furthermore, if the alignment of the rotational angular momentum of the fragments is also determined relative to the dissociation axis, then further information about the torques and forces in the transition state may be obtainable.

For a photodissociation process the energy of the 'collision complex', formed by photoexcitation, is well defined, and this leads to a simple relationship between product kinetic energy and internal energy. For example in the case

$$H_2S + h\nu \rightarrow SH + H \tag{31}$$

conservation of energy requires that, in the centre-of-mass frame in which the H_2S is initially stationary,

$$E_{\text{int}}(H_2S) + h\nu = D_0(HS - S) + KE(H) + KE(SH) + E_{\text{int}}(SH) \tag{32}$$

where E_{int}, the internal energy, is defined with respect to the lowest vibration–rotation level. In a jet-cooled molecular beam $E_{\text{int}}(H_2S)$ may be very small, and given that D_0(HS-H) is a fixed quantity, and the kinetic energies of H and SH, KE(H) and KE(SH), have a fixed relationship determined by momentum conservation ($m_H v_H = -m_{SH} v_{SH}$), there will be a linear relationship of the form

$$KE(H) = \text{constant} - E_{\text{int}}(SH) \tag{33}$$

between the measured kinetic energy and the SH internal energy. Thus measurement of the distribution of KE(H) at sufficiently high energy resolution can be interpreted in terms of the energy levels of SH and the population of those levels. An example of a high-resolution kinetic energy distribution measured for the H atom product of the H_2S photodissociation is shown in figure 32. Each peak corresponds to a vibration–rotation energy level of the SH cofragment.

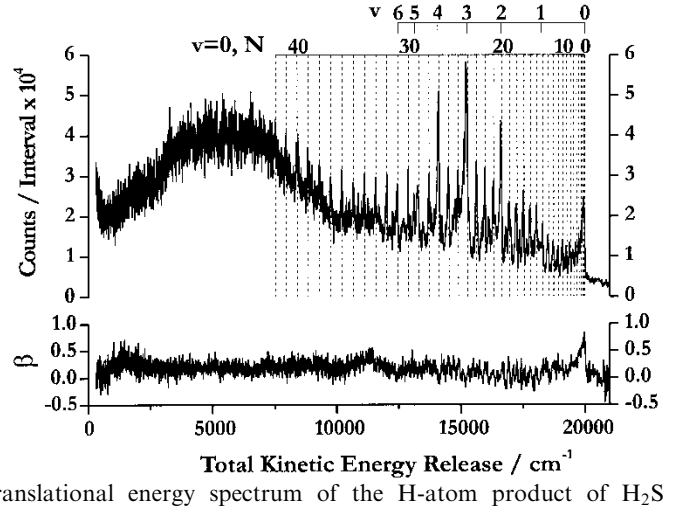

Figure 32. Translational energy spectrum of the H-atom product of H_2S photolysis at 121.6 nm. The energies corresponding to the various vibration–rotation levels of the SH products are indicated above the spectra (from ref. [213]).

These simple energetics have formed the basis of *translational energy spectroscopy*, and in the 1980s this was developed into a flexible and refined tool for studying photodissociation processes, as exemplified by the work of Wodtke and Lee [214]. In their apparatus, the photodissociation of a molecule is initiated by a laser at a fixed time and position, and the fragment atoms ejected in a particular direction pass through a small aperture into a time-of-flight tube. After a fixed distance, the fragments are ionized by electron-impact ionization and detected via a quadrupole mass spectrometer. This allows determination of the kinetic energy of fragments of known mass. An energy resolution ($\Delta E/E$) of order 2% is achievable and limited primarily by the precision of the position of ionization. Rotation of the detector position or the excitation laser polarization allows determination of the angular distribution relative to the laser polarization direction.

Welge and coworkers showed that for experiments involving production of H-atom fragments, an improved kinetic energy resolution could be obtained by resonantly enhanced two-photon ionization of the H atoms immediately following the photoexcitation [215]. This procedure provided better definition of the flight distance than using electron-impact ionization, but these experiments were limited by the 'space-charge repulsion' between H^+ ions produced in the ionization volume; this effect leads to a smearing out of the velocity distribution as it gives the ions an extra acceleration or deceleration in a random direction. The major breakthrough in this field came with the demonstration in 1988 of the *H-atom Rydberg tagging* method by Welge and coworkers.

8.2. *H-atom Rydberg tagging*

The Rydberg-tagging method was designed to overcome the space-charge limitation referred to above [216]. Instead of ionizing the nascent hydrogen atoms immediately following photodissociation, the H atoms were excited to $n \sim 90$ Rydberg states and allowed to fly as neutrals along the time-of-flight tube direction. The Rydberg atoms were then ionized close to the detector and an ion signal recorded. The space-charge repulsion problem was eliminated because the majority of the time of flight occurs while the atoms are still neutral. Ashfold *et al.* [217, 218] and Wittig *et al.* [219, 220] have developed this method to considerable advantage in photodissociation studies and have shown that an energy resolution of order 0.1% is achievable. In cases such as $NH_3 \rightarrow NH_2 + H$ [221] or $H_2S + h\nu \rightarrow SH + H$ (see figure 32) this resolution is sufficient to cleanly resolve peaks in the time-of-flight spectrum associated with population of particular vibration–rotation levels of the NH_2 or SH cofragment. Further details of this method and reviews of early applications can be found in refs [217, 218]. More recent examples include studies of radical photodissociation such as $C_2H_5 \rightarrow C_2H_4 + H$ [222], and a new apparatus applied by Butler and coworkers to photodissociation of acrolein [223].

Welge *et al.* have shown that the Rydberg-tagging technique can also be gainfully employed in measuring the H (or D) atom kinetic energy and angular distributions for bimolecular reactions and have applied it to the $D_2 + H \rightarrow HD + D$ reaction [224], obtaining fully rotationally resolved differential cross-sections for this reaction for the first time [225]. Yang and coworkers have applied the technique to the $H + HD \rightarrow D + H_2$ isotopic variant [226] and also to the $O + H_2 \rightarrow OH + H$ reaction [227].

8.3. *Tagging molecular fragments*

Following the successful work with H-atom Rydberg tagging, the question arises as to whether other atomic or molecular fragments can be tagged in a similar manner. An important point is that the time of flight of the H atom in the experiments described above is typically of the order of hundreds of microseconds to milliseconds and therefore the lifetime of the Rydberg states becomes a serious issue. It is interesting to note that the radiative lifetime of the $90p$ Rydberg state of the H atom is of order 300 μs [67] and therefore it is already somewhat surprising that the H-atom tagging technique is successful. This suggests that small background electric fields are playing a role in the stabilization of the high-n states by l and m_l mixing as discussed in section 4, and indeed small fields (tens of $\mathrm{V\,cm^{-1}}$) have been deliberately applied in some cases. One would expect that the Rydberg states of other atoms would have very similar lifetimes, although heavier atoms will tend to travel more slowly for a given kinetic energy and therefore will generally require longer flight times to achieve the same energy resolution. Rydberg tagging of O atoms has recently been demonstrated in two experiments. Davis and coworkers studied the photodissociation of NO_2 by O-atom time-of-flight spectroscopy [228] and were able to resolve peaks associated with rotational structure in the NO fragment for $J = 19$–23. Houston and coworkers [229] developed a novel approach to studying photodissociation in NO_2 in which they confined the detection of Rydberg-tagged O atoms to those that continued exactly along the parent molecular beam axis. A small aperture was placed in front of the detector, through which the selected fragments passed after 360 μs. In this way they discriminated in favour of 'zero-kinetic-energy fragments' – those that did not have sufficient energy to depart from the original parent beam trajectory – and as they scanned the photodissociation wavelength in the threshold region they were able to observe peaks corresponding to each new dissociation channel $O + NO(v, J)$. In some senses the technique was analogous to threshold photoelectron spectroscopy [124].

However, for Rydberg tagging of *molecules*, where field-free lifetimes might be expected to be of the order of nanoseconds to microseconds even for $n = 100$ it is unclear how successfully the time-of-flight Rydberg tagging method can be applied. While MATI experiments typically employ a delay time of a few microseconds before field ionization, the required Rydberg survival time to obtain good kinetic energy resolution for a molecular fragment would be hundreds of microseconds. Xu *et al*. [230] achieved a successful compromise solution to this problem in their study of the bimolecular reaction $H + D_2 \rightarrow HD + D$ in which the state-specific differential cross-section was determined by Rydberg tagging of the HD fragment. The HD product molecules in the state $v = 4, J = 3$ were excited to $n = 106$ Rydberg states, and allowed to travel for 600 ns before being field-ionized and gently accelerated along a time-of-flight tube. By avoiding space-charge problems in the first few hundred nanoseconds (during which time the volume occupied by the product molecules would expand), the authors were able to obtain a good energy resolution. At the same time, the Rydberg tagging assisted in eliminating background ion signals and was a first demonstration of the possibility of molecular Rydberg tagging in dynamical experiments. The Rydberg state lifetimes were estimated to be of order several microseconds and therefore there was no significant decay of signal.

A different approach to obtaining good kinetic energy resolution using molecular Rydberg tagging, while avoiding long flight times, is to combine Rydberg tagging

with the recently developed ion-imaging methods. In our laboratory we have demonstrated this combination for the first time and applied it to a study of threshold photodissociation of NO_2 as described below.

8.4. *Ion imaging and Rydberg tagging*

In the late 1990s the use of time-of-flight methods for determining energy distributions from photodissociation has been largely superseded in popularity by the use of two-dimensional ion imaging techniques [231] (with the possible exception of H-atom detection). In a time-of-flight method the best energy resolution can only be obtained by restricting the detection to a narrow angular range of the ejected fragments. Thus only a small fraction of the full three-dimensional product distribution is detected. For a completely isotropic distribution, the fragments will form a gradually expanding sphere in the centre-of-mass frame after photodissociation. The idea of the ion-imaging technique is to photoionize the full three-dimensional fragment sphere immediately after dissociation, and then direct the expanding sphere of ions on to a position-sensitive two-dimensional detector to obtain a two-dimensional image. In effect the three-dimensional distribution is squashed on to a two-dimensional surface and therefore the intensity distribution at the detector must then be inverted by an appropriate mathematical procedure to retrieve the original three-dimensional distribution. For the case where there is cylindrical symmetry in the dissociation process (for example with respect to the photolysis laser polarization) the Abel back transform procedure [232] can be used, although a number of other techniques can also be adopted. The full three-dimensional distribution contains both angular information about the predominant direction of fragment ejection with respect to some laboratory-fixed direction (such as the laser polarization) and also energetic information; the larger the size of the expanding distribution, the greater the kinetic energy of the fragments (and conversely the lower the internal energy of the fragments). Although angular information can also be obtained from translational spectroscopy experiments, the information is obtained in an altogether more convenient fashion using imaging detectors.

The technique has primarily been applied to photofragments other than H atoms and in general the ionization is achieved by resonance-enhanced multiphoton ionization. The use of REMPI brings the added benefit that the detection is both species selective and quantum-state selective. When recording a given image, only one vibration-quantum state of the detected product will be resonantly ionized, and so in cases where both fragments can carry internal energy this helps to fix the energy of one of the fragments in the energy balance equation. For example for the case of photodissociation of acetaldehyde $CH_3CHO + h\nu \rightarrow CH_3 + HCO$, the energy balance equation is

$$E_{\text{int}}(CH_3CHO) + h\nu = D_0(CH_3 - CHO) + KE(CH_3) + KE(CHO) + E_{\text{int}}(CH_3) + E_{\text{int}}(CHO). \quad (34)$$

Fixing the CHO internal energy by state-selective ionization not only leads to a simple relationship of the type

$$KE(CHO) = \text{constant} - E_{\text{int}}(CH_3) \quad (35)$$

but also means that it is possible to obtain correlated information about the probability of forming a given internal energy of the CH_3 in conjunction with the selected state of the HCO [233].

A key development in ion-imaging techniques has been the velocity-mapping method first demonstrated by Parker and coworkers [234]. By using an appropriate set of voltages on three cylindrical electrodes (without mesh grids) it is possible to ensure that the position of arrival of the ions at the detector only depends on the velocity component in the plane parallel to the detector, and not on the initial position of ionization. This development has eliminated smearing effects due to the initial spread of positions of the parent molecules in the photolysis laser ionization volume, and allowed an energy resolution $< 1\%$ to be achieved in selected cases and ~ 2–5% in typical cases.

Kitsopoulos and coworkers have demonstrated an alternative approach [235] in which pulsed voltages are applied to the extraction electrodes in such a way as to spread out the expanding fragment sphere in time of flight. By gating the signal arriving at the two-dimensional detector according to time of flight, different segments or slices of the three-dimensional distribution are detected. This then allows a direct reassembly of the full three-dimensional distribution without recourse to an Abel back-transform procedure. Townsend *et al.* have also demonstrated a high-resolution variation of this technique using five electrodes and DC voltages [236].

Despite the impressive achievements of the ion-imaging techniques a number of limitations or potential limitations remain.

1. The space-charge repulsion due to the creation of a number of ions simultaneously will be make a contribution to the energy resolution and this will become more significant if the intensity of the lasers has to be increased to drive multiphoton ionization of the fragments. It will also be more significant when the kinetic energy of the fragments is very low (e.g., near threshold) and therefore the ions are separating slowly. Gallagher and York [237] estimated the space-charge energy broadening using the potential variation across a sphere of uniform charge density ρ and radius r given by $(2/3)\pi a^2\rho$ (in SI units this needs to be multiplied by $1/4\pi\epsilon_0$). For 10^4 ions per mm^3 this gives an energy spread of 11.5 meV or $\sim 100\,cm^{-1}$.
2. When the photofragment is ionized by one-colour REMPI, the electron recoils away from the ion and by momentum conservation must give an opposite kick to the ion. For the detection of light fragments the ion recoil is not insignificant; for example, for an H atom ionized by 2+1 REMPI at 243.17 nm, the total energy release is $13700\,cm^{-1}$ and the velocity given to the ion is 1/1824 times the velocity of the electron which is equal to about $420\,ms^{-1}$ (an energy of $7.5\,cm^{-1}$) [238, 239]. This could typically be of the order of a few per cent of the total fragment velocity.
3. The state-selective detection of one of the fragments by REMPI requires the existence of, and knowledge of, a bound intermediate state at a suitable energy. It also requires a strong transition probability for ionization through that state. Such states are well known for most atoms and for small molecules such as NO but in other cases, e.g., NH_2, CH_2, CO_2, C_2H, stable accessible intermediate states may not exist, or the REMPI spectroscopy

may be unknown, or the ionization might require the use of intense focused lasers to drive weak multiphoton processes.

4. Background ions, produced by non-resonant ionization of fragments, parent molecules, or impurities, will also be accelerated on to the detector in a REMPI–ion imaging experiment and it may not always be possible to eliminate these by time-of-flight methods. In some cases, ionization of the parent may occur and be followed by photodissociation of the ion to produce fragment ions that have the same mass as the fragments that are being imaged, especially if high probe laser intensities are employed. Although the interpretation of these background signals may be straightforward in simple molecules, this may not be the case when studying the photodissociation of larger molecules.
5. The detection of the three-dimensional velocity distribution is always indirect; the distribution is never observed *in situ* but is always accelerated on to a two-dimensional detector where it may be distorted by the acceleration process.

In all these areas the use of Rydberg tagging potentially provides a complementary method that could overcome these limitations.

Figure 33 illustrates the experimental setup used in our laboratory [240, 241] to demonstrate for the first time the combination of Rydberg tagging and ion imaging. This setup was applied to the study of the near-threshold photodissociation of NO_2. A skimmed molecular beam of NO_2 (1% in Ar) is crossed by three tunable pulsed laser beams, one to photodissociate and two to excite the nascent NO fragments to a high-n Rydberg state. The state-selective excitation process is a double-resonant transition proceeding via a selected vibration–rotation level of the A state, in this case starting from the $J = 17/2$ ground state level. The second laser is tuned to excite to the Rydberg states around $n = 130$ for $N^+ = 8$ at the peak of the pulsed-field ionization spectrum.

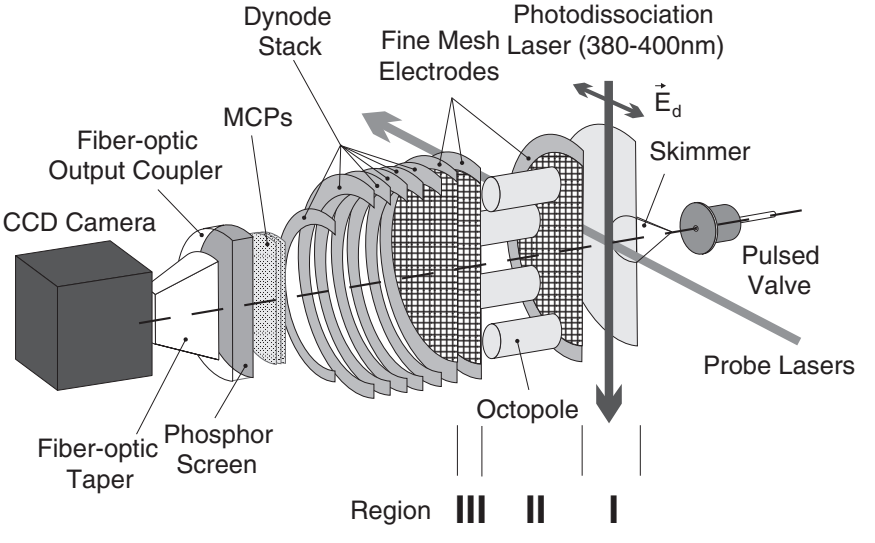

Figure 33. Experimental apparatus for Rydberg tagging/photofragment imaging experiments [240]. The octopole was only used for the inhomogeneous field ionization experiments [241] as described in section 8.6.

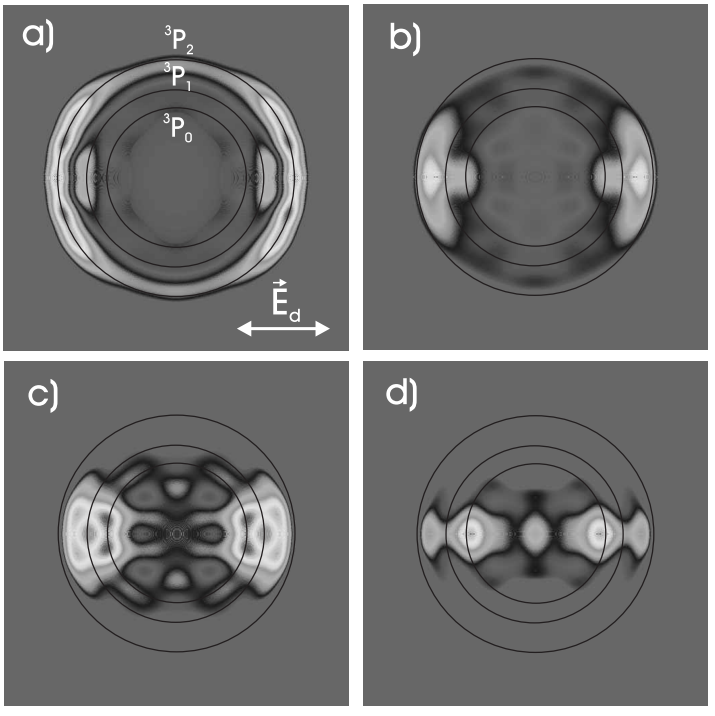

Figure 34. (*a*) Image of Rydberg-tagged NO fragments from NO_2 photodissociation at 390 nm (325 cm^{-1} excess energy) using the aparatus in figure 33 with the octopole at zero potential. (*b*)–(*d*) Images recorded using ±30, ±40 and ±60 V applied to the octopole rods (see section 8.6) (from ref. [241]).

The Rydberg-tagged fragment cloud is then allowed to expand under the original velocity distribution superimposed on the molecular beam stream velocity for a delay of around 20 μs. A small discrimination field is applied to remove any ions formed by one-colour ionization and other mechanisms (with the octopole shown in the figure grounded for these experiments). After 20 μs, a pulsed ionization field is applied and the ions produced are accelerated on to an imaging detector through the dynode system illustrated. A typical Abel-inverted image is shown in figure 34(*a*). The energetics in this case are given by the equation

$$E_{\text{int}}(NO_2) + h\nu = D_0 + KE(NO) + KE(O) + E_{\text{int}}(O^3P_J) + E_{\text{int}}(NO, v = 0, J = 17/2) \quad (36)$$

where $E_{\text{int}}(NO_2)$ is likely to be very small in the supersonic molecular beam. As D_0 and $E_{\text{int}}(NO)$ are fixed, this can be rewritten as

$$KE(NO) = \text{constant} - E_{\text{int}}(O^3P_J) + E_{\text{int}}(NO_2). \quad (37)$$

The O atom can take one of three spin–orbit states $^3P_2$, $^3P_1$ or $^3P_0$ and so for a given photodissociation energy, one might expect to see up to three rings in the image, the one of greatest diameter being that associated with the lowest internal energy product $O(^3P_2)$. In fact at the photodissociation wavelength shown, with 325 cm^{-1} of excess energy available for distribution between kinetic energy and O atom internal

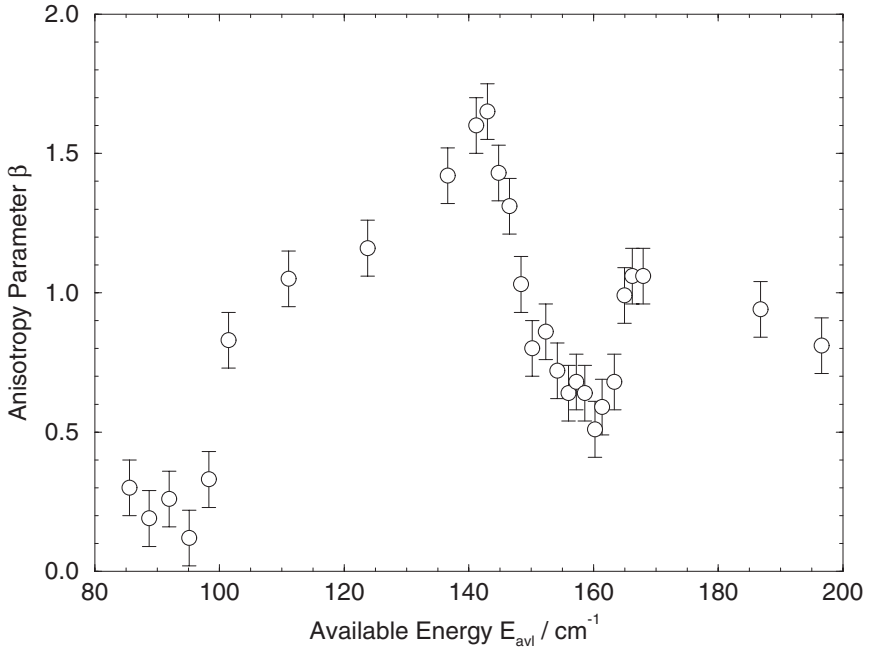

Figure 35. Photofragment anisotropy parameter β as a function of available energy for NO_2 photodissociation near threshold (from ref. [240]).

energy, the outer ring dominates the image as there is the greatest probability for forming this state.

The anisotropy of the image varies very strongly with excitation wavelength and the angular distribution can be fitted to the standard formula

$$I(\theta) = \frac{\sigma}{4\pi}[1 + \beta P_2(\cos\theta)] \tag{38}$$

to obtain values for the anisotropy parameter β. As shown in figure 35 the β parameter changes dramatically even for small changes in the excess energy. Although many factors contribute to the overall variation of β with energy, the dramatic swings are primarily due to variation in the dissociation rate of the parent molecule [240]. The parent molecules absorb the photodissociating light when they are close to a specific orientation (approximately perpendicular in this case) with respect to the polarization vector of the light. When the rate of dissociation is fast compared to rotation of the parent, the direction of ejection of the fragment will be approximately along the orientation axis of the absorbing parent, resulting in a highly anisotropic angular distribution. When the rate of dissociation is slow the molecule will have sufficient time to rotate before fragment ejection, such that the angular distribution becomes more isotropic. In this case resonances in the parent-molecule excited states lead to long-lived complex formation at certain excitation energies.

It should be emphasized that the detection of the signal from the Rydberg-tagged fragments requires the Rydberg states to survive decay by predissociation or autoionization for a period of 20 μs. The field conditions have to be rather carefully controlled in order to achieve these long lifetimes; in particular the discrimination field must be kept very small in the excitation region, not only to avoid field

ionization of the highest Rydberg states, but also to prevent destabilization with respect to predissociation and other decay processes.

8.5. *Advantages of Rydberg tagging in imaging studies*

A number of important points arise from this first demonstration of the Rydberg tagging–ion imaging technique. First, the space-charge repulsion between fragments is eliminated, because by the time the pulsed-field ionization occurs the fragments will be well spread out spatially. In the present case the parent excitation is near the dissociation threshold and the elimination of space-charge repulsion is important as the fragment separation is slow. Secondly, the problem of ion recoil at the point of ionization does not occur as in the case of REMPI above threshold. The ionization process occurs at a subthreshold energy and there is no excess energy for the electron to take away (other than the energy due to acceleration by the field). Thus there is no momentum kick given to the ion when ionization occurs. Thirdly, the ability to use a discrimination field removes all background ions and the only signal arriving at the detector is due to the Rydberg-tagged fragments: there is no need to time-gate the detector to discriminate against other species. This feature could be important if one is trying to spread out the arrival times as in the image-slicing technique [235] (see below). Fourthly, the Rydberg excitation process is state selective as in the case of REMPI studies. For the present example the selectivity is neither better nor worse than in the REMPI case. However, as demonstrated in ZEKE spectroscopy, one-colour VUV excitation can be used as an alternative to two-colour resonant enhanced multiphoton excitation for producing the Rydberg tagged fragments, and such a one-colour excitation can also be achieved with rotational selectivity (e.g., as demonstrated for CH_2, CO_2, N_2, NH_3), i.e., the excitation and detection method is selective for a particular ground state energy level which is excited to the threshold associated with a particular ionic energy level. Thus, VUV Rydberg tagging could provide a useful alternative to REMPI when there is no suitable intermediate state available (e.g., because the intermediate state is short lived or not well characterized). Rydberg tagging could also provide better state selectivity in some cases where excitation via an intermediate state is used. For example, if the transition to the intermediate is dominated by an unresolved Q branch, but then the subsequent transition to the Rydberg states is dominated by well-resolved P and R branches (e.g., [164]) it will be possible to achieve state selection through this double resonant process.

At the present time, however, the energy resolution of the setup illustrated in figure 33 does not match the best resolution achieved by velocity mapping techniques, despite the elimination of space charge and ion recoil effects. The reason for this is that the the velocity-mapping technique compensates for a range of initial parent positions in a way that the present setup cannot. Ideally one might wish to combine velocity mapping with Rydberg tagging, i.e., allow the Rydberg-tagged fragments to expand for a period long enough to allow sufficient dispersion to eliminate space-charge effects, and then field-ionize the states and use the velocity mapping ion optics to map the ions on to the detector. However, this is not easily achieved because continuous potentials are used in the velocity mapping method which are large compared to the discrimination fields used in our setup and would instantly ionize the Rydberg states. In addition a relatively long period of $\sim 10\,\mu s$ is required to separate the Rydberg-tagged fragments from background ions, and the

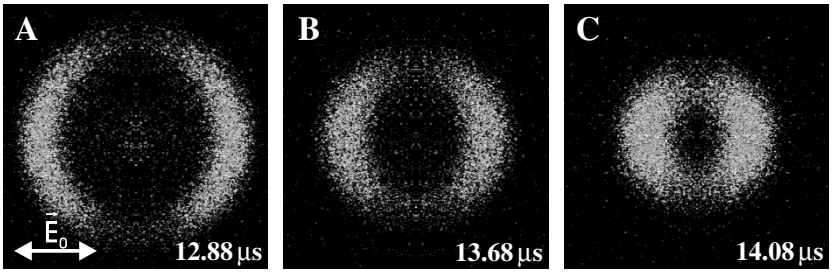

Figure 36. Rydberg tagging with slice imaging: NO fragments from NO_2 photodissociation at 355 nm are Rydberg-tagged, and after 5 μs the spatially distributed fragments are field-ionized and spread out by the applied fields. The images shown correspond to different slices of the time-of-flight distribution (from [242]).

expansion of the fragment cloud may be such as to produce a cloud of ions whose size is too large for the velocity mapping to work well.

As an alternative we have investigated the possibility of combining the pulsed-field slicing technique of Kitsopoulos *et al.* [235] with Rydberg tagging. The authors report comparable energy resolution to velocity mapping and their pulsed-field extraction after a fixed time delay is well suited to the Rydberg tagging and field ionization method. Thus in the variation we have adopted [242] the fragments are initially excited to Rydberg states as before, and then after a time delay of 5 μs, the pulsed extraction fields are applied as in ref. [235] so as to spread out the cloud of ions. The ion images produced in different time-gates for NO_2 photodissociation and NO detection are shown in figure 36. One advantage illustrated is that there is no central background signal due to one-photon background ionization of remnant NO in the NO_2 beam. This first demonstration of the combination of Rydberg tagging with pulsed-field slicing points to the possibility of achieving high resolution in future Rydberg-tagging photodissociation studies.

8.6. *Use of inhomogeneous pulsed-field ionization for spatial discrimination*

In all the imaging experiments described above, the sampling of the spatial distribution of the fragments is *indirect* in the sense that it relies on accelerating the fragments away from the expansion region and on to the two-dimensional detector. The original three-dimensional distribution must then be recovered from the observed image. If the fragments are Rydberg tagged, a new possibility arises of direct sampling of the spatial distribution *in situ*. The principle proposed here is that if an *inhomogeneous* field is applied for field ionization then in some spatial regions the field will be large enough to ionize the fragments, whereas in others it will be too small. Thus only fragments in regions where the field is large enough will be ionized, and this suggests that it may be possible to directly sample the fragment spatial distribution in this way. Two questions then arise. Firstly, is it possible to design inhomogeneous fields in such a way as to be able to select out a small volume of space for field ionization? Secondly, is the field ionization process itself sufficiently sharply defined to allow high spatial resolution. In principle one could imagine two variants of this technique: one in which the only fragments detected are those ionized in the high-field region; the other in which the fragments ionized in the high-field region are eliminated and then those remaining in the low-field regions are detected. It turns out that it is only possible to produce highly localized regions where the field is zero (by cancelling opposing fields) and virtually impossible to produce localized

regions where the field is very high (but away from the electrodes), so that the second approach must be adopted.

A first demonstration of these principles was carried out in our laboratory [241] using the experimental setup shown in figure 33. As before the NO fragments from NO_2 photodissociation were excited to Rydberg states and the fragment cloud allowed to expand. At a fixed time delay after photodissociation, a pulsed field was applied to the octopole to create an inhomogeneous field, which was zero at the centre and increased in the direction moving away from the central axis. The general idea is that the fragments moving at a sufficient distance from the central axis will find themselves at high enough field to be ionized. Those remaining near the axis are unperturbed by the field. Ions produced in the high-field regions are accelerated towards a negative electrode and lost, while other fragments continue and are field ionized by the pulsed field in the extraction region. Thus, the only fragments reaching the detector are those in the low-field region at the time the pulsed octopole field is applied.

Figures 34(*b*)–(*d*) show how one of the images for the NO_2 photodissociation is affected by the octopolar field. As expected the dominant outer ring is removed as the octopolar field is increased, as this results from fragments that will have moved further from the centre when the field is applied. In this way the octopole acts as a spatial filter or electrostatic aperture, and should transmit principally those fragments with near-zero kinetic energy. One of the main limitations revealed by these experiments is that the electrostatic aperture does not have sharp edges because of the predominant *diabatic* field-ionization behaviour. As explained in section 3.2 the field ionization is only expected to be 100% efficient at fields corresponding to $\sqrt{F} \geq E_n/3.1$ (with E_n in cm^{-1}) and the efficiency decreases to 0% over the region of fields down to $\sqrt{F} = E_n/4.6$. Thus in the present experiments, as the red- and blue-shifted Stark states are equally populated, the range of radial distances over which field ionization can take place has a rather fuzzy edge. It is possible, however, that, as in the case of ZEKE spectroscopy (see section 5.1), a double-pulse method could be applied to sharpen this edge. The other point to note about the present setup is that the octopole-field ionization does not simply eliminate the most energetic fragments, because of the range of angles over which fragments are ejected. Since some fragments are ejected along the molecular beam axis, this is not a true kinetic energy analyser but a spatial (or steradiancy) analyser.

With the present configuration of voltages it is only those molecules travelling along the central axis that are transmitted. However, it is possible to use different electrode configurations so that the transmission axis is moved off-centre to a specific radius and angle so that different parts of the three-dimensional distribution can be sampled. Figure 37 illustrates the simulated field for a hexapole [243] in which the voltages have been set so as to produce this off-axis transmission effect. These fields are obtained by superimposing the voltages required to produce a conventional hexapole field with those required to produce a homogeneous field. The voltage on the nth rod is chosen to be

$$V_n = (-1)^{n+1} V_0 + V_{1n} \qquad V_{1n} = V_1 \cos(\phi_n - \phi_0) \tag{39}$$

where ϕ_0 is the angle of the homogeneous field direction and ϕ_n the angular position of the nth rod. Using a field of this type it is possible to selectively transmit tagged molecules passing through two diametrically opposite zero-points in the hexapole field, and to choose the angle and radial position of those zero-points by varying ϕ_0

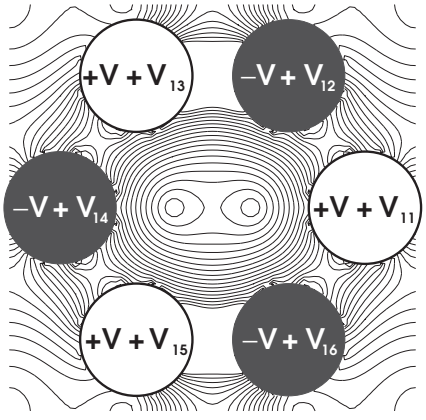

Figure 37. Calculated field magnitudes for a hexapole with voltages applied in the form of equation (39). There are two zero-points in the field where the homogeneous component cancels the inhomogeneous hexapole field.

and V_1. Selection in the third dimension (the propagation direction) can also be achieved in principle by varying the time of application of the hexapole field. These simulations suggest that a methodology could be developed for direct sampling of the full three-dimensional distribution.

9. Manipulation of translational motion

It was pointed out in section 3 that a very large dipole – effectively a permanent dipole – can be created in the Rydberg eigenstates of a molecule in the presence of an electric field. This dipole provides a handle by which it is possible to grab hold of the molecule and control its motion. Controlling the translational motion of gas-phase molecules, particularly through the use of supersonic molecular beams, has played an important role in the development of experiments in reaction dynamics and spectroscopy over the last 40 years [244]. Narrowing the velocity distribution to the order of 1 K in a supersonic beam makes possible scattering experiments with well-defined collision energy (both in the gas phase and at the gas–solid interface) and also spectroscopic measurements with reduced Doppler contribution to the linewidths. Interest in the methodology of translational control has been increased by the recent efforts to create ultracold molecules, following the successful development of laser cooling methods for atoms [245–248]. A gas sample is commonly defined as 'ultracold' if it shows a velocity distribution characteristic of a temperature less than 1 mK. The main approaches employed have been: (a) the use of helium buffer gas cooling combined with magnetic trapping [249], demonstrated for CaH to give temperatures around 400 mK; (b) the photoassociation of alkali-metal atoms cooled in magneto-optical traps [250, 251] to make alkali-metal dimers, giving temperatures as low 20 μK; (c) the use of inhomogeneous electric fields to decelerate molecular beams of dipolar molecules [252–254], for which temperatures of around 10 mK have been achieved for ND_3.

This last approach, developed by Meijer and coworkers and known as the 'Stark decelerator', is perhaps the most general, being applicable in principle to any molecule having a significant dipole and showing a first-order Stark effect. It is an extension of several decades of development of the use of inhomogeneous fields provided by multipolar devices, to deflect, focus and orient beams of dipolar

molecules [255–257]. The principle employed is that the energy of a given eigenstate in an inhomogeneous field varies with field (through the Stark effect) and hence with spatial position, and therefore a force (F) is exerted on the molecule in the direction of decreasing energy ($F = -\nabla.E$). The eigenstates can be classified as either 'high-field seeking' or 'low-field seeking' according to whether the energy decreases with increasing field or increases with field, respectively. For the case of a molecule in a low-field seeking state (blue-shifted Stark state) moving towards the high-field region, it will move up an effective potential energy hill and lose an amount of kinetic energy equal to the energy increase of the state in the field and thus be decelerated. The Stark shift of a molecule in its electronic ground state is normally very small: for ND_3 the $J = 1, M_J = 1$ level changes in energy by $\sim 1\,cm^{-1}$ for a field rise of $150\,kV\,cm^{-1}$, and therefore this is a small change of kinetic energy compared to the kinetic energy of molecules in a molecular beam (typically tens to hundreds of cm^{-1}). Thus multiple high-voltage deceleration stages are required, but Meijer has shown that this is achievable experimentally.

The extreme components of the $n = 17$ Rydberg Stark manifold for H_2 show energy versus field gradients that are approximately 1000 times greater than for ground state ND_3 (and hence a dipole moment that is 1000 times greater). The forces that can be exerted are much stronger and therefore it is of importance to investigate whether this advantage of using Rydberg excitation for Stark deceleration outweighs the obvious disadvantages, namely that these states are expected to have relatively short lifetimes, and that there is a requirement for spectroscopic selection by vacuum ultraviolet or multiphoton excitation. Indeed at the outset of the experiments described below it was not clear whether the lifetimes of any molecular Rydberg states would be sufficient to observe translational control. A key issue that emerges from the recent work reviewed here is that the fields employed for controlling the motion of Rydberg molecules have a significant effect on the lifetimes and that the design of any experiment of this type must take both effects of the field into account.

9.1. *Controlling the motion of molecules in Rydberg states*

The possibility of using Rydberg states for translational control was first reviewed by Wing and coworkers [258] who suggested the use of a quadrupole trap to store Rydberg atoms excited to low-field seeking states. Subsequently Breedon and Metcalf proposed a scheme [259] for the deceleration of Rydberg atoms in a series of stages, using either a sequence of pairs of dipole rods or a sequence of wire grids. It was envisaged that the atoms would de-excite by spontaneous emission between each stage and be coherently re-excited using π-pulses.

The general ideas behind controlling the motion of Rydberg atoms and molecules were discussed by Goodgame and Softley [260] who also estimated the lifetimes of Rydberg atoms around $n = 20$ with respect to decay by spontaneous emission and transitions induced by black-body radiation in the presence of a field. The possibility of using a hexapole for focusing Rydberg beams was also discussed. An experimental demonstration of some of these principles was then carried out by Townsend *et al.* [73] observing the deflection of krypton atoms in the field of an electric dipole. As shown in figure 38, the field of an electric dipole decreases on moving away from the dipole and therefore there will be a force on low-field seeking states in the direction perpendicular to the dipole rods that deflects them away from the dipole. Likewise the high-field seeking states would be deflected towards the dipole. The

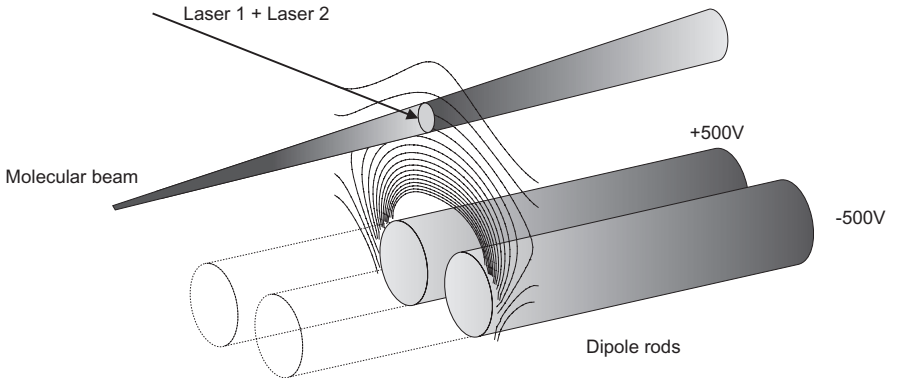

Figure 38. Electric field of a pair of oppositely charged cylindrical rods (from ref. [73]).

atoms were excited to Rydberg Stark states around $n = 18 - 19$ via a $2 + 1'$ multiphoton excitation scheme. The atoms in a supersonic beam were exposed to the field of an electric dipole for up to 40 μs and the trajectories monitored by field ionization and ion imaging. The Rydberg atoms were found to be deflected by up to 3 mm over a 20 cm total flight distance when excited to the extreme low-field or high-field seeking states of $n = 18$. The deflections observed were found to vary in an approximately linear fashion with applied potential and with principal quantum number. Raithel and coworkers also observed deflections of Rb Rydberg atoms in crossed magnetic/electric fields [261, 262]. In that example the strong magnetic field leads to a complex energy map, and the observed deflections were used to gain information about the Stark map energy gradients (i.e., the dipole moments) for the observed states.

There are several issues affecting the choice of optimum principal quantum number for these experiments [260]. On the one hand the Stark shift of the most extreme level of the Stark manifold for a given n increases with n^2 and thus the force on the Rydberg atom or molecule is much greater as n increases for the most extreme Stark states. Furthermore the lifetimes with respect to decay processes increase strongly with n, increasing the length of time over which control can be carried out. On the other hand the spectroscopic selection of a given Stark eigenstate becomes increasingly challenging as n increases, and the field inhomogeneity has an increasingly strong line-broadening effect because of the finite excitation volume (atoms in different parts of the excitation volume experience slightly different fields and therefore absorb at different frequencies). In addition the complications due to avoided level crossings between low-field seeking states of principal quantum number n and high-field seeking states of the Stark manifold $n + 1$ become more prominent as n increases because the density of n states is increasing with n^3. In general one would wish to work in a regime where these avoided crossings do not occur. The atom effectively has a choice of pathway if it reaches the crossing point, and if it is initially in a low-field seeking state it might either choose to continue on that path diabatically or to move adiabatically into the behaviour of a high-field seeking state (see section 3.5). Thus although the gradient of the extreme Stark component increases with n^2, the Inglis–Teller field (where these avoided crossings first occur) decreases as n^{-5}. Thus the overall effect is that if we restrict the field to the range 0 V cm^{-1} to F_{IT} the maximum energy that can be removed per decelera-

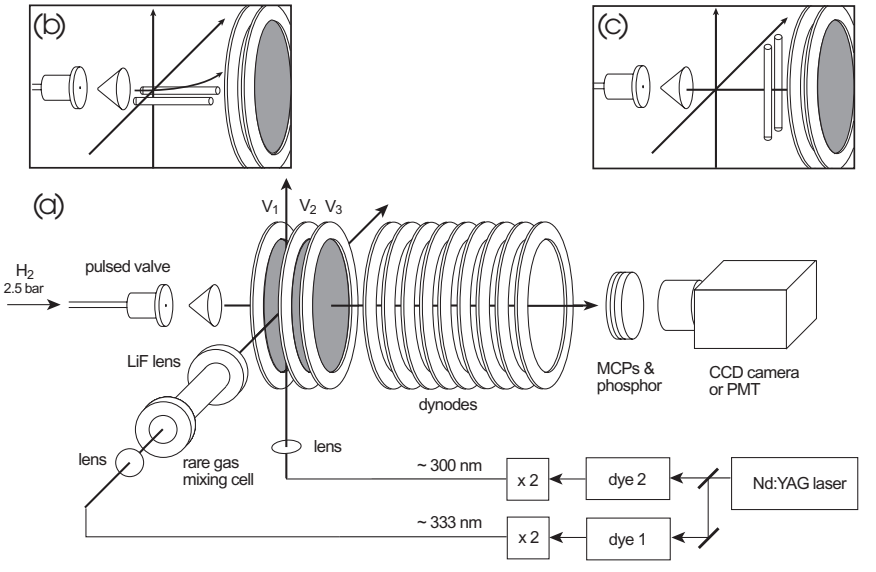

Figure 39. Experimental setup for (*a*) Stark spectroscopy, (*b*) deflection and (*c*) deceleration of molecular hydrogen Rydberg states.

tion stage scales with n^{-3}. For example, suppose we wish to remove $40\,\mathrm{cm}^{-1}$ of the Rydberg atom kinetic energy. For the extreme Stark component of $n = 17$ this requires the atom to move through a field rise of $2161\,\mathrm{V\,cm}^{-1}$ (assuming the Stark energy of this extreme component is given by the hydrogenic expression $E(F) = 6.4025 \times 10^{-5} n^2 F$). The Inglis–Teller field occurs at $1266\,\mathrm{V\,cm}^{-1}$, so that one could conceive of achieving the required field rise in two or three stages. For $n = 100$ the required field rise would only be $62\,\mathrm{V\,cm}^{-1}$ but with the Inglis–Teller field occurring at $0.18\,\mathrm{V\,cm}^{-1}$ (see table 2) then $\sim$350–400 stages of deceleration would be required to avoid passing through level crossings. On the other hand, it is possible that the crossings will be traversed diabatically at higher n and therefore the requirement to work below the Inglis–Teller limit would be relaxed. Nevertheless at this stage we have confined our work to around $n = 15$–20.

As stated above, the main issue with *molecular* Rydberg states is whether the additional mechanisms available for decay, such as predissociation, lead to lifetimes that are too short for observable translational control to be carried out. In our laboratory we have shown [263] that H_2 molecules excited to Rydberg states (of principal quantum number $n = 17$) are sufficiently long lived to demonstrate for the first time the controlled deflection of a neutral non-polar non-magnetic *molecule* in a static electric field. We have also demonstrated that a beam of H_2 molecules could be slowed down or accelerated by the application of inhomogeneous electric fields, pointing the way to the possibility of trapping and cooling of such molecules. The experimental apparatus employed is shown in figure 39. The pure H_2 beam travels at a velocity of $\sim 2600\,\mathrm{ms}^{-1}$ and is crossed perpendicularly by VUV and UV lasers to excite the molecule to the high-n Rydberg states via the $B^1\Sigma_u^+, v = 0, J' = 1$ intermediate level. The states are populated in the presence of the inhomogeneous field due to the electric dipole (as in figures 39(*b*) or (*c*)) and the Stark spectrum near $124\,210\,\mathrm{cm}^{-1}$, which corresponds to a field at the excitation point of $683\,\mathrm{V\,cm}^{-1}$, is shown in figure 40(*a*). The observed Rydberg states have $v^+ = 0$, $N^+ = 2$ core

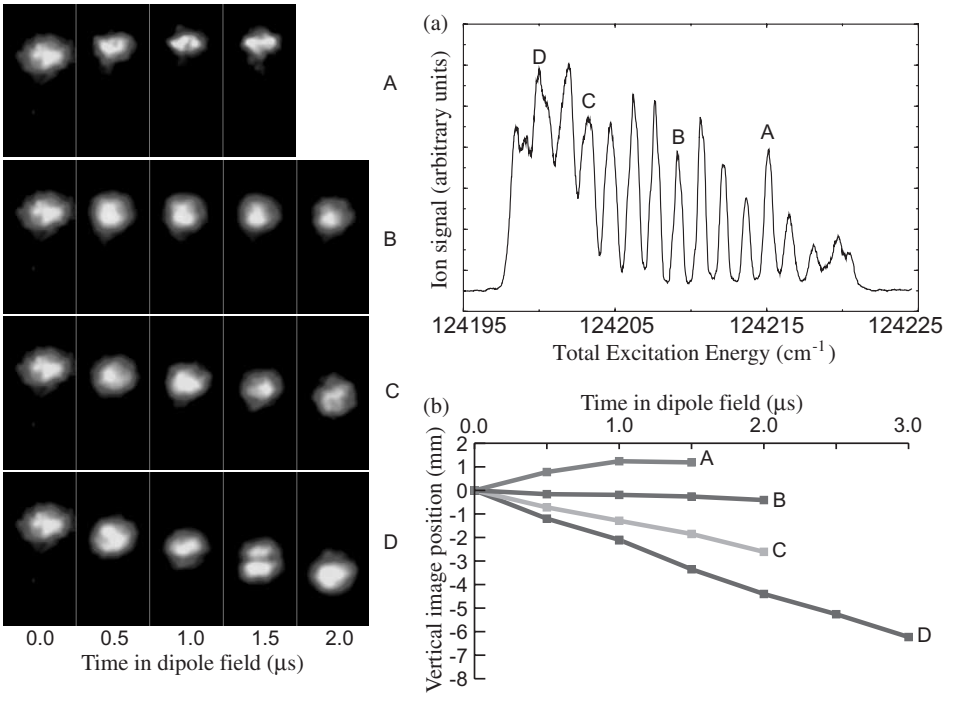

Figure 40. Images recorded in deflection experiments on H_2 Rydberg molecules after 110 μs time of flight. A total of 19 separate images are shown, in which the quantum state populated (labelled A to D for the Stark spectrum shown in inset (*a*)) or the time over which the deflection field is applied is varied. Inset (*b*) shows the centroid averaged positions of the images (reprinted from ref. [263] with permission from Elsevier).

character and the intensity of the mixed-*l* states is derived from the transition to nd, $N^+ = 2$, $J = 1$, $M_J = 0$ series. After exposure to the dipole field for ~1–2 μs, the field is switched off and the Rydberg states travel for >100 μs to the detector under field-free conditions. The Rydberg molecules are ionized at the detector and their positions (displayed by coupling the MCP plates to a phosphor screen) are imaged using a CCD camera, while the time-of-flight distribution can also be recorded. With the dipole in the horizontal configuration (figure 39(*b*)), the high-field seeking states are deflected downwards towards the dipole whereas the low-field seeking states are deflected upwards. Figure 40 shows how the position of images observed at the detector varies with the length of time over which the deflection field is applied, and with the Stark state populated.

When the dipole is rotated so as to be vertical as shown in figure 39(*c*), the high-field seeking states are accelerated towards the dipole whereas the low-field seeking states are decelerated. In either case the dipole field is switched off before the molecules pass through the dipole. The deceleration is detected by measuring the time-of-flight distribution of molecules reaching the detector with the results shown in figure 41. The observed deflections and acceleration/deceleration agree well with classical trajectory simulations based on the potential energy gradients derived from the calculated Stark map and electric fields.

One of the most interesting and complex questions concerns the lifetime of states that are populated, and the fact that they do not decay by predissociation. As

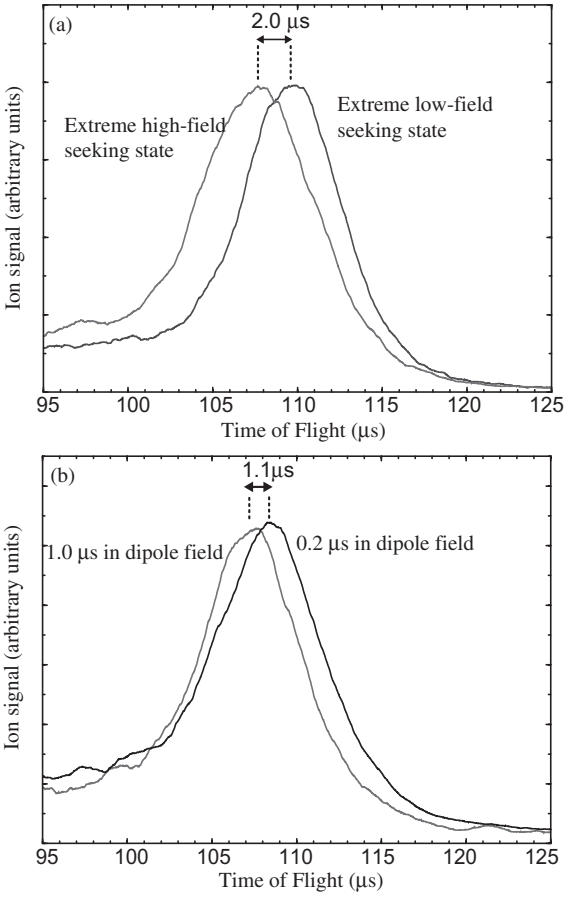

Figure 41. Time-of-flight distributions of H_2 Rydberg states after populating either the extreme high-field seeking state or the extreme low-field seeking state of the $N^+ = 2, n = 17$ Stark manifold and directing the molecular beam towards the dipole as in figure 39(*c*). The dipole field is applied for a fixed time (1.0 μs in (*a*)) before being switched off to allow the molecules to pass through the dipole under field-free conditions (reprinted from ref. [263] with permission from Elsevier).

discussed in section 4, the apparent ~100 μs lifetime is partially associated with the switching off of the field which locks the molecules into long-lived high-*l* states. Even so, it would probably be wrong to assume that there is no evolution of these states during the 100 μs after the field is switched off. The detection by field ionization is not sensitive to the exact quantum state of the Rydberg molecule; indeed it is likely that even very low Rydberg states have sufficient energy to be ionized at the detector. The Rydberg molecules could undergo state-changing radiative processes (spontaneous emission or stimulated absorption or emission by black-body radiation) or collisional processes in this time that would result in molecules that would still be ionized at the detector. The lifetimes for these radiative processes are likely to be very similar to those in atomic systems, and data for the $n = 18$ states given by Gallagher [67] and in our own calculations for Na [260] suggest that a high-*l* state would maybe undergo ~5–10 such state-changing transitions in a 100 μs period. However, the *l* quantum number can only change by 1 in any single process, and the high-*l* character

is thus retained. For example the $n = 17,\ l = 10$ state might radiate to $n = 10,\ l = 9$ or $n = 12,\ l = 11$ but such states remain stable and field-ionizable. Black-body radiation could stimulate transitions back up the ladder of Rydberg states.

Even so, the experiments still require that in the initial period in the field 0–2 μs after excitation, no predissociation or spontaneous emission occurs. Calculated spontaneous emission lifetimes for the Stark-mixed states at $n = 18$ are ~10–30 μs and black-body decay lifetimes are calculated to be ~20 μs giving an overall radiative decay lifetime of ~8–12 μs, so the main concern is probably predissociation. In fact, it turns out that the states with $N^+ = 2,\ M_J = 0$ character that are predominantly populated in these experiments are only very weakly coupled to the dissociation continuum, giving these states an unusual stability, and the field does not enhance the coupling. In general, carrying out these experiments in molecules will require careful selection of excitation scheme and polarization, and possibly the use of very high spectroscopic resolution, to ensure that the population is maximized in states of long lifetime.

The observation of deflection and deceleration of these molecules offers many exciting new prospects including the trapping of Rydberg molecules at very low velocity, focusing of Rydberg beams, and the spatial separation of molecules in different quantum states. The opportunities for high-precision spectroscopy and dynamics experiments will follow from the demonstration of these effects.

10. Conclusion

The previous sections have illustrated the growing number of applications being actively pursued which take advantage of the novel properties of molecular Rydberg states. Although some of these applications are now well-established, such as ZEKE and MATI spectroscopy (section 5), others are only in their infancy, with only a few exploratory experiments carried out to date. In this latter category are the use of pulsed-field ionization for studying the reactivity of state-selected ions (section 7), the use of Rydberg tagging of molecular photofragments in photodissociation dynamics studies (section 8), the control of translational and orientational motion using the Stark effect on Rydberg states (section 9) and the study of reactive collisions of Rydberg molecules both in the gas phase and at surfaces (section 6). In all the applications described here, electric fields play an important role, not only in providing a means to detect the Rydberg states by field ionization, but also in controlling the properties, particularly the lifetime and the dipole moment, of the Rydberg state. The decay of the Rydberg states is potentially a limiting factor in the extension of some of these techniques to a wider range of chemical systems – in the best circumstances this decay takes place on a 10–100 μs timescale and any experiment must work within this timescale. Although some of the general physical principles of how lifetimes are affected by electric fields and charged particles are understood, it is desirable to improve our understanding in order to gain some control over the lifetimes. There remains a need for more detailed experiments to be carried out investigating the dynamical behaviour of Rydberg states, with high spectroscopic resolution, to ensure that well-defined quantum states are populated and under highly controlled conditions of ion density and applied or stray fields. The investigation of the fate of decaying molecules, such as how the population is dispersed by black-body radiation-induced transitions, needs more attention, and also measurements of the extent to which Rydberg molecules behave adiaba-

tically when experiencing changing fields. Likewise, there remains a need to develop rigorous theoretical methods to deal with the dynamics of high Rydberg states of molecules with many nuclear degrees of freedom, many different channels of decay, and in the presence of fields that vary in magnitude and direction as a function of time. In addition, the effects of magnetic fields are relatively unexplored experimentally and theoretically for molecular systems, but these effects are potentially beneficial through the induced mixing of the M quantum number.

The study of Rydberg state properties not only has the potential to contribute to diverse areas of chemical physics as shown in this review, but is a stimulating field in its own right. The intermolecular interaction between Rydberg atoms or molecules at ultralow temperatures is one area where new physics may arise, as is the behaviour of Rydberg molecules at heterogeneous boundaries, and their interaction with intense light sources. There is no doubt that the study of these highly polarizable, flexible, controllable molecules will continue to be an active field for many years to come.

References

[1] A. L. Goodgame, H. Dickinson, S. R. Mackenzie, and T. P. Softley, J. Chem. Phys. **116**, 4922 (2002).
[2] J. R. R. Verlet and H. H. Fielding, Int. Rev. Phys. Chem. **20**, 283 (2001).
[3] G. Herzberg and Ch. Jungen, J. Molec. Spec. **41**, 425 (1972).
[4] H. Lefebvre-Brion and R. W. Field, *Perturbations in the Spectra of Diatomic Molecules* (Academic Press, London, 1986).
[5] J. W. C. Johns, Chem. Soc. Spec. Per. Rep. Mol. Spectrosc. **2**(8), 513 (1974).
[6] A. Giusti, J. Phys. B **13**, 3867 (1980).
[7] V. Kokoouline and C. H. Greene, Phys. Rev. Lett. **90**, 133201 (2003).
[8] V. Kokoouline, C. H. Greene, and B. D. Esry, Nature (London), **412**, 891 (2001).
[9] L. Carata, I. F. Schneider, and A. Suzor-Weiner, Phil. Trans. Roy. Soc. A **355**, 1477 (1997).
[10] I. F. Schneider, I. Rabadan, L. Carata, L. H. Andersen, A. Suzor-Weiner, and J. Tennyson, J. Phys. B **33**, 4849 (2000).
[11] C. Aman and L. Holmlid, Appl. Surf. Sci. **64**, 71 (1993).
[12] L. Holmlid, Langmuir **17**, 268 (2001).
[13] L. Holmlid, J. Phys. Condens. Matter **14**, 13469 (2002).
[14] R. G. Neuhauser, K. Siglow and H. J. Neusser, J. Chem. Phys. **106**, 896 (1997).
[15] C. A. Raptis, J. A. Bacon, and S. T. Pratt, J. Chem. Phys. **112**, 2815 (2000).
[16] M. S. Child and W. L. Glab, J. Chem. Phys. **112**, 3754 (2000).
[17] A. Okasaki, T. Ebata, and N. Mikami, J. Chem. Phys. **114**, 7886 (2001).
[18] J. W. J. Verschur, J. Kinman, H. B. Linden Van Den Heuvell, and M. J. Van Der Wiel, Chem. Phys. **103**, 359 (1986).
[19] T. T. Foltynowicz, J. D. Robinson, and E. R. Grant, J. Chem. Phys. **115**, 878 (2001).
[20] C. A. Raptis and S. T. Pratt, J. Chem. Phys. **115**, 2483 (2001).
[21] K. P. Huber and Ch. Jungen, J. Chem. Phys. **92**, 850 (1990).
[22] C. Y. Ng, Ann. Rev. Phys. Chem. **53**, 101 (2002).
[23] F. Merkt and T. P. Softley, in *High Resolution Laser Photoionization and Photoelectron Studies*, edited by I. Powis, T. Baer and C.-Y. Ng, Wiley Series in Ion Chemistry and Physics (Wiley, Chichester, 1995), Ch. 4.
[24] R. T. Wiedmann and M. G. White, in *High Resolution Laser Photoionization and Photoelectron Studies*, edited by I. Powis, T. Baer and C.-Y. Ng, Wiley Series in Ion Chemistry and Physics (Wiley, Chichester, 1995), Ch. 3.
[25] R. Wallenstein, in *Frontiers of Laser Spectroscopy of Gases* edited by A. C. P. Alves, J. M. Brown, and J. M. Hollas, NATO Adv. Study Inst. Ser C, Vol 234 (Kluwer, Dortrecht, 1988), p. 53.
[26] U. Hollenstein, H. Palm, and F. Merkt, Rev. Sci. Instr. **71**, 4023 (2001).

[27] A. Cromwell, T. Trickl, Y. T. Lee, and A. H. Kung, Rev. Sci. Instr. **60**, 2888 (1989).
[28] R. Seiler, U. Hollenstein, T. P. Softley, and F. Merkt, J. Chem. Phys. **118**, 10024 (2003).
[29] M. C. Bordas, L. J. Lembo, and H. Helm, Phys. Rev. A. **44**, 1817 (1991).
[30] Ch. Bordas and H. Helm, Phys. Rev. A. **45**, 387 (1992).
[31] M. Sommavilla, U. Hollenstein, G. M. Greetham, and F. Merkt, J. Phys. B. **35**, 3901 (2002).
[32] F. Merkt and A. Osterwalder, Int. Rev. Phys. Chem. **21**, 285 (2002).
[33] A. Osterwalder, R. Seiler, and F. Merkt, J. Chem. Phys. **113**, 7939 (2000).
[34] A. Osterwalder, F. Merkt, and Ch. Jungen, (2003) (in preparation).
[35] G. Herzberg and Ch. Jungen, J. Chem. Phys. **77**, 5876 (1982).
[36] P. B. Davies, M. A. Guest, and R. J. Stickland, J. Chem. Phys. **93**, 5417 (1990).
[37] X. M. Qian, T. Zhang, C. Y. Ng, A. H. Kung, and M. Ahmed, Rev. Sci. Instr. **74**, 2784 (2003).
[38] M. J. Seaton, Rep. Prog. Phys. **46**, 167 (1983).
[39] U. Fano, Phys. Rev. A **2**, 353 (1970).
[40] Ch. Jungen, editor, *Molecular Applications of Quantum Defect Theory* (IOP Publishing, Bristol, 1996).
[41] C. H. Greene, A. R. P. Rau, and U. Fano, Phys. Rev. A. **26**, 2441 (1982).
[42] S. Ross, AIP Conference Proceedings No. 225 (American Institute of Physics, New York, 1991), p. 73.
[43] C. H. Greene and Ch. Jungen, Adv. Atom. Molec. Phys. **21**, 51 (1985).
[44] Ch. Jungen, Phys. Rev. Lett. **53**, 2394 (1984).
[45] Ch. Jungen and S. C. Ross, Phys. Rev. A **55**, R2503 (1997).
[46] E. L. Hamilton and C. H. Greene, Phys. Rev. Lett. **89**, 263003 (2002).
[47] N. Y. Du and C. H. Greene, J. Chem. Phys. **85**, 5430 (1986).
[48] T. P. Softley and A. J. Watson, J. Chem. Phys. **101**, 923 (1994).
[49] S. Fredin, D. Gauyacq, M. Horani, Ch. Jungen, F. Lefevre, and F. Masnouseeuws, Molec. Phys. **60**, 825 (1987).
[50] M. S. Child and W. L. Glab, J. Chem. Phys. **112**, 3754 (2000).
[51] Ch. Jungen, K. P. Huber, M. Jungen, and G. Stark, J. Chem. Phys. **118**, 4517 (2003).
[52] A. L. Roche and Ch. Jungen, J. Chem. Phys. **98**, 3637 (1993).
[53] I. Mistrik, R. Reichle, U. Muller, H. Helm, M. Jungen, and J. A. Stephens, Phys. Rev. A. **61**, 033410 (2000).
[54] C. Bordas, P. Labastie, J. Chevaleyre, and M. Broyer, Chem. Phys. **129**, 21 (1989).
[55] E. E. Mayer, H. G. Hedderich, and E. R. Grant, J. Chem. Phys. **108**, 1886 (1998).
[56] M. Drescher, R. Irrgang, M. Spieweck, U. Heinzmann, N. A. Cherepkov, and H. Lefebvre-Brion, J. Chem. Phys. **111**, 10883 (1999).
[57] Ch. Jungen and A. L. Roche, Can. J. Phys. **79**, 287 (2001).
[58] H. Dickinson, D. Rolland, and T. P. Softley, Phil. Trans. Roy. Soc. A **355**, 1585 (1997).
[59] H. Dickinson, D. Rolland, and T. P. Softley, J. Phys. Chem. A **105**, 5590 (2001).
[60] S. C. Ross and Ch. Jungen, Phys. Rev. A **49**, 4353 (1994).
[61] M. Hiyama and M. S. Child, J. Phys. B **35**, 1337 (2002).
[62] F. Texier and Ch. Jungen, Phys. Rev. A **59**, 412 (1999).
[63] H. A. Bethe and E. E. Salpeter, *Quantum Mechanics of One and Two-Electron Atoms* (Springer-Verlag, Berlin, 1957).
[64] L. D. Landau and E. M. Lifschitz, *Quantum Mechanics* (*Non-Relativistic Theory*) (Pergamon, Oxford, 1977).
[65] R. J. Damburg and V. V. Kolosov, J. Phys. B. **12**, 2637 (1979).
[66] R. F. Stebbings and F. B. Dunning, *Rydberg States of Atoms and Molecules* (Cambridge University Press, Cambridge, 1983).
[67] T. F. Gallagher, *Rydberg Atoms*, Cambridge Monographs on Atomic Molecular and Optical Physics, No. 3 (Cambridge University Press, Cambridge, 1994).
[68] G. Valent, Am. J. Phys. **71**, 171 (2003).
[69] F. Merkt, Ann. Rev. Phys. Chem. **48**, 675 (1997).
[70] W. A. Chupka, J. Chem. Phys. **98**, 4520 (1993).
[71] U. Hollenstein, R. Seiler, H. Schmutz, M. Andrist, and F. Merkt, J. Chem. Phys. **115**, 5461 (2001).

[72] D. R. Herrick, J. Chem. Phys. **65**, 3529 (1976).
[73] D. Townsend, A. L. Goodgame, S. R. Procter, S. R. Mackenzie, and T. P. Softley, J. Phys B: Atom. Molec. Opt. Phys. **34**, 439 (2001).
[74] H. H. Fielding and T. P. Softley, J. Phys. B **25**, 4125 (1992).
[75] W. E. Ernst, T. P. Softley, and R. N. Zare, Phys. Rev. A **37**, 4172 (1988).
[76] K. Ito, H. Masuda, Y. Morioka, and K. Ueda, Phys. Rev. A **47**, 1187 (1993).
[77] C. T. W. Lahaye and W. Hogervorst, Phys. Rev. A **39**, 5638 (1989).
[78] G. J. Kuik, W. Vassen, C. T. W. Lahaije, and W. Hogervorst, Z. Phys. D **39**, 127 (1997).
[79] D. J. Armstrong and C. H. Greene, Phys. Rev. A **50**, 4956 (1994).
[80] M. L. Zimmerman, M. G. Littman, M. M. Kash, and D. Kleppner, Phys. Rev. A **20**, 2251 (1979).
[81] H. H. Fielding and T. P. Softley, Chem. Phys. Lett. **185**, 199 (1991).
[82] W. L. Glab, K. Qin, and M. Bistransin, J. Chem. Phys. **102**, 2338 (1995).
[83] J. Chevalyre, C. Bordas, M. Broyer, and P. Labastie, Phys. Rev. Lett. **57**, 3027 (1986).
[84] J. B. M. Warntjes, F. Robicheaux, J. M. Bakker, and L. D. Noordam, J. Chem. Phys. **111**, 2556 (1999).
[85] J. R. Rubbmark, M. M. Kash, M. G. Littman, and D. Kleppner, Phys. Rev. A. **23**, 3107 (1981).
[86] F. Merkt, R. J. Rednall, S. R. Mackenzie, and T. P. Softley, Phys. Rev. Lett. **76**, 3526 (1996).
[87] M. J. J. Vrakking, J. Chem. Phys. **105**, 7336 (1996).
[88] M. Bixon and J. Jortner, J. Chem. Phys. **105**, 1363 (1996).
[89] F. Remacle and R. D. Levine, J. Chem. Phys. **104**, 1399 (1996).
[90] M. Bixon and J. Jortner, J. Chem. Phys. **103**, 4431 (1995).
[91] M. Bixon, J. Jortner, and Y. Dothan, Molec. Phys. **17**, 109 (1969).
[92] U. Fano, Phys. Rev. **124**, 1866 (1961).
[93] D. E. Kelleher, in *Spectral Lineshapes V*, edited by B. Wende (de Gruyter, Berlin, 1981), p. 281.
[94] J. P. Connerade, *Highly Excited Atoms*, Cambridge Monographs on Atomic Molecular and Optical Physics, No. 9 (Cambridge University Press, Cambridge, 1998).
[95] D. A. Harmin, Phys. Rev. A **24**, 2491 (1981).
[96] K. Sakimoto, J. Phys. B **22**, 2727 (1989).
[97] T. P. Softley, A. J. Hudson, and R. Watson, J. Chem. Phys. **106**, 1041 (1997).
[98] M. Feher and P. Martin, Chem. Phys. Lett. **232**, 491 (1993).
[99] A. L. Goodgame, D.Phil. Thesis, Oxford University (2002).
[100] R. M. Jost, J. C. Griffin, B. Friedrich, and D. H. Herschbach, Phys. Rev. Lett. **68**, 1299 (1992).
[101] F. Merkt and R. N. Zare, J. Chem. Phys. **101**, 3495 (1994).
[102] T. P. Softley and R. J. Rednall, J. Chem. Phys. **112**, 7992 (2000).
[103] O. Osterwalder and F. Merkt, Phys. Rev. Lett. **82**, 1831 (1999).
[104] W. A. Chupka, J. Chem. Phys. **99**, 5800 (1993).
[105] M. J. J. Vrakking and Y. T. Lee, J. Chem. Phys. **102**, 8818 (1995).
[106] U. Even, R. D. Levine, and R. Bersohn, J. Phys. Chem. **98**, 3472 (1994).
[107] G. M. Greetham, U. Hollenstein, R. Seiler, W. Ubachs, and F. Merkt, Phys. Chem. Chem. Phys. **5**, 2528 (2003).
[108] F. Merkt, S. R. Mackenzie, and T. P. Softley, J. Chem. Phys. **103**, 4509 (1995).
[109] J. B. M. Warntjes and L. D. Noordam, J. Chem. Phys. **115**, 4150 (2001).
[110] M. Bixon and J. Jortner, J. Chem. Phys. **103**, 4431 (1995).
[111] F. Remacle and M. J. J. Vrakking, J. Phys. Chem. A **102**, 9507 (1998).
[112] M. J. J. Vrakking, I. Fischer, D. M. Villeneuve, and A. Stolow, J. Chem. Phys. **103**, 4538 (1995).
[113] H. Palm, R. Signorell, and F. Merkt, Phil. Trans. Roy. Soc. London Ser. A **355**, 1551 (1997).
[114] S. R. Procter, M. J. Webb, and T. P. Softley, Farad. Discuss. **115**, 277 (2000).
[115] Y. Yamakita, S. R. Procter, F. Merkt, and T. P. Softley, (2004) (submitted).
[116] L. Y. Baranov, A. Held, H. L. Selzle, and E. W. Schlag, Chem. Phys. Lett. **291**, 311 (1998).

[117] A. Held, L. Y. Baranov, H. L. Selzle, and E. W. Schlag, Chem. Phys. Lett. **291**, 318 (1998).
[118] U. Aigner, L. Y. Baranov, H. L. Selzle, and E. W. Schlag, J. Elec. Spec. Rel. Phen. (Sp. Iss.) **112**, 175 (2000).
[119] E. Murgu, J. D. D. Martin, and T. F. Gallagher, J. Chem. Phys. **115**, 7032 (2001).
[120] M. Y. Ivanov and A. Stolow, Chem. Phys. Lett, **265**, 231 (1997).
[121] S. T. Park, H. L. Kim, and M. S. Kim, Bull. Kor. Chem. Soc. **23**, 1247 (2002).
[122] K. Müller-Dethlefs, M. Sander, and E. W. Schlag, Chem. Phys. Lett. **112**, 291 (1984).
[123] G. Reiser, W. Habenicht, K. Müller-Dethlefs, and E. W. Schlag, Chem. Phys. Lett. **152**, 119 (1988).
[124] W. B. Peatman, T. B. Borne, and E. W. Schlag, Chem. Phys. Lett. **3**, 492 (1969).
[125] H. J. Dietrich, K. Müller-Dethlefs, and L. Y. Baranov, Phys. Rev. Lett. **76**, 3530 (1996).
[126] C. E. H. Dessent, S. R. Haines, and K. Müller-Dethlefs, Chem. Phys. Lett. **315**, 103 (1999).
[127] H. Park and R. N. Zare, J. Chem. Phys. **106**, 2239 (1997).
[128] K. Müller-Dethlefs and P. Hobza, Chem. Rev. **100**, 143 (2000).
[129] E. W. Schlag, *ZEKE Spectroscopy* (Cambridge University Press, Cambridge, 1998).
[130] K. Müller-Dethlefs, O. Dopfer, and T. G. Wright, Chem. Rev. **94**, 1845 (1994).
[131] C. E. H. Dessent and K. Müller-Dethlefs, Chem. Rev. **100**, 3999 (2000).
[132] C. Y. Ng, Ann. Rev. Phys. Chem. **53**, 101 (2002).
[133] F. Merkt and T. P. Softley, Phys. Rev. A **46**, 302 (1992).
[134] F. Merkt and T. P. Softley, J. Chem. Phys. **96**, 4149 (1992).
[135] W. Kong and J. W. Hepburn, Can. J. Phys. **72**, 1284 (1994).
[136] A. Mank, T. Nguyen, J. D. D. Martin, and J. W. Hepburn, Phys. Rev. A **51**, R1 (1995).
[137] W. Habenicht, G. Reiser, and K. Müller-Dethlefs, J. Chem. Phys. **95**, 4809 (1991).
[138] S. Willitsch, A. Haldi, and F. Merkt, Chem. Phys. Lett. **353**, 167 (2002).
[139] R. Lindner, K. Müller-Dethlefs, E. Wedeum, K. Haber, and E. R. Grant, Science, **271**, 1698 (1996).
[140] M. Ford, R. Lindner, and K. Müller-Dethlefs, Molec. Phys. **101**, 705 (2003).
[141] X. Tong, S. Ullrich, C. E. H. Dessent, and K. Müller-Dethlefs, Phys. Chem. Chem. Phys. **4**, 2578 (2002).
[142] D. S. Yang, Coord. Chem. Rev. **214**, 187 (2001).
[143] I. M. Waller, T. N. Kitsopoulos, and D. M. Neumark, J. Phys. Chem. **94**, 2240 (1990).
[144] V. Distelrath and U. Boesl, Farad. Discuss. **117**, 161 (2000).
[145] D. M. Neumark, Acc. Chem. Res. **26**, 33 (1993).
[146] I. Fischer, Int. J. Mass. Spec. **216**, 131 (2002).
[147] S. Willitsch, J. M. Dyke, and F. Merkt, Helv. Chim. Acta **86**, 1152 (2003).
[148] R. Signorell and F. Merkt, Farad. Discuss. **117**, 351 (2000).
[149] R. Signorell and F. Merkt, J. Chem. Phys. **110**, 2309 (1999).
[150] F. Merkt and P. M. Guyon, J. Chem. Phys. **99**, 3400 (1993).
[151] K. M. Weitzel, G. K. Jarvis, M. Malow, T. Baer, and C. Y. Ng, Phys. Rev. Lett. **86**, 3526 (2001).
[152] T. K. Ha, P. Rupper, A. Wuest, and F. Merkt, Molec. Phys. **101**, 827 (2003).
[153] D. Rolland, D.Phil. Thesis. University of Oxford (1998).
[154] X. Zhang and J. L. Knee, Farad. Discuss. **97**, 299 (1994).
[155] J. D. Pitts, J. L. Knee, and S. Wategaonkar, J. Chem. Phys. **110**, 3378 (1999).
[156] M. J. Watkins and M. C. R. Cockett, J. Chem. Phys. **113**, 10560 (2000).
[157] R. Seiler, U. Hollenstein, G. M. Greetham, and F. Merkt, Chem. Phys. Lett. **346**, 201 (2001).
[158] A. Osterwalder, S. Willitsch, and F. Merkt, J. Molec. Struct. (Sp. Iss.) **599**, 163 (2001).
[159] M. S. Ford, S. R. Haines, I. Pugliesi, C. E. H. Dessent, and K. Müller-Dethlefs, J. Elec. Spec. Rel. Phen. (Sp. Iss.) **112**, 231 (2000).
[160] L. Zhu and P. M. Johnson, J. Chem. Phys. **94**, 5769 (1991).
[161] A. B. Burrill and P. M. Johnson, Chem. Phys. Lett. **350**, 473 (2001).
[162] T. P. Softley, S. R. Mackenzie, F. Merkt, and D. Rolland, Adv. Chem. Phys. **101**, 667 (1997).

[163] H. Dickinson, S. R. Mackenzie, and T. P. Softley, Phys. Chem. Chem. Phys. **2**, 4669 (2000).
[164] H. Dickinson, T. Chelmick, and T. P. Softley, Chem. Phys. Lett. **338**, 37 (2001).
[165] O. L. A. Monti, H. A. Cruse, S. R. Mackenzie, and T. P. Softley, Chem. Phys. Lett. **333**, 146 (2001).
[166] J. E. Braun and H. J. Neusser, Mass. Spec. Rev. **21**, 16 (2002).
[167] D. P. Taylor, J. G. Goode, J. E. Leclaire, and P. M. Johnson, J. Chem. Phys. **103**, 6293 (1995).
[168] J. E. Leclaire, R. Anand, and P. M. Johnson, J. Chem. Phys. **106**, 6785 (1997).
[169] R. Anand, J. E. Leclaire, and P. M. Johnson, J. Phys. Chem. **103**, 2618 (1999).
[170] A. Fujii and N. Mikami, J. Elec. Spec. Rel. Phen. **108**, 21 (2000).
[171] M. Honda, A. Fujii, E. Fujimaka, T. Ebata, and N. Mikami, J. Phys. Chem. A **107**, 3678 (2003).
[172] M. Gerhards, M. Schiwek, C. Unterberg, and K. Kleinermanns, Chem. Phys. Lett. **297**, 515 (1998).
[173] J. G. Goode, J. E. Leclaire, and P. M. Johnson, Int. J. Mass. Spec. Ion. Proc. **159**, 49 (1996).
[174] A. D. Buckingham, B. J. Orr, and J. M. Sichel, Phil. Trans. Roy. Soc. London **A268**, 147 (1970).
[175] J. Xie and R. N. Zare, J. Chem. Phys. **97**, 2891 (1992).
[176] J. Xie and R. N. Zare, J. Chem. Phys. **93**, 3033 (1990).
[177] F. Merkt and T. P. Softley, Int. Rev. Phys. Chem. **12**, 205 (1993).
[178] S. R. Mackenzie, F. Merkt, E. J. Halse, and T. P. Softley, Molec. Phys. **86**, 1283 (1995).
[179] Ch. Yeretzian, R. H. Hermann, H. Ungar, H. L. Selzle, E. W. Schlag, and S. H. Lin, Chem. Phys. Lett. **239**, 61 (1995).
[180] M. T. Lee, K. Wang, and V. Mckoy, J. Chem. Phys. **97**, 3108 (1992).
[181] M. T. Lee, K. Wang, V. Mckoy, and L. E. Machado, J. Chem. Phys. **97**, 3905 (1992).
[182] K. Wang, M. T. Lee, V. Mckoy, R. T. Wiedmann, and M. G. White, Chem. Phys. Lett. **219**, 397 (1994).
[183] K. J. Müller-Dethlefs, J. Chem. Phys. **95**, 4821 (1991).
[184] R. Signorell and F. Merkt, Molec. Phys. **92**, 793 (1997).
[185] C. Wesdorp, F. Robicheaux, and L. D. Noordam, Phys. Rev. A **64**, 033414 (2001).
[186] C. Wesdorp, F. Robicheaux, and L. D. Noordam, Chem. Phys. Lett. **323**, 192 (2000).
[187] C. Wesdorp, F. Robicheaux, and L. D. Noordam, Phys. Rev. Lett. **84**, 3799 (2000).
[188] H. Hotop and A. Niehaus, J. Chem. Phys. **47**, 2506 (1967).
[189] S. T. Pratt, J. L. Dehmer, P. M. Dehmer, and W. A. Chupka, J. Chem. Phys. **101**, 882 (1994).
[190] P. M. Dehmer and W. A. Chupka, J. Phys. Chem. **99**, 1686 (1995).
[191] B. R. Strazisar, C. Lin, and H. F. Davis, Phys. Rev. Lett. **86**, 3997 (2001).
[192] X. Yang, D. Dai, C. C. Wang, and S. A. Harich, Abstracts. 225th National Meeting ACS, Phys. 494 (2003).
[193] C. E. Alt, W. G. Scherzer, H. L. Selzle, and E. W. Schlag, Chem. Phys. Lett. **224**, 366 (1994).
[194] J. M. Smith and W. A. Chupka, J. Chem. Phys. **103**, 3436 (1995).
[195] R. Signorell and F. Merkt, in *The Role of Rydberg States in Spectroscopy and Photochemistry*, edited by C. Sandorfy (Kluwer, Dordrecht, 1999).
[196] M. P. Robinson, B. Laburthe-Tolva, M. W. Noel, T. F. Gallagher, and P. Pilet, Phys. Rev. Lett. **85**, 4466 (2000).
[197] C. Fabre, M. Gross, J. M. Raimond, and S. Haroche, J. Phys. B, **16**, L671 (1983).
[198] D. F. Gray, Z. Zhang, K. A. Smith, and F. B. Dunning, Phys. Rev. A **38**, 1601 (1988).
[199] S. B. Hill, C. B. Haich, Z. Zhou, P. Nordlander, and F. B. Dunning, Phys. Rev. Lett. **85**, 5444 (2000).
[200] F. B. Dunning, H. R. Dunham, C. Oubre, and P. Nordlander, Nucl. Instr. Meth. Phys. Res. B **203**, 69 (2003).
[201] Z. Zhou, C. Oubre, S. B. Hill, P. Nordlander, and F. B. Dunning, Nucl. Instr. Meth. Phys. Res. B **193**, 403 (2002).
[202] P. Nordlander and J. C. Tully, Phys. Rev B **42**, 5564 (1990).

[203] P. Nordlander and F. B. Dunning, Phys. Rev. B **53**, 8083 (1996).
[204] C. Oubre, P. Nordlander, and F. B. Dunning, J. Phys. Chem. B **106**, 8338 (2002).
[205] F. Merkt, S. R. Mackenzie, and T. P. Softley, J. Chem. Phys. **99**, 4213 (1993).
[206] S. R. Mackenzie and T. P. Softley, J. Chem. Phys. **101**, 10609 (1994).
[207] R. J. Green, J. Qian, H. T. Kim, and S. L. Anderson, J. Chem. Phys. **113**, 3002 (2000).
[208] X. M. Qian, T. Zhang, Y. H. Chiu, D. J. Levandier, J. S. Miller, R. A. Dressler, and C. Y. Ng, J. Chem. Phys. **118**, 2455 (2003).
[209] D. C. Clary, Molec. Phys. **54**, 605 (1985).
[210] H. Dickinson and T. P. Softley (1996) (unpublished results).
[211] H. T. Kim, R. J. Green, and S. L. Anderson, J. Chem. Phys. **112**, 10831 (2000).
[212] M. Beckert, S. J. Greaves, and M. N. R. Ashfold, Phys. Chem. Chem. Phys. **5**, 308 (2003).
[213] P. A. Cook, S. R. Langford, R. N. Dixon, and M. N. R. Ashfold, J. Chem. Phys. **114**, 1672 (2001).
[214] A. M. Wodtke and Y. T. Lee, in *Molecular Photodissociation Dynamics*, edited by M. N. R. Ashfold and J. E. Baggott (Royal Society of Chemistry, London, 1987), p. 31.
[215] X. Xie, L. Schneider, H. Wallmeier, R. Boettner, K. H. Welge, and M. N. R. Ashfold, J. Chem. Phys. **92**, 1608 (1990).
[216] L. Schneider, W. Meier, K. H. Welge, M. N. R. Ashfold, and C. M. Western, J. Chem. Phys. **92**, 7027 (1990).
[217] M. N. R. Ashfold, D. H. Mordaunt, and S. H. S. Wilson, Adv. Photochem. **21**, 217 (1996).
[218] M. N. R. Ashfold, I. R. Lambert, D. H. Mordaunt, G. P. Morley, and C. M. Western, J. Phys. Chem. **96**, 2938 (1992).
[219] J. Zhang, M. Dulligan, J. Segall, Y. Wen, and C. Wittig, J. Phys. Chem. **99**, 13680 (1995).
[220] D. Chastaing, J. Underwood, and C. Wittig, J. Chem. Phys. **119**, 928 (2003).
[221] M. N. R. Ashfold, R. N. Dixon, M. Kono, D. H. Mordaunt, and C. L. Reed, Phil. Trans. Roy. Soc. A **355**, 1659 (1997).
[222] G. Amaral, K. Xu, and J. Zhang, J. Chem. Phys. **114**, 5164 (2001).
[223] B. F. Parsons, D. E. Szpunar, and L. J. Butler, J. Chem. Phys. **117**, 7889 (2002).
[224] L. Schneider, K. Seekamp-Rahn, F. Liedeker, H. Steuwe, and K. H. Welge, Farad. Discuss. **91**, 259 (1991).
[225] L. Schneider, K. Seekamp-Rahn, E. Wrede, and K. H. Welge, J. Chem. Phys. **107**, 6175 (1997).
[226] D. X. Dai, C. C. Wang, S. A. Harich, X. M. Yang, S. D. Chao, and R. T. Skodje, Science **300**, 1730 (2003).
[227] X. H. Liu, J. J. Lin, S. A. Harich, and X. M. Yang, Phys. Rev. Lett. **86**, 408 (2001).
[228] C. Lin, M. F. Witinski, and H. F. Davis, J. Chem. Phys. **119**, 251 (2003).
[229] J. A. Mueller, S. A. Rogers, and P. L. Houston, J. Phys. Chem. A **102**, 9666 (1998).
[230] H. Xu, N. A. Schafer, F. Merkt, D. J. Hughes, M. Springer, R. P. Tuckett, and R. N. Zare, J. Chem. Phys. **103**, 5157 (1995).
[231] A. J. R. Heck and D. W. Chandler, Ann. Rev. Phys. Chem. **46**, 335 (1995).
[232] L. M. Smith, D. R. Keefer, and S. I. Sudharasanan, J. Quant. Spec. Rad. Transf. **39**, 367 (1987).
[233] H. A. Cruse and T. P. Softley (2004) (to be published).
[234] A. T. J. B. Eppink and D. H. Parker, Rev. Sci. Instr. **68**, 3477 (1997).
[235] C. R. Gebhardt, T. P. Rakitzis, P. C. Samartzis, V. Ladopoulos, and T. N. Kitsopoulos, Rev. Sci. Instr. **72**, 3848 (2001).
[236] D. Townsend, M. P. Minitti, and A. G. Suits, Rev. Sci. Instr. **74**, 2530 (2003).
[237] A. C. Gallagher and G. York, Rev. Sci. Instr. **45**, 662 (1974).
[238] D. H. Parker, R. F. Delmdahl, B. B. L. G. Bakker, and H. P. Looek, J. Chin. Chem. Soc. **48**, 327 (2001).
[239] S. Manzhos, H. P. Loock, B. L. G. Bakker, and D. H. Parker, J. Chem. Phys. **117**, 9347 (2002).
[240] O. L. A. Monti, H. Dickinson, S. R. Mackenzie, and T. P. Softley, J. Chem. Phys. **112**, 3699 (2000).

[241] O. L. A. Monti, H. A. Cruse, S. R. Mackenzie, and T. P. Softley, J. Chem. Phys. **115**, 7924 (2001).
[242] H. A. Cruse and T. P. Softley (2004) (to be published).
[243] H. A. Cruse, D.Phil. Thesis, Oxford University (2003).
[244] G. Scholes, editor, *Atomic and Molecular Beam Methods* (Oxford University Press, Oxford, 1988), Vol. 1.
[245] S. Chu, Rev. Mod. Phys. **70**, 685 (1998).
[246] M. H. Anderson, J. R. Ensher, M. R. Matthews, C. E. Wieman, and E. A. Cornell, Science **269**, 168 (1995).
[247] W. D. Phillips, Rev. Mod. Phys. **70**, 721 (1998).
[248] H. J. Metcalf and P. Van Der Straten, *Laser Cooling and Trapping* (Springer, New York, 1999).
[249] J. M. Doyle, B. Friedrich, J. Kim, and D. Patterson, Phys. Rev. A **52**, R2515 (1995).
[250] A. Fioretti, D. Comparat, A. Crubellier, O. Dulieu, F. Masnou-Seeuws, and P. Pillet, Phys. Rev. Lett. **80**, 4402 (1998).
[251] R. Wymar, R. S. Freeland, D. J. Han, C. Ryu, and D. J. Heinzen, Science **287**, 1016 (2000).
[252] H. L. Bethlem, G. Berden, and G. Meijer, Phys. Rev. Lett. **83**, 1558 (1999).
[253] H. L. Bethlem, F. M. H. Crompvoerts, R. T. Jongma, J. Y. T. Van De Meerakker, and G. Meijer, Phys. Rev. A **65**, 053416 (2002).
[254] H. L. Bethlem and G. Meijer, Int. Rev. Phys. Chem. **22**, 73 (2003).
[255] D. H. Parker and R. B. Bernstein, Ann. Rev. Phys. Chem. **40**, 561 (1989).
[256] S. E. Novick, P. B. Davies, P. B. Dyke, and W. Klemperer, J. Am. Chem. Soc. **95**, 8547 (1973).
[257] J. Reuss, in *Atomic and Molecular Beam Methods*, edited by G. Scholes (Oxford University Press, Oxford, 1988), Vol. 1, p. 277.
[258] W. H. Wing, Phys. Rev. Lett. **45**, 631 (1980).
[259] T. Breedon and H. Metcalf, Phys. Rev. Lett. **47**, 1726 (1981).
[260] A. L. Goodgame and T. P. Softley, J. Phys. B: Atom. Molec. Opt. Phys. **32**, 4839 (1999).
[261] G. Raithel and M. Fauth, J. Phys. B **28**, 1687 (1995).
[262] G. Raithel, H. Held, L. Marmet, and H. Walther, J. Phys. B **27**, 2849 (1994).
[263] S. R. Procter, Y. Yamakita, F. Merkt, and T. P. Softley, Chem. Phys. Lett. **374**, 667 (2003).